Statics of Dust Particle on Plasma-Facing Wall and Dynamics in Boundary Plasma

Roman D. Smirnov

DOCTOR OF PHILOSOPHY

Department of Fusion Science
School of Physical Science
The Graduate University for Advanced Studies

2005 (School Year)

Abstract

In present fusion devices the generation of dust particles is observed and characteristics of the dust particles collected after discharges have been analyzed. Typically the collected dust particles have irregular, flake or spherical shapes with sizes from nanometers to tens of micrometers and consist of materials of divertor plates, first wall or inner structures. They are considered to appear in a plasma due to erosion of plasma-facing surfaces, condensation and adhesion of plasma-spattered materials, flaking of redeposition layers. The motion and destruction of dust particles in the high temperature plasma region can contribute to the impurity transport that makes essential to study behavior of dust particles during a discharge. It is well known that dust particles obtain large, usually negative, electrical charge (up to 10^6 elementary charges) in a plasma and can affect electric potential distributions and change kinetic properties of the plasma due to scattering and absorption of plasma particles. The important safety issue is the ability of dust particles to accumulate large amount of radioactive tritium. The dust may be a primary radiological and explosion risk factor. In recent years dust particles also have attracted attention in growing technological applications of plasmas connected to astrophysical, space, laboratory, and processing applications. In fusion devices the dust density usually is not high enough to show the collective effects. Therefore, the aim of the present study is to investigate the behavior of a single dust particle in a plasma wall transition layer that includes sheath formation with the dust particle, analysis of releasing conditions at the wall and possible trajectories of dust particles with various sizes and masses. We consider a conductive spherical dust particle initially placed on the wall. The directions and magnitudes of the forces acting on the dust depend on the local plasma parameters, dust particle size and charge. The present problem needs to be analyzed self-consistently because the charge of the dust particle affects the surrounding plasma and mutually depends on fluxes of electrons and ions to the dust particle. This presents significant difficulties in the theoretical treatment of such problem; therefore, we used computer simulations in combination with a simplified theoretical approach. Assuming local plasma parameters known and fixed we can theoretically find the charge, currents and forces to the dust particle that allows to analyze its behavior in a wide range of sizes, masses, spatial and time scales.

At first, we investigate the conditions allowing a dust particle to be released from the wall, when the total force is acting on the dust towards plasma. The total force in our analysis includes the electrostatic force, the drag forces due to ion absorption and scattering, the electrostatic image force due to redistribution of charges on the wall and the gravitational force. The ion drag force is obtained using the Orbital Motion Limited (OML) theory, which gives us absorption cross section of electrons and ions by the dust particle, and the charge of dust particle attached to the wall is determined by the wall surface charge density and dust radius. The condition for releasing of the dust particle is obtained analytically in respect to the dust radius. From this condition we derive the "first critical dust radius" that is the largest radius of the dust particle capable to leave the wall. Using estimations of plasma parameters near the wall according to the Bohm sheath theory, we can express the first critical radius as a function of the wall potential.

For the case of the zero gravitational force (vertical surfaces), it was shown that the first critical radius exists only when the wall potential exceeds the threshold value, below which no dust particles can be released from the wall. For the deeper wall potentials than the threshold one, the smaller dust particle than the first critical radius will be released and the bigger one will be pinned to the wall due to the large ion drug force compared to the electrostatic force. Changing the wall potential we can control the size of released dust particles or suppress motion of all dust particles. When the gravitational force is directed toward the wall, it reduces the value of the first critical radius, but does not affect the threshold potential. For the opposite direction of the gravitational force, there are two values for the first critical radius, which define two zones in the "dust radius – wall potential" space for the released dust particles. Configuration of the zones is controlled by the gravitational parameter that is a function of dust mass density and plasma parameters. One of the zones is dominated by the electrostatic force and another one by the gravitational force. For a large gravitational parameter they are merged, while for a small one they are separated by a range of wall potentials, where no dust particles can leave the wall.

The motion of the released dust particles in one-dimensional (1D) boundary plasma is analyzed numerically by solving dust motion and charging equations simultaneously. In the model of a plasma being not affected by the dust particle, we consider the 1D system bounded at one side by a perfectly absorbing electrically biased wall and at another side bordering with a bulk plasma with given densities and

temperatures of electrons and ions. The bulk plasma provides continuous inflow of plasma particles into the system, which is filled with uniformly distributed neutral gas. A Debye sheath is formed in front of the wall and an extended ionizing presheath is formed further from the wall due to electron impact ionization of neutral atoms. This system was simulated with the originally developed 1D Particle-in-Cell/Monte-Carlo (PIC/MC) code. The simulations conducted to achieving the steady state give us the spatial distributions of plasma parameters (densities, flow velocities, temperatures, potential etc.) in the sheath and the presheath. Using the OML theory and simulated plasma parameters, we found currents and forces to the dust particle and solved dust dynamics equation numerically. The simulated trajectories of the released particles in a plasma show small or large amplitude oscillations that are sharply discriminated with the critical radius: the "second critical radius". The smaller dust particles than the second critical radius have a large amplitude of oscillations going deeper into the plasma. The existence of the second critical radius is caused by the appearance of an effective potential barrier near the wall due to reduction of the dust charge that depends on sharply changing local plasma parameters. The second critical radius is increasing with decreasing of the dust mass due to a delayed charging effect. This effect leads to the dust charge is being larger than the local equilibrium one during the motion of a released particle from the wall, thus allowing the lighter dust particles to oscillate with a larger amplitude. When the dust mass is smaller than a certain critical value, there is no more clear discrimination between small and large amplitude oscillations and the second critical radius disappears.

The 1D model applied here does not take into account effects of interaction between a dust particle and a plasma. When the size of dust particle is larger than the Debye length, these effects may be significant and disturb the wall sheath formation around the dust particle. For the self-consistent analysis of the spherical dust particle behavior in a boundary plasma near the wall, the two-dimensional (2D) PIC simulations with a cylindrical symmetry are carried out. The charge, electron and ion currents and forces are simulated for a dust particle attached to the wall. It is shown that the simulated dust charge is in a good agreement with the theoretically calculated one for the smaller dust size than the Debye length. The theoretical value is calculated for a polarized dust particle at the wall in non-uniform external electric field, where the interaction between dust and plasma is not included. When the dust size is larger than the Debye length, the absolute value of the dust charge is significantly higher

than the theoretical value. This result is explained by the enhanced normal electric field at the dust surface due to the plasma shielding effect. This effect also leads to increasing of the repulsive electrostatic force and the first critical radius. Simulation result of the electron current density to the dust particle shows weak dependence on the dust size contrary to the OML prediction. A modified OML expression for the electron current density was presented, where the surface potential of the dust is replaced by the fixed wall potential. This modification shows good agreement with the simulation results. The same substitution for the ion current density also eliminates its dependence on the dust particle radius; nevertheless, the discrepancy exists between the simulation results and the modified OML formula. Further modification of the OML expression was made by taking into account the sharp change of the impact parameters (potential energy and flow velocity) of absorbed ions inside the sheath. This correction gives a good agreement between simulation results and theory for the smaller dust particles. For the dust particles bigger than the sheath width, the saturation of the ion current density was observed due to the development of the individual spherical sheath around the dust particle. The 2D simulations confirmed the existence of the first critical dust radius and showed good agreement with the prediction by the 1D model for the smaller dust particles than the Debye length.

In this study the existence of the first critical dust radius was predicted theoretically and confirmed with the 2D self-consistent simulations. We found the second critical dust radius separating small and large amplitude oscillations of the dust particles in the boundary plasma. The 2D self-consistent simulations of a dust particle on the wall gave us a good agreement with the theoretical results for the smaller dust than the Debye length and showed enhancing effect of the dust sheath on the dust particle charge and the electrostatic force. Modifications of the OML expressions for electron and ion current densities are proposed. The self-consistent simulations of the dust particle dynamics in the sheath as well as effects of a magnetic field and various elementary processes remain of the future issues. The results of this research give us the principle understanding of the dust characteristics in boundary plasmas and can contribute to the investigation of the dust dynamics in the realistic and complex situations.

Acknowledgements

First of all, I wish to express deep gratitude to my supervisor Dr. Yukihiro Tomita, who has been educating me with his advises, experience and tolerance through the years of my study in the Graduate University for Advanced Studies (Sokendai), for the guidance, without which this research would be impossible.

I am grateful to Dr. Tomonori Takizuka of Naka Fusion Research Establishment, Japan Atomic Energy Research Institute for valuable discussions on SOL plasma physics and simulation science.

I would like to appreciate Dr. Sergei Krasheninnikov of University California San Diego for the discussions that help me understand the issues of fusion science and for the important comments on this work.

I am thankful to Dr. Noriyasu Ohno of Nagoya University for precious advices concerning dusty plasma physics and experimental results.

I would like to thank Dr. Ratko Janev of Instituut voor Plasmafysica Forschungszentrum Jülich for comments on elementary processes in plasmas and atomic data.

I am appreciating Dr. Akio Sagara of the National Institute for Fusion Science for thorough discussions on dust in the Large Helical Device (LHD).

I want to acknowledge Dr. David Tskhakaya of Association Euratom-ÖAW Institute of Theoretical Physics, University of Innsbruck and Dr. Hisanori Takamaru of Chubu University for useful discussions and advices on computational techniques.

I also would like to appreciate posthumously Dr. Yuriy Chutov of Taras Shevchenko Kiev University for introducing me into the plasma physics.

I am indebted to Director-General Dr. Osamu Motojima, Center Head Dr. Masao Okamoto, and all members of Theory and Computer Simulation Center of the National Institute for Fusion Science for their supply of the wonderful surroundings for my research and everyday life.

I am grateful to the Ministry of Education, Science, Sports and Culture of Japan for the financial support.

Contents

1 Introduction **1**

1.1 Dust particles in fusion and processing plasmas.....1

1.2 Theory and physics of sheath formation.....3

1.3 Properties of dust particles in plasma 6

1.4 Motivation and target setting 10

2 Dust behavior in boundary plasma – One-dimensional model **13**

2.1 Sheath formation.....13

2.1.1 Theoretical analysis 14

2.1.2 Simulation of sheath and presheath 17

2.1.3 Simulation results and comparison with theory.....22

2.2 Behavior of a dust particle 28

2.2.1 Model: charging and forces 28

2.2.2 Release from wall: the first critical radius 34

2.2.3 Dynamics in boundary plasma: the second critical radius.....48

2.3 Dust behavior in edge plasma of fusion devices.....61

2.4 Conclusion 68

3 Dust behavior in boundary plasma – Two-dimensional model **71**

3.1 Introduction.....71

3.2 Numerical method: self-consistent simulations.....74

3.3 Results of self-consistent simulations.....89

3.4 Discussion.....103

4 Summary **105**

Appendix A Local macroscopic quantities in collisionless boundary plasma **111**

Appendix B Sheath potential prop and externally applied voltage **115**

Appendix C Electrostatic potential due to induced charge of spherical dust in non-uniform electric field **119**

Bibliography **127**

Chapter 1

Introduction

1.1 Dust particles in fusion and processing plasmas

In the past years advancing efforts toward controlled fusion as well as growing technological applications of a plasma in semiconductor and chemical industries, extending researches and experiments in space make important understanding of plasma systems behavior of increasing complexity. One of the recent subjects attracted attention in those applications is the presence of small grains of solid matter in the plasma. These grains called the dust particles are typically sized from nanometers to hundreds of micrometers at the earth conditions and can be formed due to various volumetric or surface processes in the plasma [1-4]. Among these processes there are reactions in the chemically active plasmas, condensation and adhesion of spattered materials, etching and spattering of plasma contacting surfaces chemically or/and by ion bombardment, crackling and flaking of redeposited layers etc. These processes lead to the presence of dust particles of different sizes, shapes and compositions in the plasma during discharges and their accumulation after discharges on inner reactor surfaces [4]. The dust particles were experimentally observed in all kind of plasma applications under varying plasma conditions [5-8]. In particular, in the Large Helical Device (LHD) and the ASDEX-Upgrade fusion devices they were collected after series of discharges from inner vessel surfaces at the various toroidal and pololidal locations above and below a midplane [5]. The distribution of dust particles shows no dependence on orientation of the surfaces to the horizontal in the LHD, but the majority of collected dust mass contained in larger particles was from bottom locations in the ASDEX-U. On the other hand, the LHD holds greater dust mass on the surfaces not exposed to the plasma. Most of the collected particles were irregular in shape also some amount of spherically shaped particles was present. The averaged count-median diameter of the particles from the ASDEX-U was about 3μm,

while for the dust from the LHD it was about 10 μm. Almost all particles from both devices contain C, Fe, Cr and Mn, which are divertor plate, first wall and inner structures materials, some particles were mixture of these components. The large amount of dust particles was collected from bottom locations in the TEXTOR tokamak after six month of operation [6]. About 15% of collected particles were ferromagnetic iron reach with some amount of Cr and Ni (Inconel alloy) and noticeable low-Z overlayer. Rest of particles were non-ferromagnetic and composed of graphite or Si, Al, S that came from divertor plate or boronizations and ICR-siliconizations performed during the operation period. Among ferromagnetic particles the large amount of almost perfect spheres was detected with diameters from 10 μm to 100 μm, the flake and irregular shaped particles were also observed. The non-ferromagnetic dust particles were shaped like pieces of rock or graphite clusters with very wide range of sizes from submicrometers to hundreds of micrometers. The variety of shapes and composition of dust particles shows that they were formed by different mechanisms and under different conditions. The spherical particles were likely exposed to the plasma long time or formed in the plasma volume, while the flakes are most likely formed at the surfaces. The divertor region is suggested as one of the most suitable place for the dust particles formation due to the high energy flux to divertor plates and the relatively cold plasma, where dust particles may dwell long time and even grow. Also the dust particles can appear at the time of He glow discharge cleaning or film deposition discharges (boronization, siliconization).

During discharges in a fusion device the dust particles can move in the plasma that was observed by a laser scattering method in the JIPPT-IIU tokamak [7] and by an infrared camera in the Extrap-T2 and the TEXTOR devices [9]. It is suggested that the dust particles can be accelerated to significant velocities in boundary plasma regions and moving toward the core plasma can contribute to the contamination level of the plasma [10,11]. However, at present the influence of the dust particles on operational conditions of fusion devices is not well understood [4] and the amount of accumulated experimental data on dust dynamics in fusion devices is not sufficient for clear conclusions. Among other issues the important one is the safety operation of future fusion devices like the International Thermonuclear Experimental Reactor (ITER) [12]. The carbon dust particles can absorb large amount of tritium (>0.2 H/C) and are highly reactive. This imposes radiological and explosion risk in case of

vacuum or coolant leakage as well as during maintenance periods. That may require the periodic cleaning and utilization of dust from fusion devices that can accumulate at the inner surfaces during operation periods. In the ITER the expected energy flux to the plasma-facing components during a disruption may reach dangerous values of a few $10\,\mathrm{GW/m^2}$ and destruction rate of energy absorbing surfaces may be significant producing large amount of dust. That makes actual study of dust particles behavior in edge plasmas of fusion devices during discharges.

The processing plasma used for semiconductor industry is usually a low temperature weakly ionized plasma of noble gases or mixture with chemically active gases like silane (SiH_4). Under such conditions the dust particles readily grow due to chemical reactions of various radicals in the plasma volume and coagulation of smaller clusters and particulates as well as substrate etching [8]. The amount of dust particles under such conditions can be as high as $10^{3-4}\,\mathrm{cm^{-3}}$ that is enough to make important collective effects of dust-plasma and dust-dust interactions, when such plasma is called a dusty plasma [13-15]. In dusty plasmas various new phenomena are observed like dusty crystal formation [16,17], dust voids and vortices as well as new types of waves and instabilities. The important one for material processing is possible effect of dust particles on potential profiles and ion fluxes in the plasma near a wall [18,19] and as well as substrate damage due to dust impact. However, in fusion devices the dust density most likely doesn't reach such high levels and study of a single particle dynamics is more important, toward which the present work is oriented. Nevertheless, for the processing plasma the properties of a single dust particle are fundamental and can be used for analysis of various dust phenomena.

1.2 Theory and physics of sheath formation

As the boundary plasma is one of the probable formation locations of dust particles and the region where a dust particle moves starting from the wall or toward the wall carrying charge and kinetic energy, the description of a plasma wall transition (PWT) layer is required for understanding of dust dynamics. The wall in contact with a plasma under negative floating or bias potential repulses electrons and attracts ions. That creates positively charged region near the wall which screens the plasma from the wall potential and is called a sheath. This screening is not perfect, however, and

the electric field extends into the plasma forming a non-uniform PWT layer. The formation of a PWT layer near a wall is one of the earliest plasma problems pointed out first by Tonks and Langmuir as far back as 1929 [20]. They described the potential structure in the PWT layer using series expansion method for a Poisson's equation solving with various models of ion collisionality in fluid approach. Also they phenomenologically defined the sheath edge as a point, where the local charge density is a small fraction (they used 0.05) of the local electron charge density. The practically quasi-neutral plasma outside the sheath is called a presheath and the quasi-neutral "plasma solution" of potential distribution can be applied there. The concept of the sheath edge has played the significant role in the development of the PWT layer theory although its definition was changed and the intermediate transition layer between the sheath and the presheath was introduced by Riemann much later [21,22]. As the fluid plasma solutions for a presheath are valid in the limit of the vanishing Debye length $\lambda_D \to 0$, they have singularity at some point near a wall, where the electric field goes to infinity. This point was defined as the sheath edge in the fluid approach [23]. The important step in the theory development was the Bohm criterion [24] for the sheath formation stating that ion flow velocity at the sheath edge should be no less than the ion sound speed. The Bohm criterion in fluid approach is valid regardless of ion collisionality or ionization model, because it defines the singularity point intrinsically inherent to plasma solutions of a presheath [25]. The potential distribution in the sheath can be found only by solving the Poisson's equation, which is possible analytically in the limit of the sheath edge positioned infinitely far from the wall on the Debye length scale. Then the Bohm criterion is applied to this infinitely far point as necessary condition for positive spatial charge development in the sheath. Therefore, physically the Bohm criterion and the sheath formation require that the electron density in the sheath decays faster than the ion density toward the wall. Other qualitative interpretation implies that no disturbances of the plasma by the wall can propagate into the plasma volume with the lower speed than the ion sound speed, thus the positively charged sheath region is localized near the wall. As we noted, the Bohm criterion is satisfied at the sheath edge independently on ion collisionality, so ions should be pre-accelerated in the presheath region up to the ion sound speed. Nevertheless, the presheath can be non-uniform with ion accelerating potential drop only if there is some process leading to momentum loss of ions or growing of the ion

flux [21]. Thus, the collisional, ionizing and geometrical presheaths are possible and the characteristic length of the plasma parameters and electric potential variations in the presheath will be order of the corresponding collision mean free path or geometrical scale. Another type of presheaths was pointed by Chodura [26] is the magnetic presheath, where the magnetic field lines are oblique to the wall. He introduced the magnetic presheath edge condition stating the parallel to the magnetic field ion velocity should be larger than the ion sound speed. The characteristic length of the magnetic presheath is the ion Larmor radius. Later it was shown that the magnetic presheath mechanism is associated with the ion polarization drift [27]. In real complex situations different presheath mechanisms can play important role, thus the mixed presheath can be formed.

The kinetic theory of the boundary plasma is also developed [28]. The difference of the kinetic approach from the fluid one is the description of plasma particles densities, flow velocities and other parameters as the moments of the particles velocity distribution functions, which are solutions of the Boltzmann equation. Nevertheless, in the kinetic approach it is also necessary to solve the Poisson's equation to obtain the potential distribution in the sheath or use the "plasma solution" for the presheath. Therefore, the kinetic PWT layer theory inherited the same scale problem and the singularity of the plasma quasi-neutral solutions in the limit $\lambda_D \to 0$ as the fluid one. The sheath edge concept is also used in kinetic approach as the singularity exists in the zero λ_D limit. The kinetic form of the Bohm criterion was obtained, which imposes restrictions on the ion velocity distribution function [29]. The kinetic form of the Bohm criterion shows that the ion velocity distribution function at the sheath edge should vanish for zero ion velocities and can be reduced to the fluid form using a perturbation method.

However, in the case of the finite Debye length the presheath quasi-neutral solution can be substituted with the Poisson's equation solution with the smallness parameter of the Debye length scale. In this case, the presheath solution has no singularity and the sheath edge concept loses its meaning. Moreover, in this case it was shown that the kinetic form of the Bohm criterion is satisfied everywhere in the plasma and has no information on the sheath formation [21]. Nevertheless, for finite small values of the ratio of the Debye length to the presheath characteristic length, the theory of the sheath and the presheath has essentially different spatial scales and can

not be matched in the analytical integrated PWT layer solution. The exception is the case of a highly collisional plasma, when the presheath characteristic length is comparable with the Debye length and smooth transition can be obtained [22,30]. For general case Riemann introduced the intermediate spatial scale that has characteristic length in between the Debye length and the presheath length scales [21,22]. This intermediate scale serves for smooth matching of the sheath and presheath solutions instead of the sheath edge concept. Therefore, at present there is three-scale theory for description of the PWT layer including the positively charged Debye sheath, the quasi-neutral presheath and the transition layer between them. The solutions at each region are scalable in the real coordinates. Nevertheless, the sheath edge concept had great impact on boundary plasma physics, especially in fluid approach, that discussions about it continues, see for example [31-35]. Of cause, the Poisson's equation can be solved numerically in the whole plasma that, however, needs appropriate boundary conditions at some point of the presheath or a plasma source between two walls. Usually the boundary conditions in the presheath are set approximately, iteratively excluding unphysical presheath solutions. In addition to the mentioned presheath mechanisms, the effect of various elementary processes and plasma conditions on the sheath formation is studied in numerous theoretical and simulation works. Among these effects there are secondary electron emission from the wall, two or more kinds of positively or negatively charged plasma particles, different velocity distributions of ions and electrons, different configurations of a magnetic field and combinations of these effects that are important to study for realistic conditions found in fusion or processing plasmas. Some calculations of the dusty PWT layers are also done showing multilayer structures of the dusty sheaths [36-38].

1.3 Properties of dust particles in plasma

It is well known from experimental and theoretical researches [39,40,13] that dust particles in a plasma obtain large electric charge (up to 10^6 elementary charges) due to electron and ion currents on them which are defined by plasma conditions. The charge of the dust particle is its critical parameter, which is most important to describe dust effect on the plasma as well as find acting forces on the dust particle and describe its dynamics. Usually electrons in the plasma have higher velocities than ions and

their flux to the dust particle exceeds the ion flux, so the dust particles get negative charge in the plasma, unless the electron density is too low or the secondary electron emission from the dust particle is strong. From this point of view the dust particles can be considered as small floating probes in the plasma. However, the sizes of dust particles usually are very small and classical Langmuir probe theory is not applicable for them until dust size will not be much larger than the Debye length and the ion collision mean free path, when the current to the dust can be described in the planar sheath limited regime. Instead, for description of charging of small dust particles the Orbital Motion Limited theory is commonly used [41,42], which defines the currents to the dust particle using the plasma particles absorption cross section by the spherical dust obtained in the orbital motion approximation. This approximation assumes collisionless motion of electrons and ions around a dust particle described by angular momentum and energy conservation laws. Therefore, the OML theory does not consider specifics of potential distribution around the dust particle in the plasma. It considers the impact parameter, which belongs to the electron or ion trajectory tangentially grazing the dust surface, as the radius of the absorption cross section area as long as it is assumed that all particles with the smaller impact parameters will cross the dust surface. This assumption, however, is not satisfied for every potential distribution around the dust particle [42,43]. There are two limitations, the first: when the potential decreases toward the dust faster than approximately $1/r^2$ then falling to the center ion trajectories are possible and the absorption cross section will be defined by some critical absorption radius instead of the grazing surface trajectory [42]. The second, the effective potential barrier can appear for certain values of the ion angular momentum, so such ion will not reach the dust surface even though their impact parameter is smaller than the one corresponding to the grazing trajectory [44,45]. On the other hand, it was shown that relative quantity of such rejected ions is small and does not affect ion current to the dust significantly until the plasma density is not high and the ion temperature low [45]. The potential distribution around the dust particle is defined by the screening of the dust charge with the plasma and is the issue of the sheath formation around the dust particle. However, the dust screening is the complex self-consistent problem requiring kinetic description and the complete kinetic dust charging theory is not developed yet. There are studies applicable to describe dust charging under simplified conditions. The theory of Bohm, Burhop and Massey [46]

uses the quasi-neutral plasma solution to find the potential profile around the spherical probe in the plasma. Thus, it is valid only for the dust particles, which radii are much larger than the Debye length and much smaller than the ion collision mean free path. Another, the radial motion ABR (Allen, Boyd, Reynolds) theory [47,48] solves the Poisson's equation for the purely radial ion motion toward the dust particle, and thus is valid in the cold ions approximation. The numerical study of the sheath structure around dust particles was performed in [49] showing that the potential distribution in the sheath can be well described by the Debye-Hückel potential and the screening dust radius is changing from the linearized ion-electron Debye length for small dust particles to the electron Debye length for larger particles. All the mentioned theories describe dust charging in the infinite plasma with spherically symmetrical potential distribution around the particle. However, the dust particle motion usually occurs in complex conditions of plasma flows and external fields, in particular, in the plasma wall transition layers. The study of a dust particle in more complex conditions of an ion flow showed anisotropic potential distribution around a dust particle, which is called a wake potential [50]. In this case the region of increased ion density is formed behind the particle in the flow. The simulation studies of the dust charging and screening in the ion flow demonstrate the potential distribution around the dust particle clearly [51,52]. Nevertheless, there is no self-consistent theory to describe the effect analytically. The complex picture of the dust particle screening in the flow affects not only the dust charging, but also the ion drag force acting on the particle in the ion flow. The ion drag force is directly associated with momentum transfer from the ions to the dust particle. The momentum transfer occurs due to direct absorption of ions and due to scattering of ions by the dust. The latter one is also responsible for the wake field formation. Usually the OML theory is used to describe the absorption part of the ion drag force. The simulation studies of the ion drag force due to scattering [53,54] show that the classical scattering theory with the cutoff Coulomb potential assumption underestimates the force for low ion energies. The role of the electron drag force is also recognized for specific plasma parameters in the presence of a constant external electric field [55]. Most of the mentioned studies are relevant to the dust particles with smaller radii than the Debye length. The comprehensive simulation study of the dust charging and shielding in the ion flow for larger dust particles than the Debye length is recently performed by Hutchinson [56-58]. It shows that for subsonic ion flows the downstream side of the dust particle can receive higher ion

flux than the upstream one, however, reporting that the ion drag force acting on the dust particle is with 20% accuracy agrees with the present analytical approximations. Nevertheless, all the studies mentioned here do not take into account the presence of the wall and the non-uniform electric field in the sheath.

It is known from experimental and theoretical works that dust particles can levitate in the sheath under the balance of electrical, ion drag and gravitational forces acting on them [59,62]. The experiments are usually conducted in the plasma of DC or RF glow discharges with low degree of ionization and artificially prepared dust particles, which are observed by a CCD (charge-coupled device) camera in a scattered light of laser. However, the dynamical measurements of dust charges, currents and forces on them are indirect and unreliable. The trapping of the dust particles in the sheath region near a horizontally placed electrode was observed, where the particles can oscillate around their equilibrium positions and even form the periodic structures known as dusty crystals when their motion in the horizontal plane is restricted and electrostatic coupling is strong [17,61]. The dust particles in the dusty crystals are aligned not only in the horizontal but also in the vertical direction, what as suggested is due to wake potential formation downstream of the upper layers of dust particles. Because of usually high neutral gas density in the laboratory plasma experiments with dust particles, their oscillations around equilibrium positions in the sheath are damped due to neutral atoms and ions friction. The measurements of the frequency, damping rate and equilibrium positions of dust oscillations are proposed as a plasma sheath diagnostics [62]. On the other hand, due to finite charging time of the dust particles their charge has lag during the dust motion that is called a delayed charging effect. It is shown that the delayed charging effect can lead to parametric instability and self-exiting vertical dust oscillations in the sheath [63,64]. The simulation studies of dust levitation and dynamics in sheaths are conducted within the fluid description of a plasma in a sheath [60,65]. They show that there is the maximum radius of dust particles that are capable to levitate, above which the particles fall down to the electrode. In [65] the forces acting on the dust particle in the sheath are described in the fluid approach and the conditions for capturing of the particles injected into the sheath from a wall with different velocities are analyzed. It showed that there is a narrow range of dust velocities and radii when the trapping of dust particles is possible, otherwise the dust particle fall down on the wall. However, these works do not consider what happens with the dust particle on the wall surface, while the

charging of the dust particle on the wall is significantly different from its charging in a plasma [66]. Also the used model of dust charging and motion in sheaths is not self-consistent and valid only for small dust particles. A few direct observations of dust particles motion in fusion devices was performed [9], which show projections of dust trajectories on the plane transverse to the view line, but provides no information on dust sizes and charges.

1.4 Motivation and target setting

As the dust particles are commonly found in present plasma application devices including fusion devices, investigations of their impact on the operation conditions of those devices are necessary. The sources of dust particles in plasma reactors can include destruction and deposition processes on plasma-facing surfaces as well as the volumetric chemical and physical processes. The dust particles can affect electric potential profiles in a plasma due to the large absorbed charge and also can change kinetic plasma properties due to plasma particles absorption and scattering. The moving dust particles in processing plasma applications can strike a processed material causing its damage or can accumulate in some areas of plasma reactors changing operation characteristics. In fusion devices moving dust particles are probable sources of impurities, which transport is radically different from ion impurities transport due to a variable charge, a huge mass and a large size. The highly charged dust particles also can contribute in radiation energy loss in a divertor region of fusion devices. Another important issue for future fusion reactors is ability of the dust particles to absorb significant amount of tritium that makes them potentially dangerous. The regions near walls of plasma reactors are the places where the dust particles are usually produced and accumulate during operation period. As known the highly non-linear plasma wall transition layer is formed near the plasma-facing wall, where electric fields and plasma particles flows are significant. Hence, studies of dust dynamics in plasmas and, in particular, near wall regions of plasma reactors are important for understanding of a dust impact on their operation. Investigation of a single dust particle motion is a key element for study of more complex dust systems dynamics and is directly applicable for low dust density conditions like in fusion devices. The previous studies were restricted by either consideration of dust particles

smaller than the Debye length and not attached to the wall or the simple ion flow conditions not accounting the wall presence as another sheath boundary.

Therefore, the aim of the present study is the investigation of a single dust particle statics and dynamics in PWT layers, which includes the self-consistent sheath formation with the dust particle, analysis of starting conditions at the wall and possible trajectories of dust particles, which size can be larger than the Debye length. The thesis consists of the four chapters. In Chapter 1 (Introduction) the main results of previous researches on sheath formation, basic properties of dust particles and their behavior in sheaths are described, on basis of which the motivation of the present study and its target is given. In Chapter 2, the dust particle behavior in PWT layer is analyzed using one-dimensional (1D) approach. That includes description of the 1D PIC (Particle-In-Cell) simulation method of PWT layer without dust particle and comparison of the simulation results with the kinetic theoretical consideration, the model of currents and forces acting on the dust particle in the undisturbed plasma. In this chapter the first critical radius is derived theoretically [67] and the second critical radius is shown from the analysis of dust trajectories, which defines dust releasing condition from the wall and discriminates different types of dust particles trajectories, respectively [68]. There is also discussion of dust particles surviving conditions and dynamics in the edge plasma of fusion devices. In Chapter 3 the self-consistent two-dimensional (2D) simulations of a large dust particle properties in the sheath on the wall position is presented. The chapter is opened with the introduction which explains drawbacks of the one-dimensional model and possibilities of the two-dimensional one for self-consistent analysis. After that the description of the originally developed 2D simulation model is given. The simulation results confirm the existence of the first critical radius. They are compared with predictions of the 1D model and its possible modifications are discussed together with peculiarities of the sheath formation with a dust particle, which radius is bigger than the Debye length. The final Chapter 4 includes summary of the results and discussion on unresolved problems and future issues. In the Appendices necessary mathematical derivations are presented.

Chapter 2

Dust behavior in boundary plasma – One-dimensional model

In this chapter we consider one-dimensional (1D) model of a dust particle behavior in a plasma wall transition (PWT) layer that includes kinetic analysis of collisionless sheath formation, description of the 1D PIC simulation method of the PWT layer without a dust particle, comparison of the simulation results with the kinetic theoretical consideration, and the model of currents and forces on the dust particle in undisturbed plasma. The one-dimensional model assumes that the dust particle doesn't disturb distributions of plasma parameters in sheath significantly, which is possible if the dust particle is small compared to the Debye length, presumably. Here the first critical radius is derived theoretically [67] and the second critical radius is shown from the analysis of dust trajectories [68]. Dust dynamics in an edge plasma of fusion devices is discussed.

2.1 Sheath formation

In order to analyze behavior of a dust particle in a boundary plasma we should know the properties of a sheath and a presheath including spatial distributions of potentials, densities, fluxes etc. These parameters are used later to obtain local values of a dust charge and acting forces on it that allow simulating the dust particle's motion. The theoretical fluid description of a PWT layer is not convenient for dust motion analysis as it separately considers a sheath and a presheath at different length scales and an intermediate layer is required for the smooth transition between them. Therefore, we use the computer simulation of the integrated sheath-presheath system and kinetic theoretical analysis of the sheath to check the accuracy of the simulation code.

2.1.1 Theoretical analysis

The formation of a collisionless sheath for given initial distribution functions of electrons and ions can be analyzed theoretically in the kinetic approach that gives exact solutions for distributions of plasma parameters. This consideration includes effect of truncation of electron velocity distribution function, when high-energy electrons are capable to reach the wall over the sheath potential drop and are absorbed there, as a result a deficit of high-energy reflected electrons is produced. Therefore, the electron velocity distribution function in the sheath will not be a full Maxwellian distribution as it is assumed in all fluid analysis of the sheath formation. This exact consideration of the collisionless sheath formation allows us to test correctness of the developed one-dimensional simulation code for sheaths.

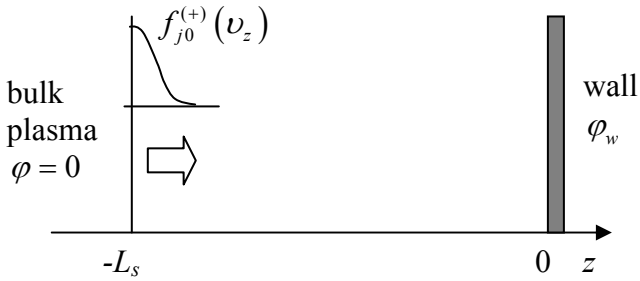

Fig. 2.1.1 *One-dimensional model for the kinetic analysis of the collisionless sheath formation.*

Let's consider the one-dimensional system (Fig.2.1.1) that is bounded by a perfectly absorbed wall at the right end $z = 0$ with the negative potential $\varphi_w < 0$ and the bulk plasma at the left $z = -L_s$ with the fixed potential $\varphi = 0$. There are no collisions and volumetric sources or sinks of plasma particles in the system. The bulk plasma consists of electrons and ions of charge q_i and provides half-Maxwellian particle inflows into the system. The half-Maxwellian velocity distribution functions of electrons and ions $f_{e0}^{(+)}$, $f_{i0}^{(+)}$ have given densities $n_{e0}^{(+)}$, $n_{i0}^{(+)}$ and temperatures T_e, T_i, respectively, the superscript (+) here denotes particles with positive velocities to the z direction.

For the injected particles of species $j = e, i$ the half-Maxwellian velocity distribution function is written as

$$f_{j0}^{(+)}\left(\upsilon_z\right)=2n_{j0}^{(+)}\sqrt{\frac{m_j}{2\pi T_j}}\exp\left(-\frac{m_j\upsilon_z^2}{2T_j}\right), \tag{2.1.1}$$

where m_j is the mass of j-th species particle. The plasma particle distribution functions inside the system should satisfy the collisionless Boltzmann equation

$$\upsilon_z\frac{\partial f_j\left(z,\upsilon_z\right)}{\partial z}-\frac{q_j}{m_j}\frac{d\varphi(z)}{dz}\frac{\partial f_j\left(z,\upsilon_z\right)}{\partial \upsilon_z}=0\,, \tag{2.1.2}$$

where $\varphi(z)$ is the local electrostatic potential. For the case of a monotonic spatial profile of the potential, which we can expect in the collisionless sheath, equation (2.1.2) has the exact solution in the whole system. Changing the velocity variable in the Boltzmann equation to the total energy

$$\varepsilon_{jz}\equiv\frac{1}{2}m_j\upsilon_z^2+q_j\varphi(z)\,, \tag{2.1.3}$$

we can get

$$\upsilon_z\left(z,\varepsilon_{jz}\right)\frac{\partial f_j\left(z,\varepsilon_{jz}\right)}{\partial z}=0\,. \tag{2.1.4}$$

Therefore, the solution of eq. (2.1.4) for the particles with positive velocities is

$$f_j^{(+)}\left(z,\varepsilon_{jz}\right)=f_{j0}^{(+)}\left(\varepsilon_{jz}\right)=2n_{j0}^{(+)}\sqrt{\frac{m_j}{2\pi T_j}}\exp\left(-\frac{\varepsilon_{jz}-q_j\varphi(z)}{T_j}\right), \tag{2.1.5}$$

that means the shape of total energy distribution function of injected particles does not change spatially and their total energy conserves. In the Debye sheath formed near the negatively biased wall, the monotonically decreasing potential accelerates ions toward the wall, thus the local velocity of the slowest ion is $\upsilon_{is}\left(z\right)=\sqrt{-2q_i\varphi(z)/m_i}$ and all ions come to the wall. For electrons the sheath potential is repulsive, thus only the part of electrons with initial velocities larger than $\upsilon_{es}=\sqrt{-2e\varphi_w/m_e}$ will be absorbed by the wall, while the rest of electrons is reflected by the negative sheath potential and forms the negative velocity part of the electron distribution function $f_e^{(-)}\left(z,\varepsilon_{ez}\right)$. This function satisfies the same Boltzmann equation (2.1.4) and has the similar solution

$$f_e^{(-)}\left(z,\varepsilon_{ez}\right)=f_e^{(-)}\left(-L_s,\varepsilon_{ez}\right)=f_{e0}^{(+)}\left(\varepsilon_{ez}\right),\quad \varepsilon_{ez}<-e\varphi_w\,, \tag{2.1.6}$$

$$f_e^{(-)}\left(z,\varepsilon_{ez}\right)=0,\quad \varepsilon_{ez}\geq-e\varphi_w\,. \tag{2.1.7}$$

As we can see, the high energy part of electrons with the negative velocities is truncated and the local truncation velocity is $\upsilon_{etr} = -\sqrt{2e\left[\varphi(z)-\varphi_w\right]/m_e}$.

Now, when we know the local distribution functions, we can find the local macroscopic plasma parameters (Appendix A). The densities of electrons and ions are

$$n_e(z) = n_{e0}^{(+)} \exp\left(\frac{e\varphi(z)}{T_e}\right)\left[1+\operatorname{erf}\left(\sqrt{\frac{e\left[\varphi(z)-\varphi_w\right]}{T_e}}\right)\right], \tag{2.1.8}$$

$$n_i(z) = n_{i0}^{(+)} \exp\left(-\frac{q_i\varphi(z)}{T_i}\right)\operatorname{erfc}\left(\sqrt{-\frac{q_i\varphi(z)}{T_i}}\right), \tag{2.1.9}$$

where $\operatorname{erf} x \equiv \frac{2}{\sqrt{\pi}}\int_0^x e^{-t^2}\,dt$ and $\operatorname{erfc} x \equiv 1-\operatorname{erf} x$ are the error function and the complementary error function, respectively. The effect of the truncation of the electron velocity distribution function is displayed by the term with the error function of potential in (2.1.8), which provide reduction of the electron density in comparison with the usual Boltzmann relation. The corresponding fluxes have the following form

$$\Gamma_e = n_{e0}^{(+)}\sqrt{\frac{2T_e}{\pi m_e}}\exp\left(\frac{e\varphi_w}{T_e}\right), \tag{2.1.10}$$

$$\Gamma_i = n_{i0}^{(+)}\sqrt{\frac{2T_i}{\pi m_i}}, \tag{2.1.11}$$

and the flow velocities are

$$u_{ez}(z) = \sqrt{\frac{2T_e}{\pi m_e}}\,\frac{\exp[-e\left(\varphi(z)-\varphi_w\right)/T_e]}{1+\operatorname{erf}[\sqrt{e\left(\varphi(z)-\varphi_w\right)/T_e}\,]}, \tag{2.1.12}$$

$$u_{iz}(z) = \frac{\sqrt{2T_i/\pi m_i}}{\exp(-q_i\varphi(z)/T_i)\operatorname{erfc}(\sqrt{-q_i\varphi(z)/T_i}\,)}. \tag{2.1.13}$$

The fluxes are constants in the sheath because there are no any particle sources or sinks, also we should note that the electron flux is created exclusively due to the truncation of the electron velocity distribution function, otherwise the symmetrical Maxwellian distribution does not provide any flux. From the floating wall condition $\Gamma_e = \Gamma_i$ it is easy to find the floating wall potential

$$\varphi_{w,fl} = -\frac{T_e}{e}\frac{1}{2}\ln\left[\left(\frac{n_{e0}^{(+)}}{n_{i0}^{(+)}}\right)^2 \frac{m_i}{m_e}\frac{T_e}{T_i}\right]. \tag{2.1.14}$$

The Poisson's equation $\varepsilon_0 \frac{d^2\varphi}{d\,z^2} = q_i n_i\left(z\right) - en_e\left(z\right)$ should be solved in order to obtain the spatial distribution of the potential in the system. Unfortunately, it is strongly nonlinear second order differential equation that can not be solved analytically. Nevertheless, the obtained expressions for plasma parameters as functions of the local potential are suitable for the comparison with the simulations.

2.1.2 Simulation of sheath and presheath

The Particle-In-Cell/Monte-Carlo (PIC/MC) simulations are used here to get plasma parameters distributions in the whole PWT layer including a sheath and a presheath. As well known, a presheath can be formed if some elementary process leading to changing of ion momentum or flux is present in the system [21]. Such processes can be elastic collisions of ions with neutrals, ionization, charge exchange or presence of an oblique magnetic field. The kinetic simulation of the PWT layer with collisional processes can be readily performed with PIC/MC simulations [69,70] that require only collisional cross sections and make no assumptions on the form of a collisional integral in the Boltzmann equation despite simplified or fluid approaches. The PIC method based on solving of motion equations of super-particles, which are ensembles of real particles of one kind with close positions and velocities or in other words small elements of a phase space developing in time as one super-particle. The motion is performed discretely in time on a spatial mesh, which serves for solving of field equations. The Monte-Carlo extension to the PIC method [70,71] calculates the probability of a collisional process for super-particles and performs the collision of a super-particle when a random number hits in the normalized probability. The probability can be calculated for each particle and local plasma parameters. Therefore, the PIC/MC

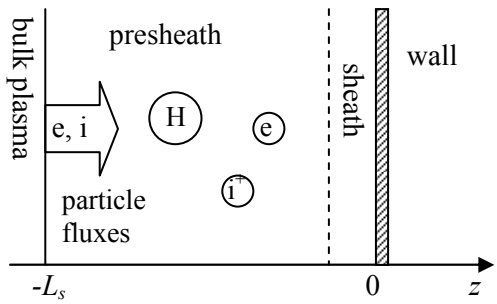

Fig. 2.1.2 *One-dimensional model of the simulated system.*

method allows to kinetically simulate a plasma with elementary processes in self-consistent way. For our simulations we developed original one-dimensional in space and three-dimensional in velocity space (1D3v) code based on the PIC/MC method. The model and the simulation method are described below.

The plasma in the simulated system (Fig.2.1.2) consists of ions, electrons, and hydrogen atoms uniformly distributed with a fixed density n_a and a temperature T_a. The simulated system of the length L_s is bounded by the bulk plasma containing equilibrium electrons and ions with the constant densities $n_{e0} = n_{i0} = n_0$ and the temperatures T_e, T_i. The bulk plasma provides incoming electron flux with half-Maxwellian and ion flux with shifted Maxwellian velocity distribution functions, where the velocity shift is a given parameter, which sets the incoming ion flux. The boundary of the bulk plasma at the same time is transparent for outgoing particles that form the negative velocity part of the distribution functions. The elementary processes accounted in the system are ionization of neutrals by electron impact collisions, elastic scattering of ions on the neutral atoms and charge exchange. Depending on selected plasma parameters we can turn on and off different processes that allows us to create the ionizing or collisional presheath. For the conditions of a divertor plasma the ionizing presheath may be preferable due to a relatively high plasma temperature. The wall is assumed perfectly absorbing for electrons and ions and no secondary emission and recycling are considered. Hence, the sources of electrons and ions in the system are the bulk plasma and the plasma generated by electron impact ionization, and the sink is due to coming out of plasma particles through the boundaries of the system. We do not consider the magnetic presheath formation here; however, the magnetic field which is perpendicular to the wall can be present in the system.

For electron impact ionization cross section the Lotz's formula [72] was used for ionization of a ground state atom to a single ionized ion

$$\sigma_{iz} = \sum_{k=1}^{K_s} a_i \varsigma_i \frac{\ln\left(\varepsilon_e / \chi_i\right)}{\varepsilon_e \chi_i} \left\{ 1 - b_i \exp\left[-c_i \left(\frac{\varepsilon_e}{\chi_i} - 1 \right) \right] \right\}, \tag{2.1.15}$$

where ε_e [eV] is the energy of the impact electron, χ_i is the binding energy of electrons in the *i*-th subshell, ς_i is the number of equivalent electrons in this subshell; a_i, b_i, and c_i are the fitting constants. These parameters for two gases (hydrogen and argon) are presented in Table 2.1.1.

	H	Ar
K_s	1	2
ς_1	1	6
χ_1, eV	13.6	15.8
a_1, $10^{-14}\,\mathrm{cm}^2\mathrm{eV}^2$	4.0	4.0
b_1	0.60	0.62
c_1	0.56	0.40
ς_2	-	2
χ_2, eV	-	29.2
a_2, $10^{-14}\,\mathrm{cm}^2\mathrm{eV}^2$	-	4.0
b_2	-	0.4
c_2	-	0.6

Table 2.1.1 *Electron impact ionization cross section parameters of hydrogen and argon atoms* [72].

After the ionizing collision the impact electron has energy

$$\varepsilon_{cs,e} = \varepsilon_e - \chi_1 - \varepsilon_{new,e}, \tag{2.1.16}$$

where $\varepsilon_{new,e}$ is the energy of the created electron, which was taken from [71, eq.(77)] the same for H and Ar

$$\varepsilon_{new.e} = 10\tan\left[R\arctan\left(\frac{\varepsilon_e - \chi_1}{20}\right)\right], \tag{2.1.17}$$

here all energies are in eV, and R is the uniform random number on the range (0,1]. Both the impact electron after ionization and the created electron have isotropic distribution of velocity vector in velocity space. Created ions have random velocities according to the isotropic Maxwellian velocity distribution function with the neutral gas temperature T_a

$$f_{new,i} = \left(\frac{m_i}{2\pi T_a}\right)^{\frac{3}{2}} \exp\left(-\frac{m_i\left[\upsilon_x^2 + \upsilon_y^2 + \upsilon_z^2\right]}{2T_a}\right). \tag{2.1.18}$$

The cross section for elastic collisions of ions with neutrals for hydrogen was taken from [73,74]

$$\sigma_{el} = \sigma_0 \left(A_0 + A_1 \ln \varepsilon_{CM} + A_2 \ln^2 \varepsilon_{CM} \right), \tag{2.1.19}$$

where $\sigma_0 = 2.80028 \times 10^{-21}\ \mathrm{m}^2$, ε_{CM} is the collision energy in the center-of-mass (CM) system expressed in eV, and the coefficients A_i for hydrogen are $A_0 = 0.591039 \times 10^3$, $A_1 = -0.877354 \times 10^2$, $A_2 = 0.256830 \times 10^1$. For argon atoms corresponding cross sections were taken from the experimental data [75] and were fitted with the same formula (2.1.19) with the coefficients $A_0 = 0.14264 \times 10^3$, $A_1 = -0.2335355 \times 10^2$, $A_2 = 0.176657 \times 10^1$. For simulation of the ion elastic collisional process with neutral atoms, the random velocity of an atom $\vec{\upsilon}_a$ is obtained according to the isotropic Maxwellian (2.1.18). After that the relative velocity $\vec{\upsilon}_{rel} = \vec{\upsilon}_{i0} - \vec{\upsilon}_a$ and the center-of-mass velocity $\vec{\upsilon}_{CM} = \left(\vec{\upsilon}_{i0} + \vec{\upsilon}_a\right)/2$ are calculated, here $\vec{\upsilon}_{i0}$ is the velocity of an ion before the collision. The collision energy in the CM system then is

$$\varepsilon_{CM} = \frac{m_i}{4} \left|\vec{\upsilon}_{rel}\right|^2. \tag{2.1.20}$$

After scattering the new relative velocity $\vec{\upsilon}_{rel,sc}$ is calculated, so that $\left|\vec{\upsilon}_{rel,cs}\right| = \left|\vec{\upsilon}_{rel}\right|$ and its direction is random isotropically distributed in velocity space. The velocity of the ion after scattering is found as

$$\vec{\upsilon}_{i,sc} = \vec{\upsilon}_{CM} + \frac{1}{2} \vec{\upsilon}_{rel,sc}. \tag{2.1.21}$$

The charge exchange cross section is given according to [73,74] both for hydrogen and argon as

$$\sigma_{cx} = \frac{A_0 \ln\left(A_1 / \tilde{\varepsilon}_{CM} + A_2\right)}{1 + A_3 \tilde{\varepsilon}_{CM} + A_4 \tilde{\varepsilon}_{CM}^{3.5} + A_5 \tilde{\varepsilon}_{CM}^{5.4}}, \tag{2.1.22}$$

where $\tilde{\varepsilon}_{CM} = 10^{-3} \varepsilon_{CM} / A_w$, ε_{CM} [eV] is the same as for elastic collisions, A_w is the atomic weight (for hydrogen $A_w = 1$ and for argon $A_w = 40$). The coefficients are $A_0 = 3.2345 \times 10^{-20}\ \mathrm{m}^2$, $A_1 = 0.23588 \times 10^3$, $A_2 = 0.23713 \times 10^1$, $A_3 = 0.38371 \times 10^{-1}$, $A_4 = 0.38068 \times 10^{-5}$, and $A_5 = 0.11832 \times 10^{-9}$. The ion velocity after the collision is substituted with a random velocity isotropically distributed in the velocity space according to the Maxwellian (2.1.18) with the neutral gas temperature T_a.

The PIC method includes calculation of electrons and ions trajectories represented by super-particles in the self-consistent electric potential. The spatial

distributions of the potential at each time step are obtained by solving the Poisson's equation with zero potential of the bulk plasma boundary, $\varphi(-L_s)=0$, and the given potential of the wall φ_w. Another modification of the 1D code has the floating wall boundary condition with the electric field at the wall given according to the wall surface charge density $E_w=-\sigma_w/\varepsilon_0$. The surface charge density σ_w of the wall found by accumulating of collected charges from the plasma and assumption of neutrality for the whole plasma including the bulk. After the discretization of the Poisson's equation on the uniform spatial mesh using finite difference formulae the obtained three-diagonal matrix is solved by the sweep method [70].

Simulations of the plasma in the system started from uniform distributions of electrons and ions under the conditions corresponding to the neutral bulk plasma and prolonged to achievement of the steady state showing the sheath-presheath plasma structure. The super-particle motion equations are expressed in finite differences by the modified leap-frog explicit scheme. In the standard leap-frog method the particle positions and velocities are calculated at different time moments, which are shifted on half of the time step $\Delta t/2$. That creates errors in diagnostic of such parameters as a particle flux in sharply non-uniform and accelerated plasma as in a sheath, because in this case the flux is a product of the velocity and the density that correspond to different positions of a particle in the sheath. This problem is resolved by calculating of the particle velocity at each half time step that matches corresponding diagnostic moments for the particle position and velocity.

$$\begin{cases} \upsilon^{t+\Delta t/2}=\upsilon^{t}+\dfrac{q_j E\left(z^t\right)}{m_j}\dfrac{\Delta t}{2} \\ z^{t+\Delta t}=z^{t}+\upsilon^{t+\Delta t/2}\Delta t \\ \upsilon^{t+\Delta t}=\upsilon^{t+\Delta t/2}+\dfrac{q_j E\left(z^{t+\Delta t}\right)}{m_j}\dfrac{\Delta t}{2} \end{cases}, \tag{2.1.23}$$

where E is the local electric field. As easy to see this scheme preserves the accuracy order and stability of the standard leap-frog method due to keeping of the same relation

$$\upsilon^{t+\Delta t/2}=\upsilon^{t-\Delta t/2}+\frac{q_j E\left(z^t\right)}{m_j}\Delta t\,, \tag{2.1.24}$$

but adds two more operations at each time step, which are, nevertheless, have little impact on total calculation time, because other operations for Monte-Carlo collisions and diagnostics take much longer time. The diagnostic includes calculations of the spatial profiles of the densities, fluxes and flow velocities, the velocity distribution functions and the mean energy of all plasma components in three velocity dimensions as well as the spatial potential distribution and the time behavior at the selected points. The time behavior diagnostic allows us to check the achievement of a steady state and control numerical instabilities with the level of plasma oscillations. All spatial profiles are obtained in the steady state and are averaged over the time interval that exceeds several tens of the ion plasma oscillation periods. Typical time of one simulation comes to a few hundreds periods of the plasma ion oscillations.

2.1.3 Simulation results and comparison with theory

In order to check the correctness of the code we simulated the collisionless sheath without any elementary processes and compared them with the theoretical results described in Section 2.1.1. The simulation results of the collisionless sheath are shown in Fig.2.1.3 for the ratio of ion-to-electron temperature $T_i/T_e = 1/8$, the mass ratio $m_i/m_e = 64$ and the half-Maxwellian ion and electron influxes with the density ratio $n_{e0}^{(+)}/n_{i0}^{(+)} = 0.5069$ that implies quasi-neutrality of the bulk plasma. The wall was set floating and for the given above plasma parameters its theoretical potential is $e\varphi_{w,fl}/T_e = -2.44$. In Fig.2.1.3(a), the simulated spatial potential profile is shown. As we can see, the simulated floating wall potential coincides with the theoretical value. The potential profile is monotonically decreasing that corresponds to the theoretical condition. The drop of potential at the bulk plasma boundary is caused by the specific ion velocity distribution function that does not satisfy the Bohm criterion [24] and has zero velocity ions in spite of physical sheath edge conditions [21], therefore, the electron sheath is formed to accelerate ions. For the purpose of the test it doesn't play role, because such behavior corresponds to the theoretical solution with the given boundary conditions. In Fig.2.1.3(b), the time evolution of the wall potential and the potential at the middle point are plotted, where $\lambda_D \equiv \sqrt{\varepsilon_0 T_e / n_0 e^2}$ is the Debye length at the boundary of the bulk plasma. They oscillate in the steady state with the plasma

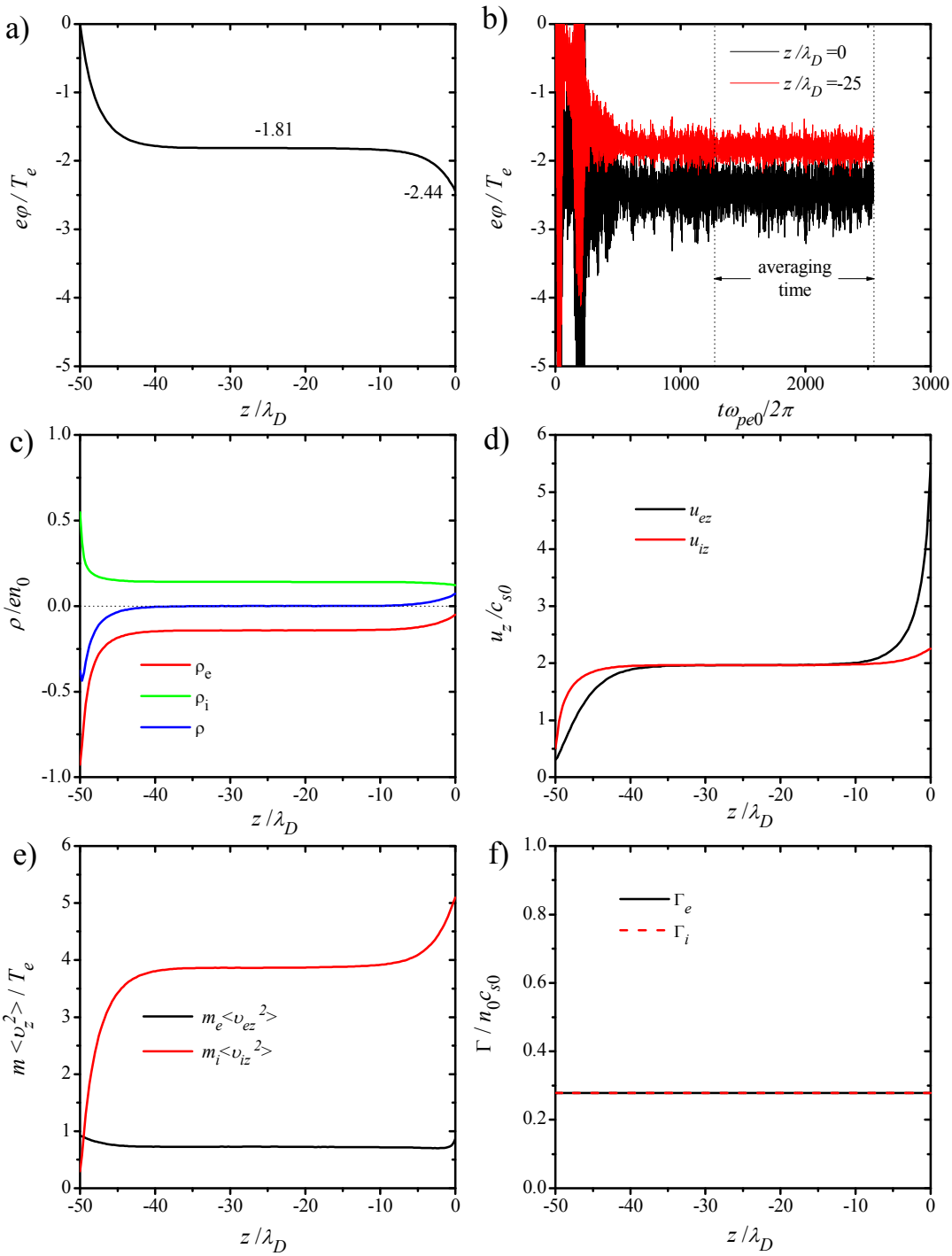

Fig. 2.1.3 *Simulation results of the collisionless sheath for the ion to electron temperature ratio* $T_i/T_e = 1/8$, *the mass ratio* $m_i/m_e = 64$ *and the half-Maxwellian ion and electron influxes with the density ratio* $n_{e0}^{(+)}/n_{i0}^{(+)} = 0.5069$ *at the* $z/\lambda_D = -50$, $\lambda_D \equiv \sqrt{\varepsilon_0 T_e / n_0 e^2}$ *is the Debye length at the boundary of the bulk plasma.*

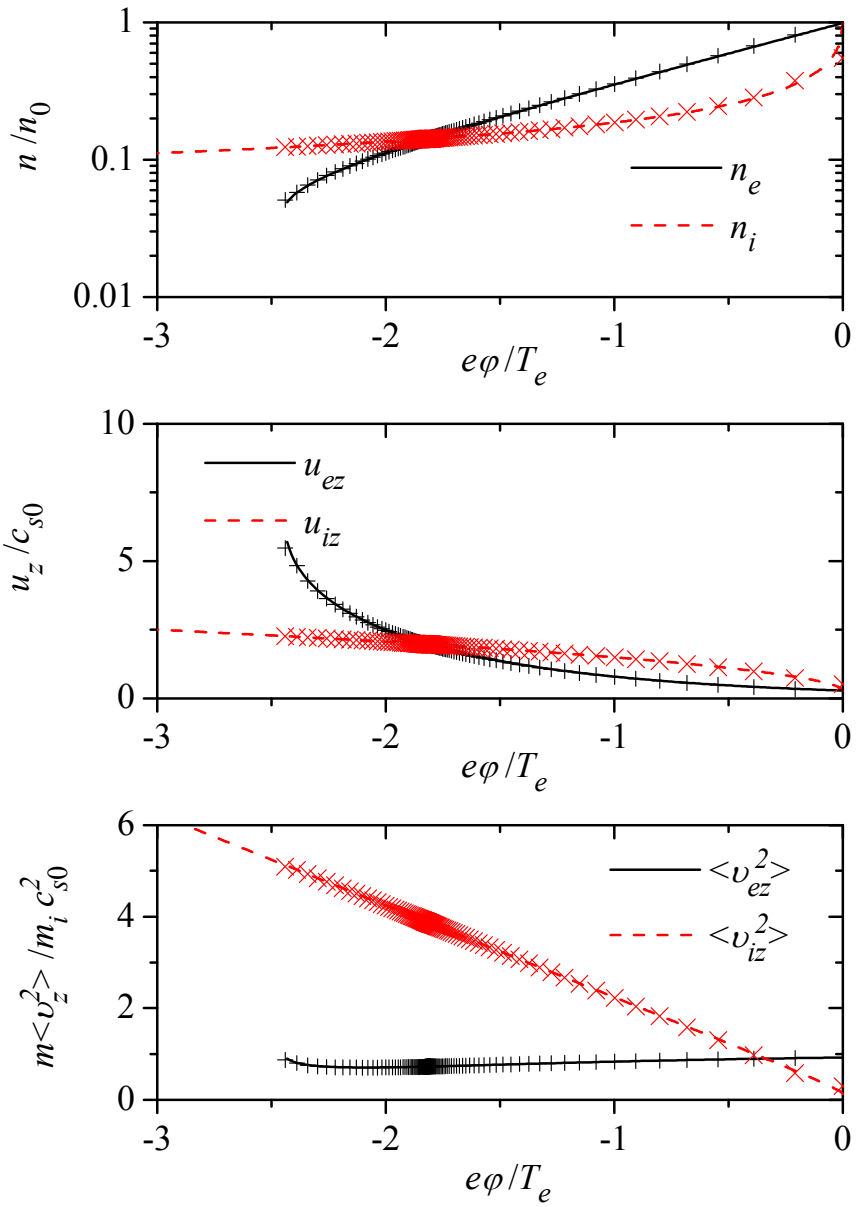

Fig. 2.1.4. *Comparison of the simulated (crosses) and the theoretical (lines) values of the electron and ion densities, flow velocities and mean kinetic energies as functions of the local potential. The plasma parameters are the same as in Fig.2.1.3.*

electron frequency and the amplitude of order of the electron temperature that confirms the stability of the simulation. The averaging time period is shown by the vertical dotted lines. The time averaged spatial profiles of the charge densities, the flow velocities, the mean kinetic energies and the fluxes are presented in Fig.2.1.3(c-f), respectively, where the brackets represent an ensemble averaging. We can see the sheaths structure in this case with the electron sheath near the bulk plasma, the quasi-neutral region in the middle of the system and the Debye sheath near the wall. The

electron and ion fluxes are equal each other that should be expected for the floating wall condition and are constant over the whole system as long as there are no particles sources and sinks. The agreement between the simulation results and the theoretical solutions is confirmed by Fig.2.1.4, where the electron and ion densities, the flow velocities and the mean kinetic energies are plotted as functions of the local potential. The crosses on the figure shows the simulated values and the lines are the theoretical solutions. As we can see, there is excellent agreement for all parameters. The theoretical curves for the electron and ion densities show that for the shallow potentials near the bulk plasma boundary, the electron density is higher than the ion one and an electron sheath should be formed for the injected half-Maxwellian ions without collisions. Further, there is the charge-neutrality point, which corresponds to the shelf on the potential profile, and the ion sheath. The electron velocity distribution function inside the sheath is strongly affected by the truncation effect that causes sharp increase of the electron flow velocity. The obtained results confirm the validity of the developed simulation code and provide additional information on the boundary conditions at the bulk plasma and the effect of the truncation of the electron velocity distribution function.

The more realistic sheath simulations can be carried out when we take into account the presheath formation due to ionization of neutrals and provide an initial ion flow velocity at the bulk plasma boundary to avoid the electron sheath appearance.

Let's consider the plasma that is close to parameters of the divertor plasma in fusion devices. The real values of the temperature of electrons and ions in the bulk plasma were chosen $T_e = T_i = 10\,\text{eV}$ and the plasma density was $n_0 = 10^{12}\,\text{cm}^{-3}$. Due to difficulties of a particle simulation with a large plasma volume that requires vast computation resources we took the length of the simulated system $L_s = 100\lambda_D$, where $\lambda_D = \sqrt{\varepsilon_0 T_e / n_0 e^2} = 23.5\ \mu\text{m}$ is the bulk electron Debye length, which still significantly exceeds the expected sheath width of order a few Debye lengths. The elementary process accounted here was the electron impact ionization of neutral hydrogen. With the purpose of getting the reliable ionizing presheath, which length is order of ionization mean free path, fitted into the simulated system we would effectively increase the neutral gas density that was $n_a = 10^{15}\ \text{cm}^{-3}$ with the temperature $T_a = 0.025\,\text{eV}$, which corresponds to the room temperature of 20˚C.

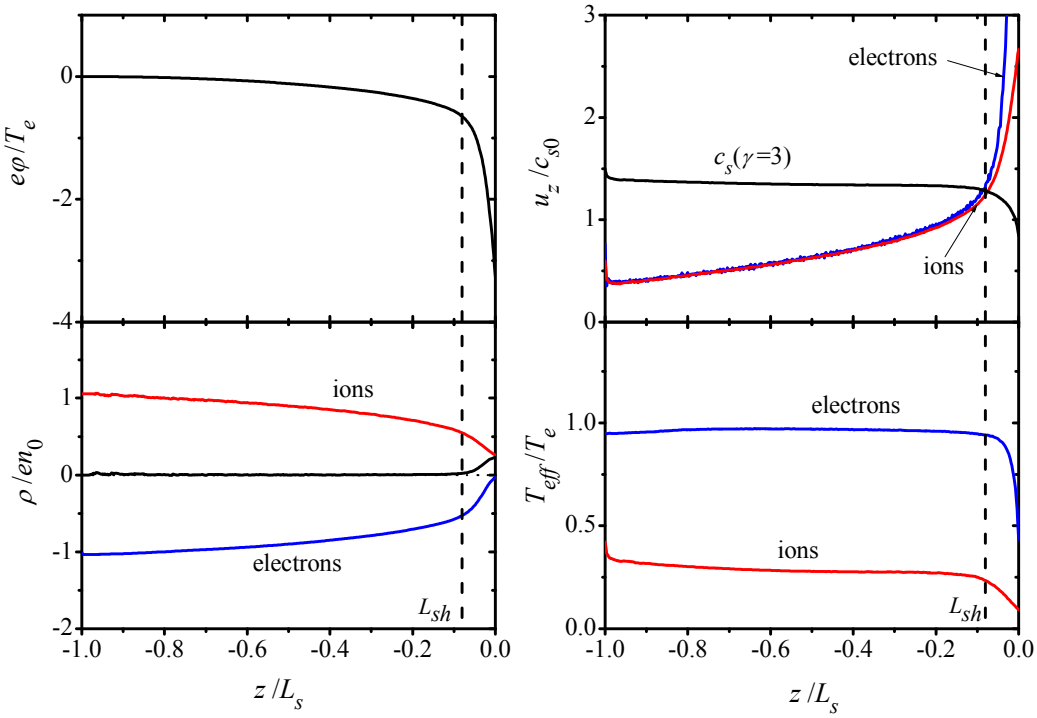

Fig. 2.1.5 *Spatial profiles of the simulated potential, electron and ion densities, flow velocities and effective temperatures in the Debye sheath and the presheath near the floating wall.*

Simulated spatial distributions of the electric potential, the charge densities, the flow velocities and the effective temperatures $T_{eff} \equiv m\left(\left\langle \upsilon_z^2 \right\rangle - \left\langle \upsilon_z \right\rangle^2\right)$ of electrons and ions are shown in Fig.2.1.5. We can see the monotonic potential distribution in the system that includes the positively charged sheath and the quasi-neutral presheath. As expected, the largest part of the potential drop between the floating plate and the bulk plasma appears in the Debye sheath region. The potential drop at the bulk plasma boundary was eliminated by the selected shift velocity of the injected Maxwellian ion velocity distribution function. Inside the Debye sheath all parameters of the plasma significantly change due to sharp acceleration of ions and modification of the electrons velocity distribution function. In contrast, the ionizing presheath region has the weak electric field, the almost constant effective temperatures of electrons and ions and gradual acceleration of ions toward the plate up to the sound speed accompanied with decrease of the density. According to the Bohm criterion [21,24] we can define the sheath edge as the position, where the ion flow velocity equals to the local ion sound speed

$$c_s(z) = \sqrt{\frac{T_e(z) + \gamma T_i(z)}{m_i}}, \tag{2.1.25}$$

where γ is the ratio of the specific heat at a constant pressure to that at a constant volume, for the one-dimensional adiabatic case $\gamma = 3$. The simulated spatial distribution of the ion sound speed presented in Fig.2.1.5 normalized by $c_{s0} = \sqrt{T_e / m_i}$, where the obtained position of the sheath edge is indicated as L_{sh}. The obtained value of L_{sh} is $5.4\lambda_{D,sh}$, where $\lambda_{D,sh} = 1.36\lambda_D$ is the electron Debye length at the sheath edge, its value is also simulated.

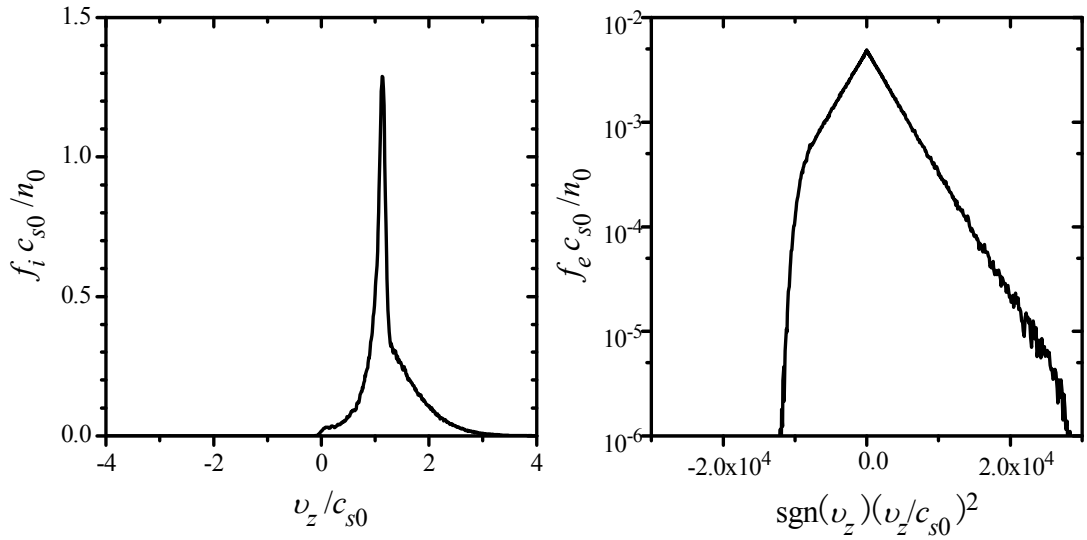

Fig. 2.1.6 *Simulated velocity distribution functions of the ions (left) and the electrons (right) at the sheath edge position* $z / L_s = L_{sh} / L_s = 0.074$.

Due to the absorption of the high-energy electrons, the negative velocity tail of the electron distribution function is absent and the electron effective temperature and the electron density are reduced. We can observe this effect in Fig.2.1.6, where the simulated ions and electrons distribution functions at the sheath edge are shown. Two groups of ions were formed in the ion velocity distribution function: the ions injected from the bulk plasma and the ones created by ionization of hydrogen atoms, both of which were accelerated by the presheath potential drop. Assuming that the slowest ions injected from the bulk plasma initially have zero velocity that further accelerated in the presheath, we can approximately find the part of the injected ions in the total ion density at the sheath edge. Such estimation shows that about half of the ions at the sheath edge was injected and another half was created by ionization. As can be seen,

acceleration of the ions leads to narrowing of their velocity distribution function that allows us to neglect their temperature as the first approximation.

Therefore, the simulation gave us spatial distributions of the plasma parameters in the whole system including the Debye sheath and the ionizing presheath. The obtained potential distribution, the electron and ion densities, the flow velocities and the effective temperatures can be used further for the analysis of the dust particle motion in the boundary plasma.

2.2 Behavior of a dust particle

Here we will consider the one-dimensional model of a single spherical dust particle behavior in a boundary plasma assuming that the plasma is not affected by the dust particle. When immersed into the plasma a dust particle becomes a small floating probe that absorbs plasma charges and can move or levitate under effect of an electrostatic force and other forces such as an ion drag force or a gravitational force. In our case, the dynamics of the dust particle is described by the equations of charging and motion with the initial conditions implying the dust particle placed on the wall with zero velocity. The conditions, under which the dust particle can be released from the wall, will be also analyzed in details in this section. In order to solve the dust dynamics equations we need to know the currents and forces acting on the dust particle, which depend on the local plasma parameters and the dust charge. The distributions of the boundary plasma parameters were simulated in the previous section and the currents and the forces we describe below.

2.2.1 Model: charging and forces

The charging of a dust particle in a plasma is a fundamental problem that is related to the plasma probe theory. Usually, a dust particle in a plasma can be considered as a floating probe accumulating electron and ion currents on it. As the electron mass is small, electron velocities are high and the electron current to the uncharged dust particle exceeds the ion current and the dust particle obtains a negative charge. This process of charging continues until the negative charge of the dust particle, which is repulsive for electrons and attractive for ions, will not equalize the

currents and further the equilibrium dust charge will not change significantly. Note that the equilibrium dust charge in the steady state still can vary due to discrete nature of the absorbed charges, which may be important for very small dust particles, and fluctuations of the plasma parameters. The repulsion of the electrons and the attraction of the ions create a plasma sheath around the dust particle, which modifies potential distribution and trajectories of plasma particles around the dust particle and requires the solution of the Poisson's equation. Thus, the problem of dust charging is self-consistent and is not solved in a general case. It becomes even more complex if a dust particle is placed in a plasma flow or an external non-uniform electric field like in a sheath. For the analysis of dust dynamics we need to simplify the situation to describe the dust charging analytically apart a self consistent computer simulation. The Orbital Motion Limited (OML) theory [41,42] gives us the possibility to describe the charging current to a spherical dust particle. This theory does not consider a self-consistent sheath structure around the dust particle, instead it uses the energy and the angular momentum conservation equations to obtain the absorption cross section of an electron or an ion by the dust particle. The cross section corresponds to the grazing dust surface trajectory of an electron or an ion that has the maximal impact parameter among absorbed particles. This consideration is valid only if the potential distribution around the dust particle is spherically symmetrical and does not allow the existence of trapped ion trajectories. That is possible if the potential is decreasing toward the dust particle not faster than approximately $1/r^2$ [42,44]. Other limitation is appearance of an effective potential barrier [43,45] due to specific competition between the electric field in the screened dust potential and the centrifugal force. The barrier appears for a big dust particle in comparison with the screening length. However, the OML theory was proved to be accurate enough for the most situations [45]. Other available theories have more strict limitations as the ABR (Allen, Boyd, Reynolds) theory [47] is applicable for low energy ions and the theory by Bohm, Burhop and Massey for the limit of $\lambda_D \to 0$. Also, all these theories do not take into account a magnetic field, secondary or photo emissions etc., which are beyond our consideration at present and can be included in future. Therefore, the OML theory was used here to describe the absorption of plasma particles by the spherical dust particle. It gives the following expressions for the absorption cross section of an electron or an ion

$$\sigma_{e,i} = \pi R_d^2 \left(1 - \frac{Q_d q_{e,i}}{2\pi \varepsilon_0 R_d m_{e,i} \upsilon_{e,i}^2} \right), \tag{2.2.1}$$

where R_d is the radius of the dust particle, Q_d is its charge, $\upsilon_{e,i}$ is the incident velocity of the absorbed electron or ion, and $q_e = -e$. If the velocity distribution functions of electrons and ions are known then we can calculate the charging currents. As we saw in previous Section 2.1.3, the ions are highly accelerated toward the wall by the sheath and presheath potential drops, therefore we can neglect an ion temperature and describe the ions as monoenergetic with the local flow velocity u_{iz}. The electron distribution function is assumed Maxwellian with the effective temperature T_e. Thus, the ion and electron currents to the negatively charged dust particle can be found as following

$$\begin{aligned} I_i(z) &= \pi R_d^2 \Gamma_i(z) q_i \left(1 - \frac{Q_d q_i}{2\pi \varepsilon_0 R_d m_i u_{iz}^2(z)} \right) \\ I_e(z) &= -\pi R_d^2 e n_e(z) \sqrt{\frac{8T_e(z)}{\pi m_e}} \exp\left(\frac{Q_d e}{4\pi \varepsilon_0 R_d T_e(z)} \right) \end{aligned}, \tag{2.2.2}$$

and in the case of a positively charged dust particle

$$\begin{aligned} I_i(z) &= \pi R_d^2 \Gamma_i(z) q_i \left(1 - \frac{Q_d q_i}{2\pi \varepsilon_0 R_d m_i u_{iz}^2(z)} \right) \\ I_e(z) &= -\pi R_d^2 e n_e(z) \sqrt{\frac{8T_e(z)}{\pi m_e}} \left(1 + \frac{Q_d e}{4\pi \varepsilon_0 R_d T_e(z)} \right) \end{aligned}. \tag{2.2.3}$$

The local equilibrium charge $Q_{d,eq}$ of the dust particle can be found from the equation

$$I_i(Q_{d,eq}, z) + I_e(Q_{d,eq}, z) = 0. \tag{2.2.4}$$

If for the initially uncharged dust particle $Q_d = 0$ the electron current exceeds the ion current, so the condition $e n_e(z) \sqrt{\frac{8T_e(z)}{\pi m_e}} > q_i \Gamma_i(z)$ is fulfilled, then the dust particle can have a negative equilibrium charge. This condition is easily satisfied for the most situations due to the very small electron mass until an electron density is too low as for example in a very deep negative sheath potential. The last situation may be realized near a highly biased wall with an external negative voltage applied.

During the motion the dust particle experiences changing of the surrounding plasma parameters and if the motion is fast in comparison to the dust charging

time τ_{ch}, then the dust particle may not reach the local equilibrium charge at the every position that is called the delayed charging effect. The dust charging time can be estimated using the perturbation method. Let's write the non-equilibrium dust charge as $Q_d = Q_{d,eq} + \Delta Q_d$ then the dust charging equation is

$$\frac{d\,\Delta Q_d}{d\,t} = I_i\left(Q_{d,eq} + \Delta Q_d\right) + I_e\left(Q_{d,eq} + \Delta Q_d\right). \tag{2.2.5}$$

This equation can be linearized when the deviation of the charge is small $\frac{\Delta Q_d}{4\pi\,\varepsilon_0 R_d T_e(z)} << 1$ and taking into account equation (2.2.4) we will get

$$\frac{d\,\Delta Q_d}{d\,t} = -\left(\frac{n_i(z) R_d q_i^2}{2\varepsilon_0 m_i u_{iz}(z)} + \frac{n_e(z) R_d e^2}{\varepsilon_0\sqrt{2\pi\, m_e T_e(z)}}\right)\Delta Q_d\,. \tag{2.2.6}$$

The solution of equation (2.2.6) in the form $\Delta Q_d \propto \exp\left(-t/\tau_{ch}\right)$ gives the charging time

$$\frac{1}{\tau_{ch}} = \frac{n_i(z) R_d q_i^2}{2\varepsilon_0 m_i u_{iz}(z)} + \frac{n_e(z) R_d e^2}{\varepsilon_0\sqrt{2\pi\, m_e T_e(z)}}\,. \tag{2.2.7}$$

The delayed charging effect may be important if the dust charging time is shorter than the characteristic time of the dust motion, which we will discuss in the following sections.

Further, let's consider the forces acting on the dust particle. As long as the charged dust particle is placed in the sheath with the local electric field $E(z)$, it experiences the electrostatic force, which with the assumption of undisturbed plasma in our one-dimensional model is simply

$$F_E(z,t) = Q_d(z,t)\,E(z). \tag{2.2.8}$$

Another force acting on the dust particle is the ion drag force. It includes two components: the first is the ion drag force due to absorption of ions by the dust particle $F_{i,ab}(z,t)$ and the second is the ion drag force due to scattering of ions $F_{i,sc}(z,t)$. The ion absorption drag force can be calculated in the same way as the ion current assuming the monoenergetic ion velocity distribution function

$$F_{i,ab}(z,t) = \pi R_d^2 \Gamma_i(z) m_i u_{iz}(z)\left(1 - \frac{Q_d(z,t)\,q_i}{2\pi\,\varepsilon_0 R_d m_i u_{iz}^2(z)}\right). \tag{2.2.9}$$

Here we neglected the dust particle's velocity in comparison to the ion flow velocity and substituted the relative ion-dust velocity with the ion one.

The ion drag force due to scattering can be written as

$$F_{i,sc}\left(z,t\right)=\frac{Q_d^2\left(z,t\right)q_i^2 n_i\left(z\right)\ln\Lambda_d}{4\pi\,\varepsilon_0^2 m_i u_{iz}^2\left(z\right)}, \tag{2.2.10}$$

where $\ln\Lambda_d$ is the Coulomb logarithm for the dust particle. This force is obtained from the classical momentum transfer cross section for the Coulomb scattering [76]. The lower limit of the integral of the Rutherford scattering is the smallest scattering angle that corresponds to the dust screening radius $\left(R_d+\lambda_D\right)$ and the upper limit is the largest scattering angle that corresponds to the absorption radius R_{abs}. The shielding length is usually assumed equal to the electron Debye length λ_D [49,65] and according to the OML theory $R_{abs}=R_d\sqrt{1-\frac{Q_d q_{e,i}}{2\pi\,\varepsilon_0\,R_d m_{e,i}\upsilon_{e,i}^2}}$. Correspondingly to the classical consideration [13,65] the Coulomb logarithm for the dust particle is the weak function of the dust particle's radius and the Debye length

$$\ln\Lambda_d=\ln\left(\frac{\left(R_d+\lambda_D\right)^2+b_0^2}{R_{abs}^2+b_0^2}\right),\quad b_0\equiv\frac{Q_d q_i}{4\pi\,\varepsilon_0 m_i u_{iz}^2}. \tag{2.2.11}$$

Here we neglect the dependence of the Coulomb logarithm on the dust radius and assume that it is constant. For the simulated plasma parameters we take $\ln\Lambda_d=3$ that is smaller value than a usual plasma Coulomb logarithm integrated from the zero impact parameter. The dust velocity is also neglected here in respect to the ion flow velocity.

When the dust particle is placed close to the wall (at the distance less than the screening radius) the distribution of the wall charges is affected by the dust particle creating the electrostatic force directed toward the wall. We approximately describe this force using the electrostatic image method symmetrically placing the point charge equal with an opposite sign to the dust charge at the same distance from the wall as for the dust particles center. That assures the normal electric field at the wall surface neglecting the plasma and the dust particle polarization effects. As the dust charge is screened by a plasma, we can neglect this force for the dust dynamics in plasmas, but we account it for the release condition analysis when the dust particle is placed on the wall. Thus, the electrostatic image force for the dust on the wall is equal to

$$F_m = \frac{Q_d^2}{4\pi\varepsilon_0 \left(2R_d\right)^2}. \tag{2.2.12}$$

The gravitational force acting on the dust particle is arbitrary directed relatively to the wall normal direction depending on the wall orientation to the horizontal line. For the vertical walls the projection of the gravitational force on the wall normal is zero and in our one dimensional analysis it can be omitted. In other cases the projection can be directed both toward the wall and in the opposite direction. We consider two limit cases of the bottom position of the horizontal wall and the upper position. Then the gravitational force will be $F_g = \pm m_d g$, where m_d is the dust particle's mass, and g is the free fall acceleration. The plus sign means the gravitational force directed toward the wall and the minus sign means from the wall direction. For the case of solid spherical dust particle

$$F_g = \pm\frac{4}{3}\pi R_d^3 \rho_d g, \tag{2.2.13}$$

where ρ_d is the mass density of the dust particle.

In our consideration there is no flow of the neutral atoms and they do not provide a directed drag force, but cause dissipative friction force. Because of the low neutral gas temperature and the small dust particle velocity relative to the ion flow velocity, the neutral frictional force is negligible in comparison to the ion drag force. Therefore, we neglect the neutrals frictional force in the short time of one dust oscillation period and just point the dumping effect of the neutrals friction. The forces described above are included in the total force and used for solution of the dust motion equation

$$F = F_E + F_{i,ab} + F_{i,sc} + F_m + F_g. \tag{2.2.14}$$

We have expressions for the currents and forces to the dust particle, where the independent parameters are the local plasma parameters, which are simulated or can be estimated theoretically, and the dust radius R_d. Numerical solutions of dynamics equations (2.2.1) for different radii of the dust particle can show their possible trajectories in the boundary plasma. In the next section we analyze the solutions and the initial conditions on the wall.

2.2.2 Release from wall: the first critical radius

Now, let's discuss the situation when the dust particle is placed on the wall initially. We are interested, first of all, what is the dust charge and when the dust particle can leave the wall and move into the plasma. The charge of the dust particle on the wall is no more directly obtained from the floating condition of equal currents of electrons and ions to the dust particle. Instead, the dust charge is determined by the wall surface charge density as long as the conductive dust particle is in electrical contact with the wall. In the absence of the dust particle, the wall surface charge density is directly related to the electric field at the wall E_w. From the Gauss theorem for the plane geometry and the zero electric field inside the conductive wall we know the wall surface charge density $\sigma_w = -\varepsilon_0 E_w$. If the dust particle is a disk (circle element of the wall) then its charge would be the product of the dust surface and the wall surface charge density $Q_d = S_d \sigma_w = -\pi R_d^2 \varepsilon_0 E_w$. In the case of the spherical dust particle we can not just write $Q_d = S_d \sigma_w = -4\pi R_d^2 \varepsilon_0 E_w$ because the electric field will be disturbed by the dust particle. Therefore, the dust particles charge on the wall is described as

$$Q_d = -\xi_q \, \pi R_d^2 \, \varepsilon_0 E_w , \tag{2.2.15}$$

where ξ_q is the form factor taking into account the effect of dust shape and the redistribution of the surface electric field due to the presence of the dust particle. The form factor can be found analytically for simple situations by solution of the Laplace equation for the disturbed electric field. For the case of the conductive sphere placed on the wall in a uniform external electric field, it was shown [77] that the value of the form factor is

$$\xi_q = \frac{2}{3}\pi^2 \approx 6.58 . \tag{2.2.16}$$

Note that this value is larger than that of a spherical surface $\xi_q = 4$, thus, on average the normal electric field on the dust surface is enhanced due to polarization of the dust in comparison with the undisturbed electric field at the wall surface. Later, when we consider the two dimensional model, we include effects of the non-uniform external electric field and analyze the plasma effect. Hence, the initial dust particle charge on the wall expressed as (2.2.15) is a function of the dust radius and the electric field at

the wall. When the particle is released from the wall it recharges to the floating potential as the electric contact with the wall is lost.

The condition, when the dust particle can leave the wall, should assume that the total force acting on the particle on the wall position is negative, i.e. directed from the wall

$$F\left(z=0\right)=F_E+F_{i,ab}+F_{i,sc}+F_m+F_g<0\,. \tag{2.2.17}$$

Here we neglected any molecular forces bounding the dust particle with the wall, because it requires including roughness and atomic structures of the surfaces that is beyond our consideration.

All the forces included in the releasing condition (2.2.17) are functions of the dust radius and the plasma parameters at the wall. Thus, if the plasma parameters are fixed then the releasing condition can be solved in respect to the dust radius. As the direction of the gravitational force is arbitrary we consider three cases: the gravitational force is zero (vertical wall), negative (upper wall) and positive (lower wall) corresponding to expression (2.2.13). After substitution of the initial dust charge (2.2.15) into the electric force, we find

$$F_E\left(z=0\right)=-\xi_q\,\pi\,R_d^2\,\varepsilon_0 E_w^2\,. \tag{2.2.18}$$

The ion drag forces on the dust particle at the wall position are

$$F_{i,ab}\left(z=0\right)=\pi\,R_d^2\Gamma_{iw}m_i u_{izw}\left(1+\frac{\xi_q R_d E_w q_i}{2m_i u_{izw}^2}\right),\text{ and} \tag{2.2.19}$$

$$F_{i,sc}\left(z=0\right)=\frac{\xi_q^2\pi\,R_d^4 E_w^2 q_i^2 n_{iw}\ln\Lambda_d}{4\,m_i u_{izw}^2}\,. \tag{2.2.20}$$

The electrostatic image force is rewritten as

$$F_m=\frac{\xi_q^2\pi\,R_d^2\varepsilon_0 E_w^2}{16}, \tag{2.2.21}$$

and the gravitational force (2.2.13) does not change. As we can see, all the forces are power dependent on the dust radius R_d, where the highest is the fourth order power for the ion scattering force and the lowest one is the second order. Therefore, the dust particle release condition (2.2.17) finally becomes the second order polynomial inequality

$$\frac{F\left(z=0\right)}{\pi\,R_d^2\,m\,\Gamma_{iw}u_{izw}}=A\,R_d^2+B\,R_d+C<0\,, \tag{2.2.22}$$

where

$$A = \left(\frac{\xi_q E_w q_i}{2 m_i u_{izw}^2} \right)^2 \ln \Lambda_d \,, \tag{2.2.23}$$

$$B = \frac{\xi_q E_w q_i}{2 m_i u_{izw}^2} \pm \frac{4}{3} \frac{\rho_d g}{m_i \Gamma_{iw} u_{izw}} \,, \tag{2.2.24}$$

$$C = 1 + \frac{\varepsilon_0 E_w^2}{m_i \Gamma_{iw} u_{izw}} \left(\frac{\xi_q^2}{16} - \xi_q \right). \tag{2.2.25}$$

Inequality (2.2.22) can have two, one or no real solutions depending on the relation between the coefficients A , B and C. The RHS of inequality (2.2.22) is a concave shape parabola on R_d scale (Fig.2.2.1), because, as easy to see, in all cases $A > 0$. Physically it means that the very large particles can not leave the wall due to the large positive ion scattering force.

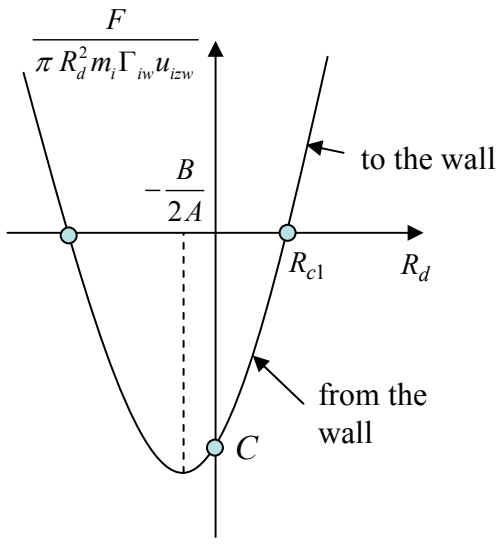

Fig. 2.2.1 *Parabolic dependence of the normalized force on* R_d.

Let's consider the situation when the gravitational force is zero, where the dust particle is located on the vertical wall. In this case the coefficient B is positive and number of non-negative zeros of the condition's (2.2.22) LHS depends on the sign of the coefficient C: when $C > 0$, there are no positive solutions for R_d, and when $C \le 0$, there is one non-negative solution with the physical meaning.

The one non-negative solution is

$$R_{c1} = \frac{m_i u_{izw}^2}{\xi_q E_w q_i \ln \Lambda_d} \left[-1 + \sqrt{1 + 4 \ln \Lambda_d \left(\alpha_p - 1 \right)} \right] \,, \tag{2.2.26}$$

where

$$\alpha_p \equiv 1 - C = \frac{\xi_q \left(1 - \xi_q / 16 \right) \varepsilon_0 E_w^2}{m_i \, n_{iw} u_{izw}^2} . \tag{2.2.27}$$

Therefore, the non-negative solution (2.2.26) exists only when

$$\alpha_p \ge 1 . \tag{2.2.28}$$

We called R_{c1} the first critical dust radius. If the dust particle radius $R_d < R_{c1}$, the release condition (2.2.17) is satisfied and the dust particle can leave the wall, in the opposite case $R_d \geq R_{c1}$, the dust particle can not leave the wall. Thus, the first critical dust radius is the radius of the biggest released dust particle. As we noted, in the case $\alpha_p < 1$ there is no positive solution for the first critical dust radius and because all the coefficients A , B, and C in this case are positive, the total force acting on the dust particle will be positive, so the particle of any size can not leave the wall.

In order to understand when the condition (2.2.28) of the first critical dust radius existence is satisfied, we need to know plasma parameters at the wall. These parameters can be measured or simulated, but for getting more general conclusion let us theoretically estimate the electric field E_w, the ion density n_{iw} and flow velocity u_{izw} at the wall in the Debye sheath. The classical way is to use the Bohm theory [21,24] of the sheath, which assumes the vanishing electric field and the ion flow velocity equal to the ion sound speed $c_{s0} = \sqrt{T_e/m_i}$ at the sheath edge. We consider here the classical collisionless sheath with Maxwellian electrons formed in front of the biased wall with the given sheath potential drop φ_{sh}. After integrating of the Poisson's equation once and using the flux and the energy conservations for the ions, one arrives to

$$\frac{u_{izw}}{c_{s0}} = \sqrt{1 + \frac{2e\varphi_{sh}}{T_e}}, \tag{2.2.29}$$

$$n_{iw} = n_0 \left(1 + \frac{2e\varphi_{sh}}{T_e}\right)^{-1/2}, \tag{2.2.30}$$

$$E_w^2 = \frac{2n_0 T_e}{\varepsilon_0}\left(\sqrt{1 + \frac{2e\varphi_{sh}}{T_e}} + e^{-\frac{e\varphi_{sh}}{T_e}} - 2\right), \tag{2.2.31}$$

where n_0 is the ion density at the sheath edge. Now we have the plasma parameters near the wall expressed analytically via the sheath potential drop, the plasma density and the electron temperature at the sheath edge.

Fig.2.2.2 shows the electrostatic, the ion absorption drag, the ion scattering drag, the image and the total forces as functions of the normalized dust radius for the estimated plasma parameters according to formulae (2.2.29-31) with the sheath potential drop $e\varphi_{sh}/T_e = 10$, the dust form factor $\xi_q = 6.58$ and the dust Coulomb

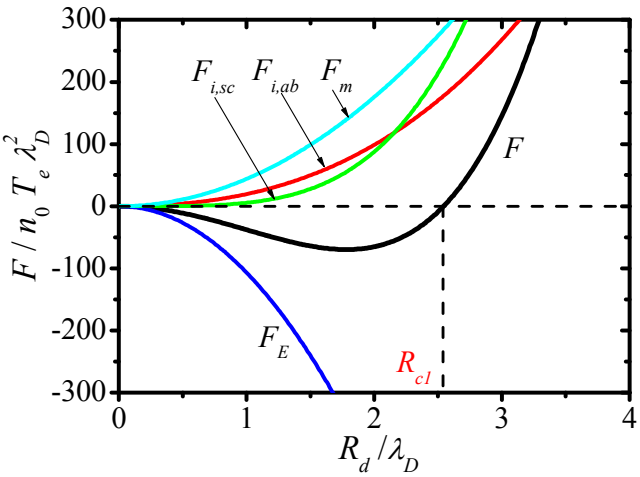

Fig. 2.2.2 *Forces acting on the dust particle on the wall position as functions of the normalized dust radius* R_d *for the spherical particle with* $\xi_q = 6.58$, *the dust Coulomb logarithm* $\ln\Lambda_d = 3$ *and* $e\varphi_{sh}/T_e = 10$. *The first critical dust radius corresponding to the total force equaled zero indicated as* R_{c1}.

logarithm $\ln\Lambda_d = 3$. Here and then we perform numerical calculations for the single charged hydrogen ions with $q_i = +e$. As we can see, the electrostatic force (2.2.18), which is parabolic on R_d, exceeds all other forces for the particles smaller than the first critical dust radius R_{c1}, so these particles can be released from the wall. With increasing of the size of dust particles the ion drag force increases faster than the electrostatic force and dust particles bigger than R_{c1} are pinned against the wall.

The dependence of the parameter α_p on the sheath potential drop is presented in Fig.2.2.3(a) using the obtained dependencies of the plasma parameters on φ_{sh} in the Bohm sheath model. The parameter α_p is a monotonically increasing function of φ_{sh} from zero, therefore, condition (2.2.28), which indicates the existence of the first critical dust radius, is satisfied when the sheath potential drop is larger than the threshold value $\varphi_{sh,th}$ corresponding to $\alpha_p = 1$. As shown in Fig.2.2.3(b), the first critical radius increases from zero at the threshold sheath potential drop to a few Debye lengths for deeper sheath potentials. For the potentials lower than the threshold one, no physical solutions for the first critical radius exist and the dust particles of any size are pinned against the wall with the ion drag forces.

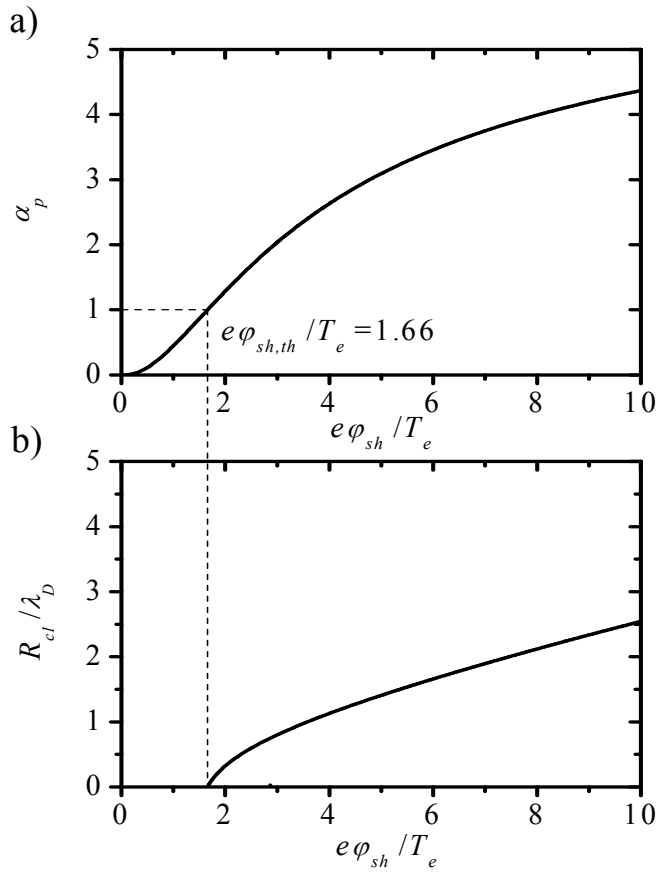

Fig. 2.2.3 *Dependence of the parameter* α_p *(a) and the first critical dust radius* R_{c1} *(b) on the sheath potential drop* φ_{sh} *in the Bohm sheath model. Here the parameters* $\xi_q = 6.58$ *and* $\ln\Lambda_d = 3$.

Thus, the region above the curve in Fig.2.2.3(b) corresponds to the pinned dust particles, and the region below the curve corresponds to the particles sizes and the sheath potentials when the dust particles can be released from the wall.

As can be seen from the definition of the parameter α_p (2.2.27), it is the ratio of the electric field pressure to the ion flow pressure. Hence, the condition of the first critical radius existence (2.2.28) means that the electrostatic pressure should be larger than the ion flow pressure at the wall. The value of the threshold sheath potential drop corresponds to the marginal equality of the pressures. The threshold potential $\varphi_{sh,th}$ can be found from the equation

$$\alpha_p \equiv \frac{\xi_q\left(1-\xi_q/16\right)\varepsilon_0 E_w^2}{m_i\, n_{iw} u_{izw}^2} = 2\,\xi_q\left(1-\xi_q/16\right)\left[1+\frac{e^{-e\varphi_{sh,th}/T_e}-2}{\sqrt{1+2e\varphi_{sh,th}/T_e}}\right]=1. \quad (2.2.32)$$

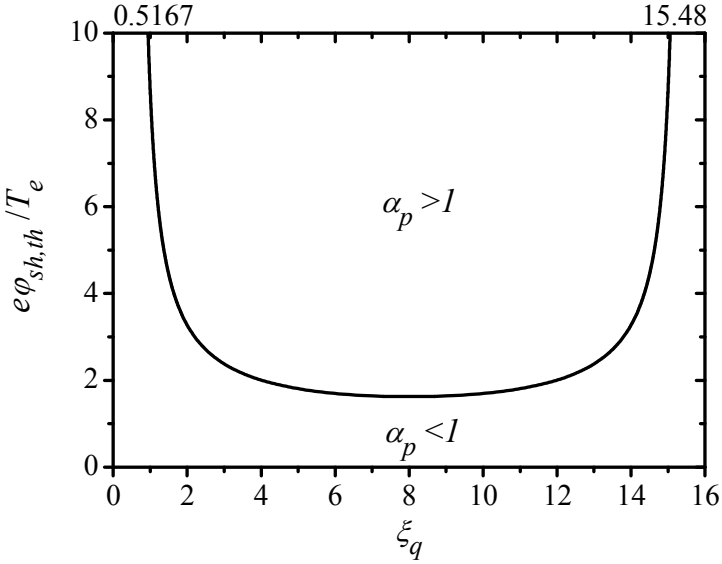

Fig. 2.2.4 *Threshold sheath potential drop as the function of the dust particle form factor in the Bohm sheath model.*

The solutions of this equation for different dust form factors are sown in Fig.2.2.4. As one can see, the threshold sheath potential drop weakly depends on the form factor for wide range of its values from around $\xi_q = 4$ to $\xi_q = 12$ including the value for the spherical dust particle $\xi_q = 6.58$. Thus, the threshold potential is not sensitive for the small deviations of the dust shape from the spherical one. Another point is that the threshold potential exists only in the range of the form factors $0.5167 \approx 8\left(1-\sqrt{7/8}\right) < \xi_q < 8\left(1+\sqrt{7/8}\right) \approx 15.48$ changing sharply near the limits. Outside this range of the form factor values the parameter α_p is less than unity and the first critical dust radius does not exist. Thus, all dust particles with the form factor outside the indicated range of values will be pinned against the wall. The lower limit of the range appears due to insufficient dust charge to release the dust particle from the wall and the upper limit is caused by the strong electrostatic image force as it is proportional to the square of the dust charge, while the electrostatic repulsive force depends on it only linearly.

The sheath potential drop can be controlled by the externally applied voltage to the wall. Generally, if we apply the voltage between two walls, the plasma potential will be still positive in respect to the both walls until the area of one wall will not be very small compare to another one or the secondary/photo electron emission is not strong. The dependence of the sheath potential drop on the externally applied voltage

can be obtained theoretically in the planar geometry (Appendix B) and satisfy the relation

$$\frac{\exp\left(-e\varphi_{sh}/T_e\right)}{1+erf\left(\sqrt{e\varphi_{sh}/T_e}\right)}\frac{S^{w1}}{S^{w2}}+\frac{\exp\left(-e\left(\varphi_{sh}+\varphi_{ext}\right)/T_e\right)}{1+erf\left(\sqrt{e\left(\varphi_{sh}+\varphi_{ext}\right)/T_e}\right)}=\sqrt{\frac{\pi\, m_e}{2\, m_i}}\left(1+\frac{S^{w1}}{S^{w2}}\right), \tag{2.2.33}$$

where φ_{ext} is the externally applied voltage to the wall "$w1$" in respect to the wall "$w2$", S^{w1} and S^{w2} are the areas of the two walls, respectively. The solutions of (2.2.33) are shown in Fig.B.3 (Appendix B).

Therefore, the first critical dust radius and the threshold potential are the functions of the externally applied voltage to the wall. It shows the possibility to control the size of the released dust particles or even suppress the dust releasing from the wall when the wall potential is below the threshold value.

Now the gravitational force is taken into account, at first, we consider the case when its direction is toward the wall. In this case, the coefficient B (2.2.24) remains positive and the release condition (2.2.22), as in the case without gravitational force, has one or no physical solutions for the first critical radius depending on the sign of the coefficient C (2.2.25). The first critical radius can be written then

$$R_{c1}=\frac{m_i u_{izw}^2}{\xi_q E_w q_i \ln\Lambda_d}\left[-\left(1+\Delta_g\right)+\sqrt{\left(1+\Delta_g\right)^2+4\ln\Lambda_d\left(\alpha_p-1\right)}\right], \tag{2.2.34}$$

where

$$\Delta_g=\frac{8}{3}\frac{n_0 T_e}{\xi_q E_w q_i n_{iw}\,\lambda_D}\delta_g, \tag{2.2.35}$$

and the dimensionless gravitational parameter δ_g is defined as

$$\delta_g\equiv\frac{\rho_d g\,\lambda_D}{n_0 T_e}=\frac{\rho_d g\;\varepsilon_0^{1/2}}{e\,n_0^{3/2}\,T_e^{1/2}}. \tag{2.2.36}$$

The parameter Δ_g after substitution of the electric field and the ion density on the wall according to (2.2.30-31) will be the following function of the dimensionless sheath potential drop

$$\Delta_g=\frac{8}{3\sqrt{2}\,\xi_q}\left(\frac{1+2e\varphi_{sh}/T_e}{\sqrt{1+2e\varphi_{sh}/T_e}+e^{-e\varphi_{sh}/T_e}-2}\right)^{1/2}\delta_g. \tag{2.2.37}$$

Thus, the gravity effect is localized and described only by the gravitational parameter δ_g. As we can see from (2.2.34), the condition for the first critical dust radius existence, $\alpha_p \geq 1$, is not modified. It means that the threshold sheath potential drop is also present and, moreover, its value is not affected by the gravitational force directed to the wall. Such independence of the threshold potential on the gravitational force can be explained if we note that it corresponds to the first critical dust radius approaching zero. Therefore, only the forces with the lowest second order dependence on the dust radius define the force balance near the threshold potential and the effect of gravitational force vanishes in this case due to cubic dust radius dependence.

In Fig.2.2.5, the dependence of the first critical dust radius on the sheath potential drop is shown when the gravitational force is directed toward the wall for various values of the gravitational parameter δ_g. As we can see, the stronger gravity is, the smaller the first critical radius is and the smaller the region of released dust particles becomes. That is physically reasonable, as the gravitational force in this case hampers the release of the particles. Also, one can see that the threshold potential is not affected by gravity as was discussed above. The gravitational parameter δ_g (2.2.36) depends not only on the dust mass density but also on the plasma parameters, so for the same dust particles the effect of the gravitational force on the first critical radius is smaller in dense and hot plasmas. For the carbon dust particles with $\rho_d = 2$ g/cm^3 and $g = 9.8$ m/s^2 we can obtain the estimation formula

$$\delta_g = \frac{9.09 \times 10^{17}}{n_0^{3/2}[\text{cm}^{-3}]\, T_e^{1/2}[\text{eV}]}. \tag{2.2.38}$$

Using this expression, the gravitational parameter δ_g for a typical density of the divertor plasma $n_0 = 10^{12}$ cm^{-3} and the electron temperature $T_e = 10$ eV is estimated as $\delta_g \approx 0.29$, hence the effect of the gravitational force is small, while for a typical processing plasma with $n_0 = 10^{10}$ cm^{-3} and $T_e = 3$ eV the gravitational parameter is $\delta_g \approx 525$ and the effect of the gravitational force becomes significant. As shown in Fig.2.2.6, when the gravitational parameter $\delta_g < 1$, the first critical dust radius is practically unaffected by the gravitational force and for $\delta_g > 10$ the first critical radius is inversely proportional to δ_g.

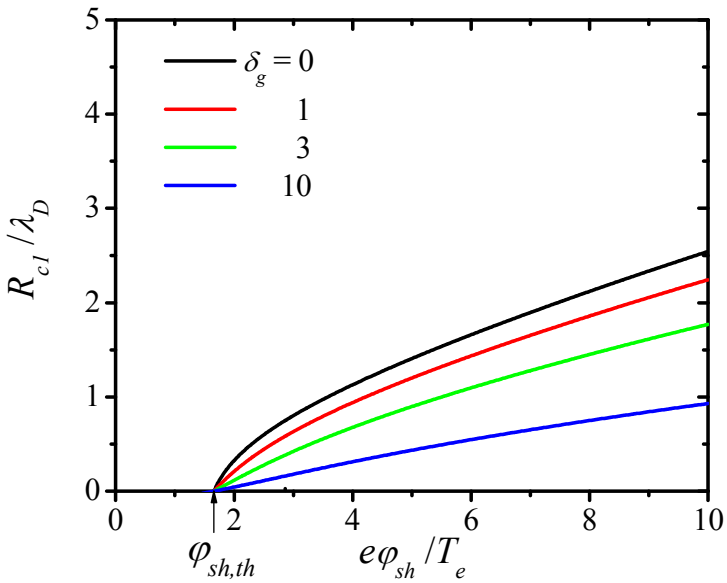

Fig. 2.2.5 *Dependence of the first critical dust radius on the sheath potential drop with the gravitational force directed toward the wall for various values of the gravitational parameter* δ_g *and the parameters* $\xi_q = 6.58$, $\ln \Lambda_d = 3$.

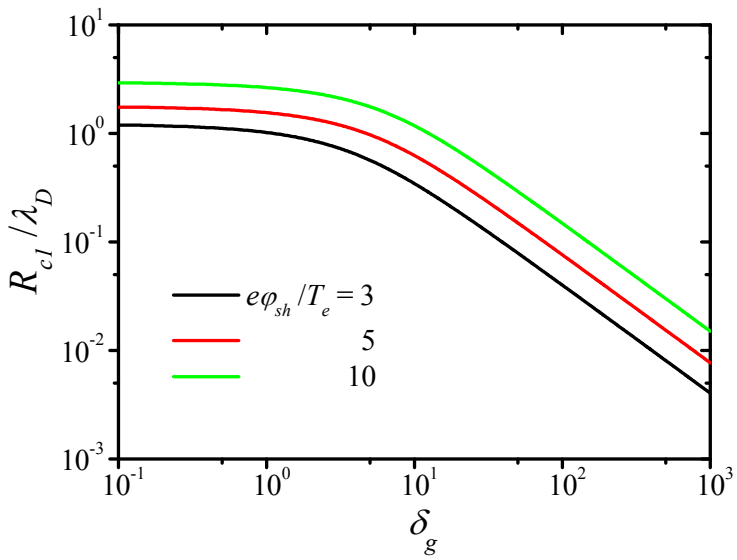

Fig. 2.2.6 *Dependence of the first critical dust radius on the gravitational parameter* δ_g *for the gravitational force directed toward the wall with various values of the sheath potential drop and the parameters* $\xi_q = 6.58$, $\ln \Lambda_d = 3$.

In the case of the gravitational force directed from the wall, the coefficient B (2.2.24) may be both positive and negative, thus there appears the releasing condition (2.2.22) can have two positive solutions for the first critical radius

$$R_{c1} = \frac{m_i u_{izw}^2}{\xi_q E_w q_i \ln \Lambda_d} \left[-\left(1-\Delta_g\right) \pm \sqrt{\left(1-\Delta_g\right)^2 + 4\ln\Lambda_d\left(\alpha_p - 1\right)} \right]. \qquad (2.2.39)$$

As can be seen from expression (2.2.39), in any case we have only one physical solution for the first critical radius when $\alpha_p \geq 1$. For $\alpha_p < 1$ the first critical radius has no solutions when the discriminant $D \equiv \left(1-\Delta_g\right)^2 + 4\ln\Lambda_d\left(\alpha_p - 1\right) < 0$ or $\Delta_g < 1$ and has two physical solutions R_{c1}^l and R_{c1}^u (R_{c1}^l smaller than R_{c1}^u) when $D > 0$ and $\Delta_g > 1$. Two values for the first critical radius mean that the dust particle will be released from the wall when its size is in between of them $R_{c1}^l < R_d < R_{c1}^u$ and pinned to the wall when the dust size is out of the range. Thus, the threshold sheath potential drop in this case exists, above which there is only one value of the critical dust radius. Below the threshold sheath potential two situations are possible depending on the gravitational parameter δ_g: no particles can leave the wall, or there is the range of released dust particle's radius in between two solutions of the critical radius. The threshold sheath potential does not depend on gravity as in the case of the positive gravitational force. The situation is illustrated in Fig.2.2.7, where the regions colored in green correspond to the released dust particles. We can see two regions of the released dust particles for the values of the gravitational parameter $\delta_g < 2.302$ that are merged when $\delta_g > 2.302$. There is a gap in the sheath potential values for the small gravitational parameters, where no dust particles can leave the wall even though the gravitational force is directed from the wall. When the gravitational parameter is large, there are dust particles that are released from the wall for any sheath potentials. For the special value of the gravitational parameter $\delta_g \approx 2.302$, the two regions of released dust particles and the two regions of the pinned particles can be clearly distinguished. There is a dominant force indicated in the left part of Fig.2.2.8 that prevails in each of the regions. In the right part of Fig.2.2.8 the absolute values of the forces are plotted for the selected dust radii. In the logarithmic scale of the figure, the largest force is dominant in some range of the sheath potentials. As we can see, the gravitational force is dominant for the large particle with $R_d / \lambda_D = 10$ in the released

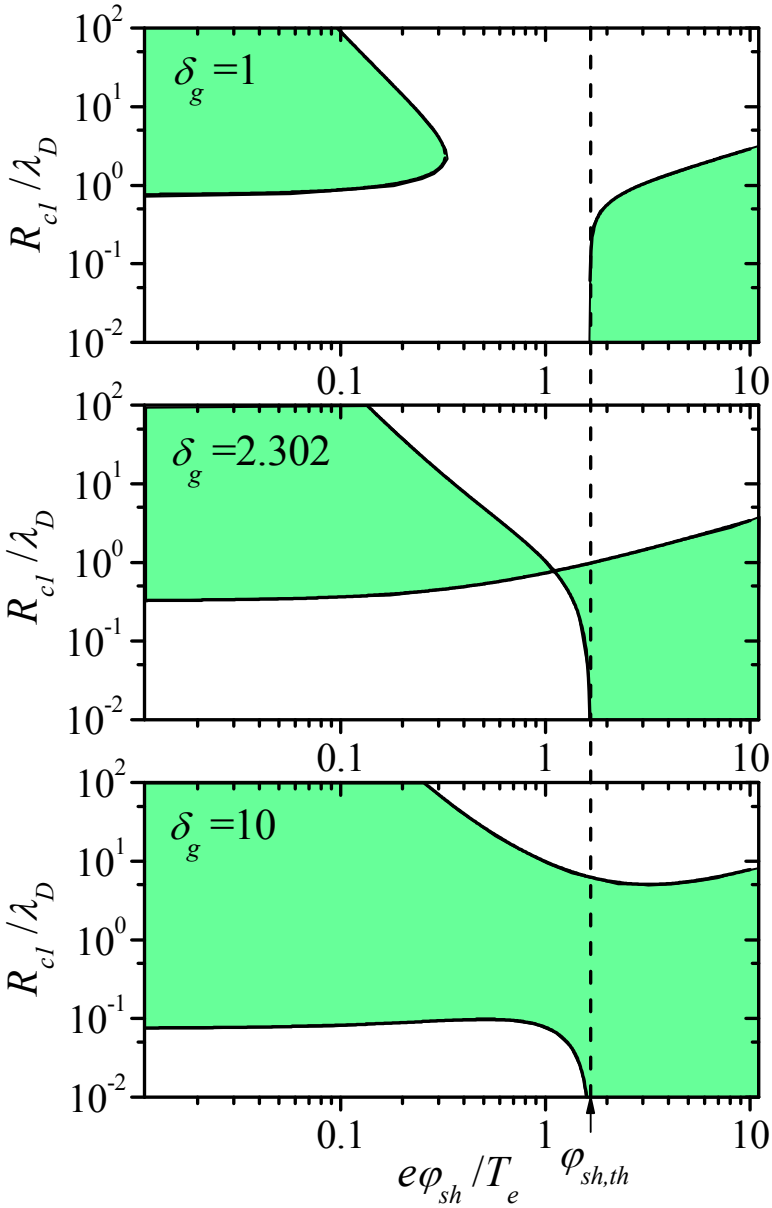

Fig. 2.2.7 *The first critical dust radius* R_{c1} *as a function of the sheath potential drop* φ_{sh} *for the case when the gravitational force is directed from the wall with various values of the gravitational parameter* δ_g *and parameters* $\xi_q = 6.58$, $\ln \Lambda_d = 3$. *The regions corresponding to the released dust particles are indicated in green color.*

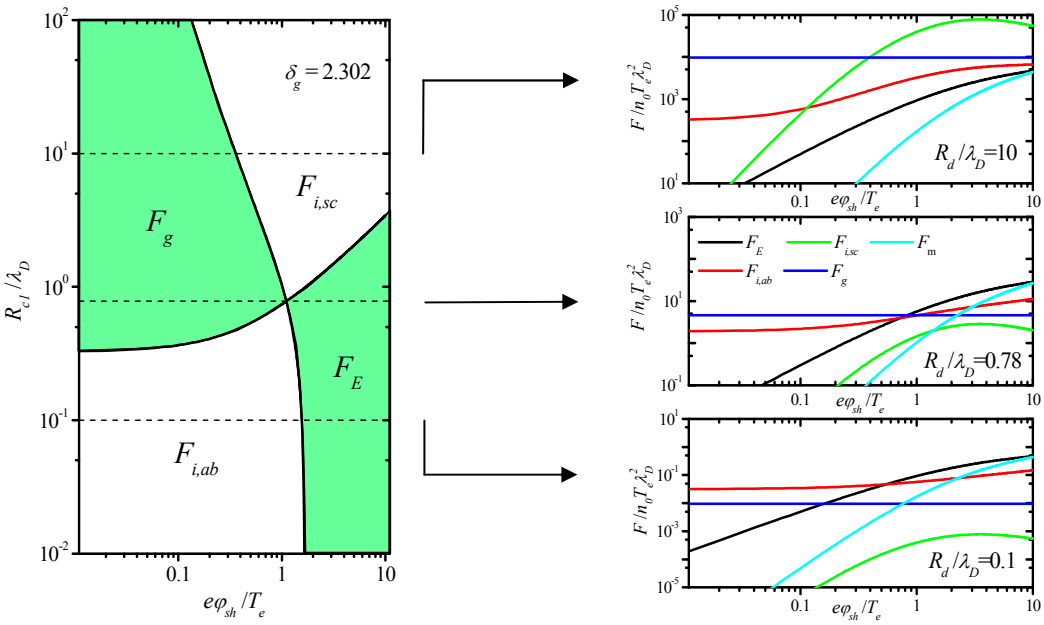

Fig. 2.2.8 *Force diagram for selected dust particle radii for the case of the gravitational force directed from the wall and the parameters* $\ln\Lambda_d = 3$, $\xi_q = 6.58$, *and* $\ln\Lambda_d = 3$.

region and the ion scattering drag force prevails in the upper pinned region. For the small dust particle $R_d/\lambda_D = 0.1$ the ion absorption drag force is dominant in the lower pinned region and the electrostatic force in the released region. The configuration of the pinned and released particles regions depend on the gravitational parameter. The diagram shown in Fig.2.2.9 displays the number of the first critical radius solutions depending on the sheath potential drop and the gravitational parameter. We can see that only one solution exists for the sheath potentials higher than the threshold potential that corresponds to the electrostatically released dust particles region. For the lower potentials than the threshold the two critical radius solutions exist when the gravitational parameter is above the solid line, which is defined by the condition $D = 0$. These two solutions bound the gravitationally released dust particles region. The area below the solid line in Fig.2.2.9 corresponds to the situation when all dust particles are pinned. The largest value of the gravitational parameter, when this situation is possible, is $\delta_g \approx 2.302$ and corresponding pinned and released dust particles regions are shown in Fig.2.2.8. Therefore, basing on the gravitational parameter and Fig.2.2.9 we can say what

configuration of the released and pinned dust particles regions we have, and using the first critical radius solutions we are able to predict particles of what size can leave the wall or not.

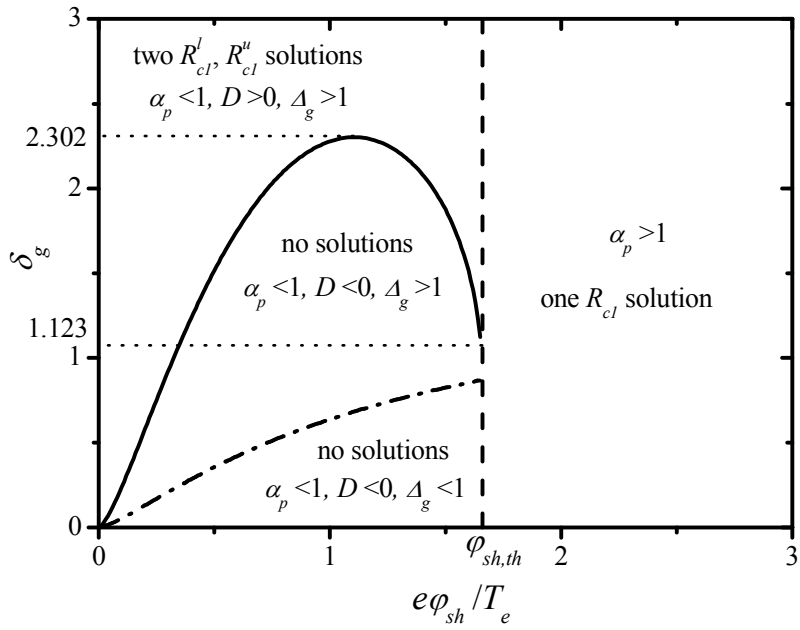

Fig. 2.2.9 *Diagram of the existence of the first critical dust radius depending on the sheath potential drop and the gravitational parameter for the case of the gravitational force directed from the wall. As everywhere above* $\xi_q = 6.58$ *and* $\ln \Lambda_d = 3$.

Therefore, in this section we have shown that the first critical dust radius exists, which discriminates the released and pinned dust particles on their radii. The dependences of the first critical dust radius on the sheath potential drop, the gravitational parameter and the dust form factor are analyzed. They show the possibility to control the size of the released dust particles with the externally applied bias voltage to the wall or even suppress the motion of dust particles with any size. The dependences of the first critical radius on the sheath potential were analyzed for different situations including the direction of the gravitational force, the dust mass densities and the plasma conditions. In the next section we show the dynamics of the released particles in the boundary plasma [67].

2.2.3 Dynamics in boundary plasma: the second critical radius

In this section we consider the motion of the dust particles in the boundary plasma, which are released from wall. The dynamics of the dust particle, which radius is smaller than the first critical radius, is described by the charging and motion equations

$$\begin{cases} \dfrac{d\,Q_d\left(z,t\right)}{d\,t} = I_i\left(z,t\right) - I_e\left(z,t\right) \\ m_d\,\dfrac{d^2 z}{d\,t^2} = F\left(z,t\right) \end{cases}, \tag{2.2.40}$$

where $F(z,t)$ is the total force acting on the particle at the current position and the time moment. The initial conditions for these equations assume that the dust particle is placed on the wall with zero velocity and its charge is conditioned by the attachment to the wall

$$z\left(t=0\right)=0\,,\quad \left.\frac{dz}{dt}\right|_{t=0}=0\,,\quad Q_d\left(t=0\right)=-\xi_q\,\pi\,R_d^2\,\varepsilon_0 E_w\,. \tag{2.2.41}$$

The ion and electron currents to the dust particle are described according to the OML theory [41,42] by the formulae (2.2.2-3) for the monoenergetic ions and the electrons with the Maxwellian velocity distribution and for both the negative and positive dust charge. The forces acting on the dust particle including the electrostatic force, the ion drag absorption and scattering forces are taken according to the previously described formulae (2.2.8-10). In this case, we omitted the electrostatic image force due to exponential screening of the dust potential by a plasma when the dust particle is detached from the wall. The gravitational force is constant because it does not depend on dust particle's position and charge. Therefore its effect will be discussed separately from the numerical solutions of the dust dynamics equations (2.2.40) in a non-uniform boundary plasma for better understanding of each force effect.

The spatial distributions of the plasma parameters in the sheath and the presheath were simulated and described in Section 2.1.3. The simulated spatial distributions of the electric potential, the electron and ion charge densities, the flow velocities and the temperatures are used to calculate the local currents and forces to the dust particle. The system of dust dynamics equations (2.2.40) together with the initial conditions (2.2.41) was solved numerically by the Runge-Kutta fourth order method for various dust particle radii and masses. The plasma parameters known at

the discrete positions of the PIC spatial computational mesh were linearly interpolated to the current dust particle's position. In Fig.2.2.10, the simulated trajectories, velocities and charges for the carbon $\rho_d = 2$ g/cm^3 dust particles of various radii are shown in the sheath and the presheath near the floating wall in the previously simulated system (Section 2.1.3) with the density of the hydrogen plasma at the bulk plasma boundary $n_0 = 10^{12}$ cm^{-3} and the electron and ion temperatures of the bulk plasma $T_e = T_i = 10$ eV. The particle positions in Fig.2.2.10 are normalized by the electron Debye length λ_D, which is 23.5 μm for the given plasma parameters, the velocities are normalized by the ion sound speed $c_{s0} = 3.09 \times 10^4$ m/s and the time is normalized by the ion plasma frequency $\omega_{i0} = 1.32 \times 10^9$ s^{-1}. As we can see from Fig.2.2.10(a), the smallest particles of $R_d = 2.35$ nm goes out of the simulated region in short time of a few microseconds and gain the speed up to 10^3 m/s. Somewhat bigger particle with $R_d = 0.235$ μm (Fig.2.2.10(b)) damping oscillations with a relatively large amplitude around some equilibrium position. As we do not take into account the dust-neutrals friction, the damping of the oscillations has collisionless nature and is caused by the delayed charging effect. The amplitude of the oscillations significantly exceeds the sheath width, which has the order of the Debye length, so the dust particle penetrates deeply into the presheath during the oscillations. The oscillation period of this dust particle is about 0.1 ms and it gains the velocity up to 10 m/s. The big particle with the radius $R_d = 9.4\,\mu$m also oscillates (Fig.2.2.10(c)), but the amplitude of the oscillations is comparatively small, so that the dust particle does not leave the sheath, the period of oscillations is about 3.8 ms, while the gained speed has the order of 1m/s. The charging time for the dust particles can be estimated according to formula (2.2.7), which shows that it is inversely proportional to the dust radius and gives $\tau_{ch}\,\omega_{i0} \approx 0.28$ for the particle with $R_d = 9.4\,\mu$m, $\tau_{ch}\,\omega_{i0} \approx 11$ for the $R_d = 0.235$ μm and $\tau_{ch}\,\omega_{i0} \approx 1.1 \times 10^3$ for the particle with $R_d = 2.35$ nm. These estimations are made for the simulated plasma parameter at the sheath edge, where the simulated electron density is $n_{e,sh} = 5.1 \times 10^{11}$ cm^{-3}, the ion density is $n_{i,sh} = 5.3 \times 10^{11}$ cm^{-3}, the ion flow velocity is $u_{i,sh} = 3.96 \times 10^4$ m/s and the effective electron temperature is $T_{e,sh} = 9.4$ eV.

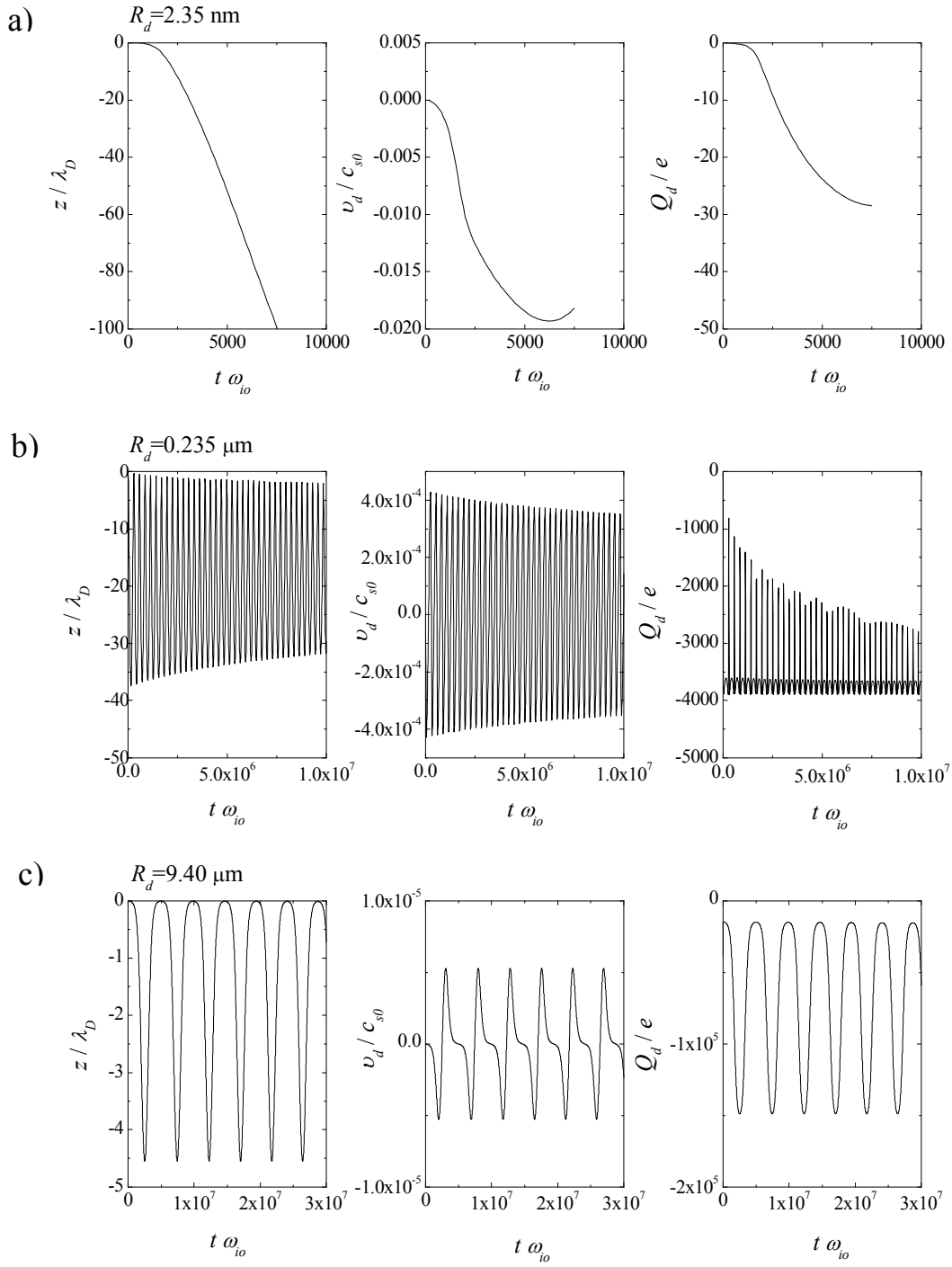

Fig. 2.2.10 *Time evolution of simulated trajectories and charge of the carbon dust particles ($\rho_d = 2$ g/cm^3) with various radii in the simulated boundary plasma.*

As we can see in Fig.2.2.10, the charging time is much shorter than the oscillation periods of the particles, except for the smallest one of the radius $R_d = 2.35$ nm. Therefore, the delayed charging effect, when the motion of a dust particle is fast and its local charge does not reach the local equilibrium value at any point, is strong for the smallest dust particle and weak for the large ones. The charging time of a dust particle (2.2.7) depends on the local plasma parameters, which vary in the sheath sharply. In Fig.2.2.11, spatial profiles of the charging time of the dust particles with the same radii as in Fig.2.2.10 are shown. As we can see, the charging time increases significantly in the Debye sheath, where the plasma density is low. That can enhance the delayed charging effect for the dust particles with the amplitude of oscillations within the sheath region. As we mentioned, the delayed charging is responsible for the damping of the dust particles oscillations. This damping occurs when even short delay in the dust charging accumulates during many oscillation periods. As was shown in [63], when there is a spatial gradient of the equilibrium dust charge then during the dust particle motion toward the gradient direction its charge will be a bit lower than the local equilibrium value and a bit higher during the motion in the opposite direction.

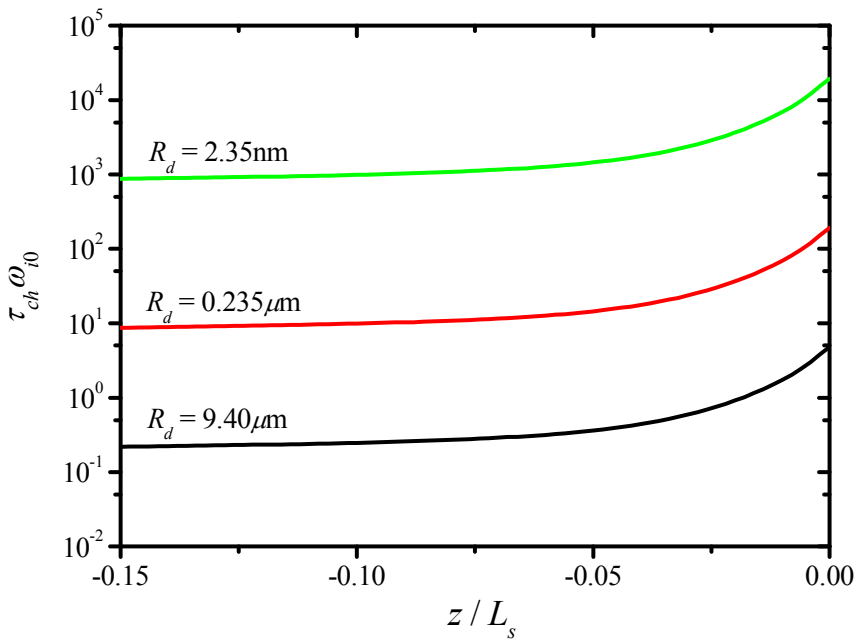

Fig. 2.2.11 *Spatial profiles of the charging time of the dust particles with different radii in the simulated boundary plasma.*

Thus, in any case the electric force acting on the dust particle will be a bit stronger during its motion in the opposite to the direction of the equilibrium dust charge gradient. This effect leads to the exciting or damping of the dust oscillations depending on the direction of the electric force. The shorter the charging time is, the smaller the delayed charging effect is, as we can see comparing between Fig.2.2.10(b) and Fig.2.2.10(c).

After this qualitative observation of the different dust particles trajectories, let's get closer look at the oscillations. In Fig.2.2.12, the amplitudes of the first oscillation period of the dust particle as functions of its radius are shown for various dust masses. One can see that there is no motion of dust particles of any masses, which radii are bigger than the first critical dust radius R_{c1}. Otherwise, the dust particle can leave the wall and penetrate into the plasma on a maximal distance $-z_{\max}$. As can be seen in Fig.2.2.12, there are dust particles, which can and can't go far from the wall, sharply discriminated on the dust radii by some value. We call this value the second critical dust radius R_{c2}. So, the smaller dust particles than the second critical dust radius have the large amplitude of oscillations in the boundary plasma, while the larger ones will oscillate with the small amplitude or stay near the wall depending on the initial conditions. More detailed analysis of the small amplitude oscillations requires taking into account the molecular interaction between the dust and the wall that is beyond of the present consideration. Thus, not all particles that are smaller than the first critical radius R_{c1} can actually penetrate into the plasma, and only that dust particles, which are smaller than the second critical radius, can do.

As can be seen in Fig.2.2.12, the radii of light dust particles, which are lighter than the critical mass $m_d < m_c$, cannot be strictly differentiated in respect to dust particles trajectories. Thus, there is no second critical radius for them. The second critical dust radius depends on the dust particle mass, as can be seen in Fig.2.2.12, and approaches the value $R_{c2}^{*} = 0.41\lambda_D$ for these plasma parameters when the dust mass approaches to infinity $m_d \to \infty$. The mass dependence can be explained by the delayed charging effect, which leads to increasing of the second critical radius with decreasing of the dust mass due to the faster dust motion from the wall compared to the slow relaxation of the high initial dust charge. For the very light dust particles with $m_d < m_c$, this effect is so strong that the electric field in the sheath region propels

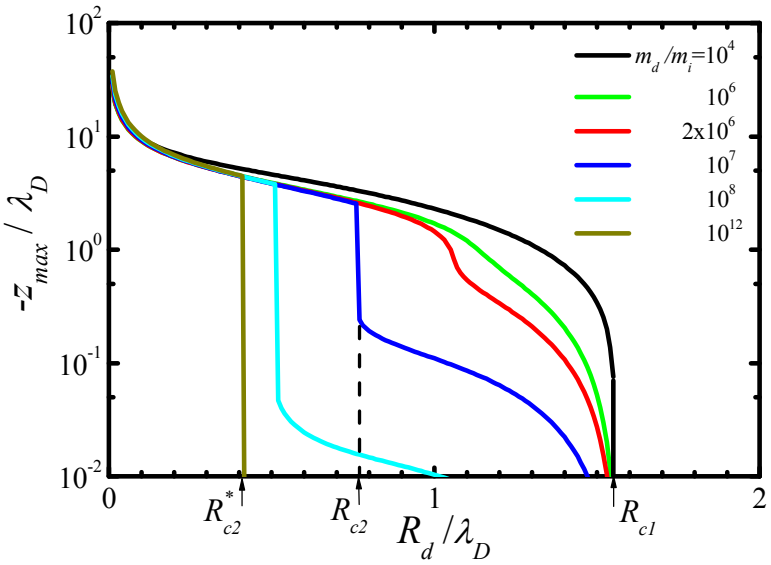

Fig. 2.2.12 *Amplitude of the first period of the dust particle oscillations as a function of the dust radius for different masses.*

them against the ion flux for any dust radii that smaller than the first critical one. From the simulations we found that the critical mass for the simulated plasma parameters equals approximately $m_c = 2\times10^6 m_i$, where m_i is the ion (proton) mass. For the solid carbon dust particles with $\rho_d = 2$ g/cm^3 we can find the relation $m_d / m_i = 5\cdot10^{12} R_d^3 [\mu\text{m}]$. Therefore, for these plasma parameters, the particles with the radii smaller than 7.4 nm are lighter than the critical mass and experience strong delayed charging effect. This estimation also agrees with the charging time calculations made for the dust particle, which trajectory is shown in Fig.2.2.10(a).

The existence of such sharp separation of the oscillation amplitudes on the dust radii for heavy dust particles can be explained using the effective potential energy

$$U(z) \equiv -\int_0^z F(z')\,dz'. \tag{2.2.42}$$

The effective potential energy is convenient for the analysis of the motion of the heavy dust particles as their charge is the local equilibrium one at any point due to the long enough oscillation periods in comparison with the dust charging time. Therefore, the total force acting on the heavy dust particles depends only on the local plasma parameters and the local equilibrium dust charge, but not on the time, thus we can use the effective potential. As we saw above, this is an approximate assumption

for many oscillation periods, but is good for the one period and becomes more precise for heavier dust particles. The spatial profiles of the effective potential are shown in Fig.2.2.13 for different radii of the dust particles. For the dust particles smaller than the second critical radius $R_{c2}^{*} = 0.41\lambda_D$, the gradient of the effective energy near the wall is positive (Fig.2.2.13(a)), so the total force is directed from the wall, and there is a potential minimum, around which a dust particle oscillates reaching far from the wall positions (Fig.2.2.13(b)).

The bigger dust particles than R_{c2}^{*} have no minimum of the potential energy or the effective potential barrier does not allow them to move far from the wall. Such dust particles return to the wall, where they recharge, and detach from the wall again. Therefore, the heavy dust particles are capable to move away from the wall on a significant distance only if their radii are smaller than R_{c2}^{*}. The smaller the dust particle is, the deeper it penetrates into the plasma. Note also that the returning point of a dust particle trajectory is located much further from the wall than its equilibrium position, especially for small particles. Such small particles can reach the bulk plasma, see also Fig.2.2.10(a).

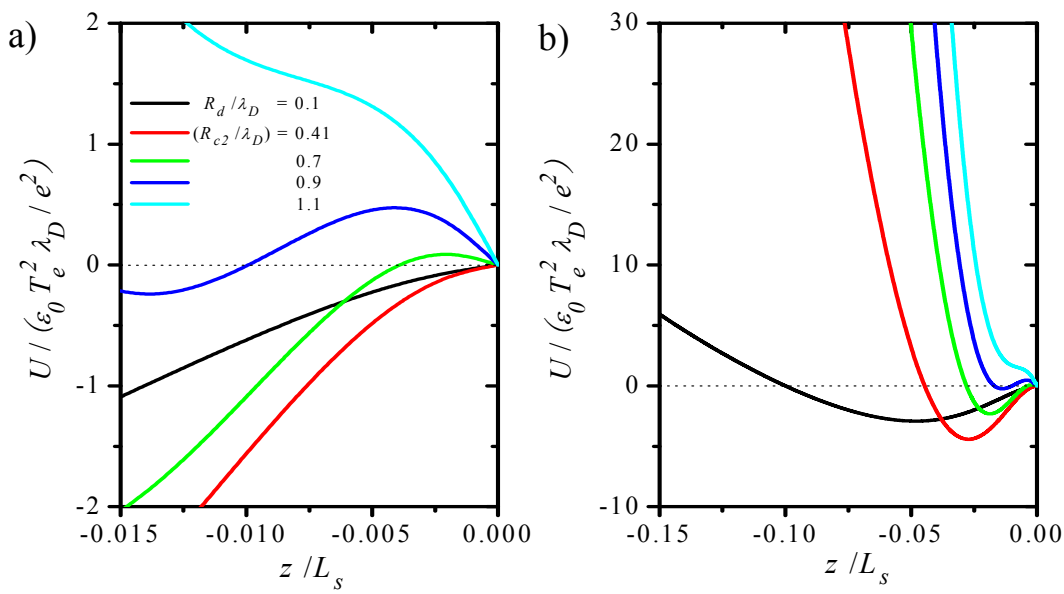

Fig. 2.2.13 *Spatial profiles of the effective potential energy for heavy dust particles with different radii on close to the wall spatial scale (a) and the extended scale (b).*

The minima and the maxima of the effective potential energy correspond to the stable and unstable equilibrium positions of the dust particle, respectively. For understanding when and why the effective potential barrier appears, we obtained the equilibrium positions for dust particles of various radii. If a dust particle with the given radius R_d is placed at some position in the plasma for sufficiently long time, it obtains the local equilibrium charge $Q_{d,eq}(z)$, which corresponds to the zero total current on the dust particle $dQ_{d,eq}(z)/dt = 0$. If the local equilibrium charge of the dust particle at some position corresponds to the zero total force acting on it, then this position is equilibrium position z_{eq} of the dust particle of the radius R_d, so that $d^2 z_{eq}/dt^2 = 0$. Fig.2.2.14 presents the calculated equilibrium positions and the corresponding equilibrium charges for the dust particles with the radius R_d. As we can see, there is no equilibrium positions for the dust particles with the larger radius than R_{c2}^{cut}, which is the critical levitation radius found in [60]. That situation corresponds to monotonically decreasing effective potential profiles in Fig.2.2.13.

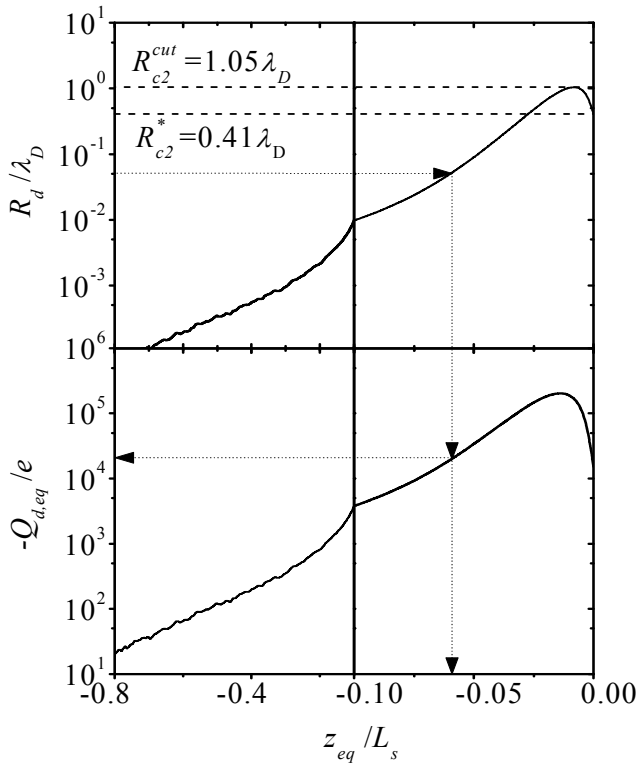

Fig. 2.2.14 *Equilibrium dust position and the corresponding local equilibrium dust charge as function of the dust particle radius.*

There are two equilibrium positions for the dust with the radii $R_{c2}^{cut} > R_d > R_{c2}^*$. The equilibrium position closer to the wall is unstable that corresponds to the effective potential maxima, while the one further from the wall is the stable equilibrium position, which corresponds to the effective potential minima (Fig.2.2.13). There is only one stable equilibrium position far from the wall when $R_d < R_{c2}^*$. Therefore, the value R_{c2}^* corresponds to the effective potential barrier, which just appears near the wall. Here, we classify the motions of heavy dust particles started from the wall on their radii without the gravitational force:

$R_{c1} > R_d > R_{c2}^{cut}$ - There is no equilibrium position. The particle returns to the plate just after detachment from it. The particle can perform short oscillations in the immediate proximity to the wall due to the recharging process when its initial velocity is not zero.

$R_{c2}^{cut} > R_d > R_{c2}^*$ - The dust particle initially placed at the wall cannot reach its equilibrium position due to existence of the effective potential barrier and returns to the plate similar to the previous case. However, if the initial kinetic energy of the dust particle is larger than this barrier, it can oscillate around its equilibrium position.

$R_{c2}^* > R_d$ - There is only one stable equilibrium position. The smaller the dust particle is, the further from the wall the equilibrium position. The particle will oscillate around its equilibrium position.

Now it can be clearly seen, that the effective potential barrier is the reason of the sharp separation between the short and long amplitude oscillations, and the radius R_{c2}^*, when the barrier appears, is the second critical radius for the heavy dust particles described above. The physical explanation of the non-monotonous effective potential profiles with the maxima is based on the spatial profile of the local equilibrium dust charge. As can be seen in Fig.2.2.15, the sharp decrease of the charge near the wall makes the electric force acting on the dust particle weak in spite of the strong electric field there. Actually, when the wall potential is deeply negative, the electron density near the wall will be very low and a dust particle can have a positive electric charge there, so the electric force will be directed toward the wall and there will be no repulsive force at all. That occurs for the dust particles of any radius, because, as can be seen from the electron and ion charging currents (2.2.2-3) and Fig.2.2.15, the equilibrium dust charge is proportional to the radius.

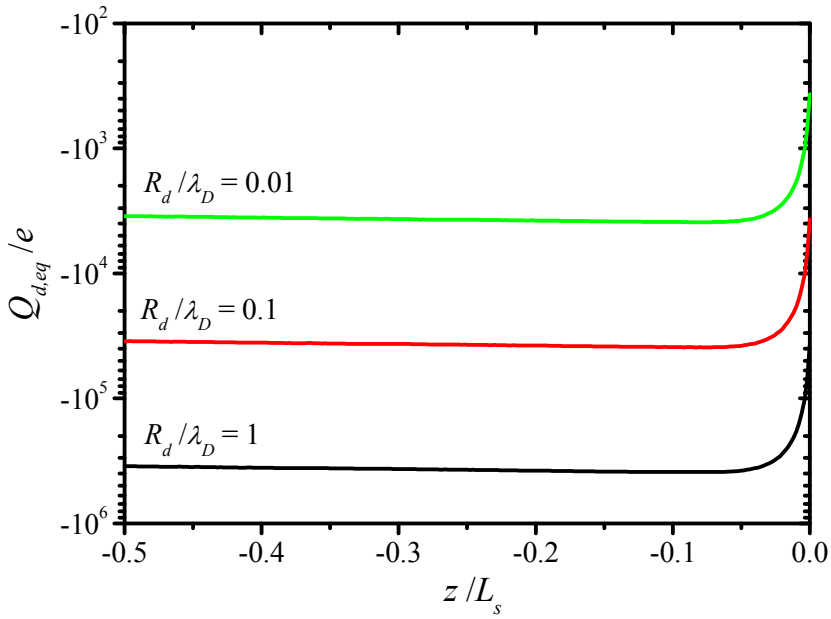

Fig. 2.2.15 *Spatial profiles of the local equilibrium charge of the dust particles with different radii in the simulated system.*

In order to analyze the dependence of the second critical radius on the wall potential, let's use the Bohm sheath model [21,24], which was used for the analysis of the first critical radius and which gives the same local plasma parameters as analytical functions of the local potential $\varphi(z)$ as (2.2.29-31). The potential inside the sheath has all values from zero at the sheath edge to the arbitrary wall potential, which equals to the sheath potential drop φ_{sh}. In Fig.2.2.16, the radius of the dust particle that has the equilibrium position at the point with the potential $\varphi(z)$ is shown. As we can see from Fig.2.2.16, when the wall potential is deeper than $-4.23T_e/e$ and the particles smaller than $1.17\lambda_D$, two equilibrium positions exist. The equilibrium position closer to the wall is unstable and another is stable. Hence, the decreasing part of the curve corresponds to the second critical radius, while the increasing part corresponds to the positions of the effective potential minima. Thus, if the wall potential is shallower than $-2.84T_e/e$, then there is no maximum of the effective potential in the system and so the second critical radius does not appear. If the wall potential is deeper than $-4.23T_e/e$, then a maximum appears for the dust particles with $R_d < 1.17\lambda_D$. In this

case dust particles of any size with low kinetic energy can be confined in the vicinity of the wall. Therefore, the second critical dust radius exists only for the sheath potential drops in the range $2.84 < e\varphi_{sh}/T_e < 4.23$.

The effect of gravity on the effective potential energy maxima and minima positions and the second critical radius is similar to its effect on the first critical radius. In Fig.2.2.17, the dependencies of the first critical radius on the sheath potential drop together with the radius of the dust particle, which has the equilibrium at the point with the potential φ, for the different directions of the gravitational force are shown. The used value of the gravitational parameter in Fig.2.2.17 is large enough $\delta_g = 1.66 \times 10^4$ in order to demonstrate the gravity effect clearly. When the gravitational force is directed toward the wall the second critical dust radius decreases (Fig.2.2.17(c)) as could be expected. Note that the dust particles can go deep into the plasma only when the wall potential and the dust radii are in the intersection region of $R_d \le R_{c1}$ and $R_d \ge R_{c2}$. In the opposite case, the positions of the effective potential minima and maxima can be separated (Fig.2.2.17(a)).

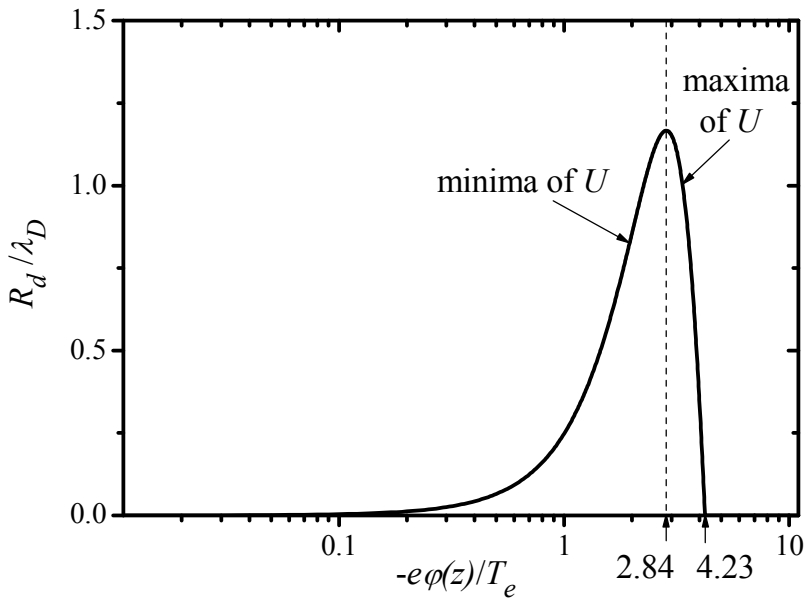

Fig. 2.2.16 *Radius of a dust particle, which has the equilibrium position at the point z as function of the local potential $\varphi(z)$ in the sheath described according to the Bohm sheath model* [21,24].

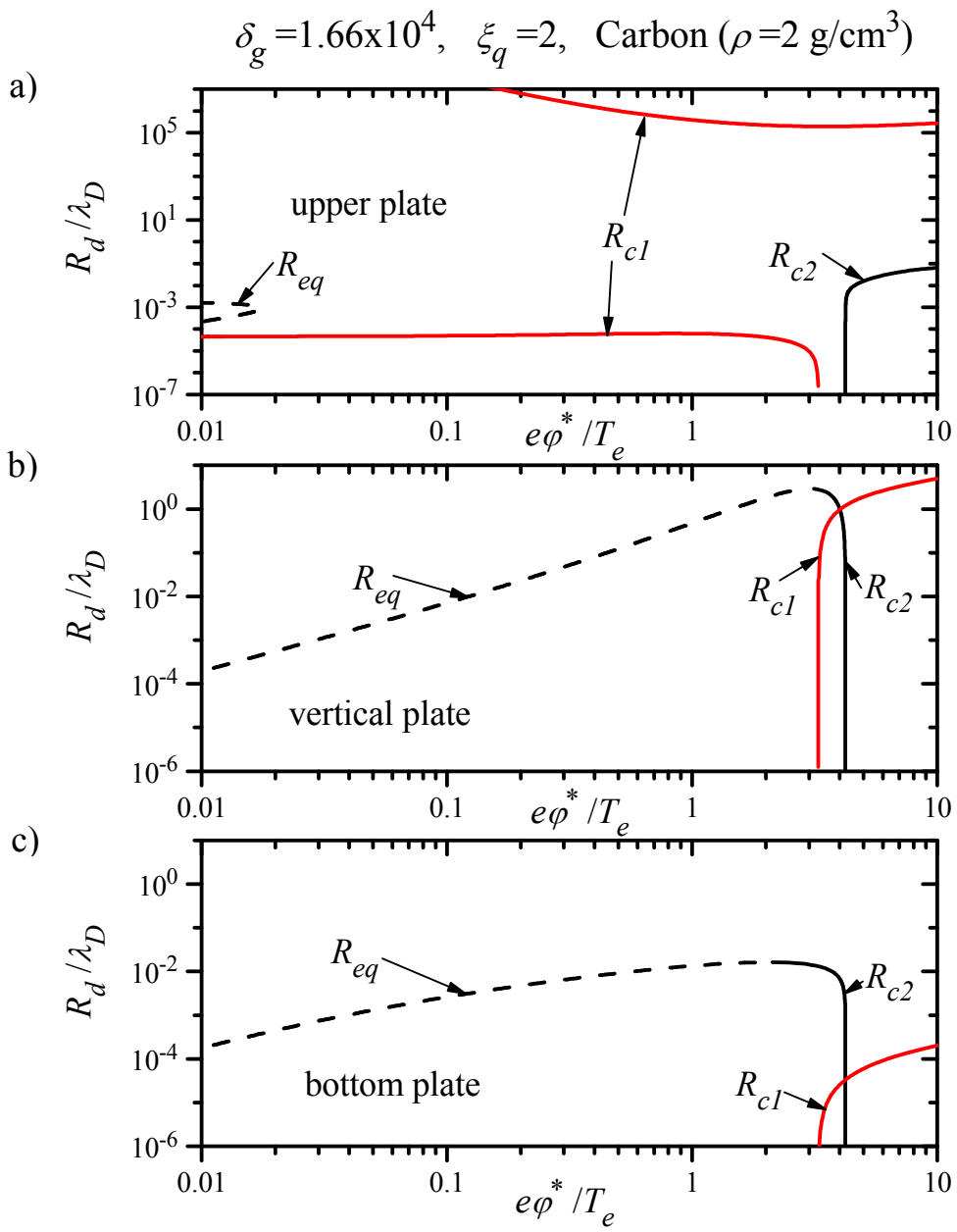

Fig. 2.2.17 *Dependencies of the first critical dust radius on the sheath potential drop* $\varphi_{sh} = \varphi^*$ *(red lines) and the radius of the dust particle, which has the equilibrium at the point with the potential* $\varphi = -\varphi^*$ *(black lines: solid for the unstable equilibrium and dashed lines for the stable one), for the gravitational force directed from the wall (a), to the wall (c) and without gravity (b).*

In this case, for some very small dust particles in the deep sheath potentials there is only an effective potential maximum, while some bigger particles have no barrier and fall down from the wall. Interesting is the region inside the R_{eq} curve, where the dust particles have stable equilibrium position. It means that the corresponding dust particles can possibly levitate or oscillate near the wall above them. Therefore, the diagrams, like shown in Fig.2.2.17, calculated for various values of the gravitational parameter δ_g and different form factors ξ_q give complete description of the dust particle behavior for any values of the dust radius R_d and the wall potential.

In this section we studied the dynamics of a dust particle coming off the wall in the sheath and the presheath using solutions of dust dynamics equations, i.e. the equations of motion and charging simultaneously, in wide range of the dust radii, masses and the wall potentials. It was shown that the second critical radius exists for heavy dust particles, $m_d > m_c$, which separates particles that can or can not go far from the wall. Dynamics of the dust particle charging during the motion causes dependence of the second critical radius on the dust mass and finally leads to its vanishing for $m_d < m_c$. The delayed charging effect also causes the collisionless damping of the oscillations. The smaller the dust particle is, the deeper it goes into the plasma. The existence of the second critical radius was explained by the appearance of the effective potential barrier due to sharp decreasing of the equilibrium dust charge near the wall. The combined dependencies of the first critical radius on the wall potential and the second critical radius on the local potential in the boundary plasma for different directions of the gravitational force allow to analyze the dust particle behavior in the wide range of the plasma parameters [68].

2.3 Dust behavior in edge plasma of fusion devices

In this section we discuss the dust dynamics in edge plasmas of fusion devices, which takes into account some important aspects not considered in the previous sections, e.g. a heat balance of the dust particles and an effect of a magnetic field presence. The results described here were published in [11]. In order to estimate conditions, under which a dust particle can survive in a plasma, we consider a balance of incoming and outgoing energy fluxes to/from a spherical dust particle. The major energy input is the absorption of ions and electrons by the dust particle from a surrounding plasma and their recombination on the dust surface. Another source of the incoming energy is bremsstrahlung and line radiation in a plasma that can be absorbed by the dust particle. Since the dust particle in a plasma usually obtains a negative floating potential, φ_d, which corresponds to equality of absorbed ion and electron fluxes, the energy gained by ions in the sheath potential drop equals to the energy lost by electrons. Therefore, we can calculate the electron, ion particle fluxes and their kinetic energy fluxes to the dust particle assuming the Maxwellian velocity distribution functions of electrons and ions in an unperturbed plasma. Neglecting effect of a magnetic field in the limit $\rho_{Le}, \rho_{Li} \gg \lambda_D$, where ρ_{Le} and ρ_{Li} are the electron and ion Larmor radii, respectively, and taking absorption cross section according to the Orbital Motion Limited (OML) theory [41,42] we can get absorbed particle fluxes

$$\Gamma_e = \pi R_d^2 n_0 \sqrt{\frac{8T_e}{\pi m_e}} \exp\left(\frac{e\varphi_d}{T_e}\right), \quad \Gamma_i = \pi R_d^2 n_0 \sqrt{\frac{8T_i}{\pi m_i}} \left(1 - \frac{e\varphi_d}{T_i}\right), \tag{2.3.1}$$

where R_d is the radius of the dust particle, T_e, T_i are the electron and ion temperatures, respectively, and n_0 is the electron or ion density under quasi-neutrality condition for the hydrogen plasma. Assuming $T_e = T_i = T$, $m_i / m_e = 1836$, and from the equal electron and ion fluxes we find the dust floating potential

$$\frac{e\varphi_d}{T} = -2.504 . \tag{2.3.2}$$

Similarly, we can obtain following expressions for the electron and ion kinetic energy fluxes to the dust particle

$$W_e = 2T_e \pi R_d^2 n_0 \sqrt{\frac{8T_e}{\pi m_e}} \left(1 - \frac{e\varphi_d}{2T_e}\right) \exp\left(\frac{e\varphi_d}{T_e}\right)$$
$$W_i = 2T_i \pi R_d^2 n_0 \sqrt{\frac{8T_i}{\pi m_i}} \left(1 - \frac{e\varphi_d}{2T_i}\right) . \qquad (2.3.3)$$

The sum of the energy fluxes to the dust particle due to the absorption of electrons and ions is $W_p = W_e + W_i + \Gamma_i \varepsilon_{iz}$, where ε_{iz} is the ionization potential of the neutral atoms. Here, it is assumed full absorption of the recombination energy by the dust particle. Taking into account the floating potential (2.3.2), we obtain

$$W_p = \pi R_d^2 n_0 \sqrt{\frac{8T}{\pi m_i}} \left(20.29T + 3.504\varepsilon_{iz}\right). \qquad (2.3.4)$$

Corresponding total heat transmission coefficient for the dust particle's sheath is

$$\gamma_d \equiv \left(W_e + W_i\right)/\Gamma_e = 5.79. \qquad (2.3.5)$$

Radiation heating of the dust particle we roughly estimate with some constant energy flux density P_{rad}, assuming that the dust particle is uniformly exposed to the radiation. Thus, the radiation energy flux to the dust particle equals

$$W_{rad} = 4\pi R_d^2 P_{rad}. \qquad (2.3.6)$$

The typical value of P_{rad} for present fusion devices can be estimated as $\sim 10^4$ W/m^2 that is usually negligible in comparison with the absorbed particle energy flux density. As we can see, both heating processes are defined by plasma parameters and are independent of the temperature of the dust particle T_d.

Different processes such as the radiation, the thermal evaporation, the physical and chemical sputtering, and the radiation enhanced sublimation (RES) can sustain cooling of the dust particle. We neglect effects of neutrals in a plasma taking into account their low density in comparison with the ion density.

The radiation energy flux from the dust particle can be described with the Stefan-Boltzmann function

$$W_{SB} = 4\pi R_d^2 \sigma_{SB} T_d^4, \qquad (2.3.7)$$

where $\sigma_{SB} = 5.67 \times 10^{-8}$ W/m^{2}K^4 is the Stefan-Boltzmann constant. Here, for simplicity the total emissivity of the dust particle taken equal unity thanks to usual surface roughness of dust particles, which were observed in fusion devices [5,6]. Evaporation cooling of the dust particle we estimate assuming that the particle

consists of carbon (graphite) and taking for it experimental data of the evaporation rate as a function of the dust temperature T_d, and the heat of vaporization from [78]. The evaporation rate $G_{C,evap}$ can be expressed as

$$G_{C,evap} = 4\pi R_d^2\, 5.01\times 10^{26}\, T_d^{-1/2}\, 10^{10.3656-38570/T_d} \text{ atom /s.} \tag{2.3.8}$$

The bound energy of a carbon atom calculated from the heat of vaporization is $\Delta\varepsilon_{evap} = 7.43$ eV. Therefore, the energy flux from the dust particle due to the thermal evaporation is written as

$$W_{evap} = G_{C,evap}\,\Delta\varepsilon_{evap}\,. \tag{2.3.9}$$

Other mechanisms of the dust cooling (physical and chemical sputtering and RES) are associated with the incoming ion flux Γ_i (2.3.1) to the dust particle. Each of these processes has the experimentally or numerically defined erosion yield Y that generally is function of ion energies ε_i and the dust temperature T_d. Assuming that above processes are caused by the proton flux on the carbon dust particle and taking corresponding yield dependencies from [73,74], we can calculate the averaged yield over the ion energy distribution function $f_i(\varepsilon_i)$:

$\bar{Y} = \Gamma_i^{-1}\sqrt{\dfrac{2}{m_i}}\int_0^\infty d\varepsilon_i\,\sigma_{ab}(\varepsilon_i)\,E_i^{1/2}\,Y(\varepsilon_i - e\varphi_d)\,f_i(\varepsilon_i)$, here $\sigma_{ab}(\varepsilon_i)$ is the absorption cross section of ions by the dust particle. For the Maxwellian ion energy distribution function with temperature the $T = 10$ eV, we obtain for physical sputtering and RES

$$\bar{Y}_{phys} \cong 1.4\times 10^{-4}, \quad \bar{Y}_{RES}(T_d) \cong 0.049\exp\left(-\frac{6932.6}{T_d}\right). \tag{2.3.10}$$

Total erosion yield for chemical sputtering $Y_{chem}(T_d)$ is taken from [74] for the ion energy range 20-30 eV. Activation energies for these processes can be estimated as

$$\Delta\varepsilon_{phys} = 7.4\,\text{eV}, \quad \Delta\varepsilon_{RES} \approx 0.7\,\text{eV}, \quad \Delta\varepsilon_{chem} \approx 2\,\text{eV}, \tag{2.3.11}$$

that finally gives the following energy fluxes carried out from the dust particle by three considered processes

$$W_{phys} = \Gamma_i \bar{Y}_{phys}\,\Delta\varepsilon_{phys}\,,\; W_{RES} = \Gamma_i \bar{Y}_{RES}\,\Delta\varepsilon_{RES}\,,\; W_{chem} = \Gamma_i Y_{chem}\,\Delta\varepsilon_{chem}\,. \tag{2.3.12}$$

The follow condition of the energy balance for the dust particle

$$W \equiv \left(W_p + W_{rad}\right) - \left(W_{SB} + W_{evap} + W_{phys} + W_{RES} + W_{chem}\right) = 0 \tag{2.3.13}$$

defines its equilibrium temperature $T_{d,eq}$. It should be noted, that all involved energy fluxes are proportional to the surface area of the dust particle $\sim R_d^2$, which is canceled in the equilibrium condition (2.3.13), so that the equilibrium temperature of the dust particle $T_{d,eq}$ doesn't depend on the dust radius.

The dependencies of the incoming and outgoing energy flux densities to the dust particle on its temperature are presented in Fig.2.3.1. Cross points of the total cooling and heating power curves give solutions of (2.3.13) and thus the dust equilibrium temperature $T_{d,eq}$ for different plasma densities. As can be seen in Fig.2.3.1, contributions of RES, physical and chemical sputtering in dust cooling around the equilibrium condition are negligible for the given plasma temperature. Depending on the plasma density, cooling of the dust particle at the thermal equilibrium carried out either by radiation or evaporation. In the last case corresponding to the high plasma densities and dust equilibrium temperatures, the dust particle can be destructed quickly.

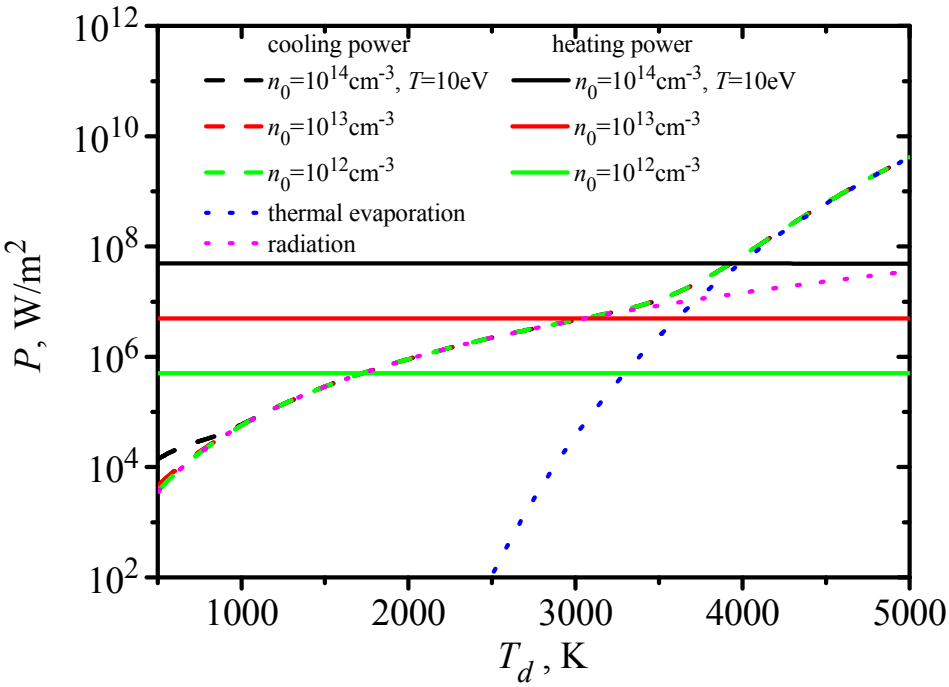

Fig. 2.3.1 *Incoming and outgoing energy flux densities for a spherical carbon dust particle in hydrogen plasma with* $T_e = T_i = 10\,\text{eV}$ *and various densities* n_0.

We can estimate the rate of dust destruction and its dwell time taking into account four processes mentioned above: thermal evaporation, RES, physical and chemical sputtering. These processes cause the flux of carbon from the dust particle that can be written as

$$G_C = G_{C,evap} + \Gamma_i \left(\overline{Y}_{phys} + \overline{Y}_{RES} + Y_{chem} \right). \tag{2.3.14}$$

Decreasing rate of the radius of the spherical dust particle is

$$\frac{dR_d}{dt} = \frac{A_C G_C}{4\pi R_d^2 \rho_d N_A}, \tag{2.3.15}$$

where $A_C = 12$ g/mole is the carbon's atomic weight, $\rho_d \approx 2$ g/cm^3 is the dust particle mass density, and N_A is the Avogadro's constant. As the flux G_C is again proportional to the dust surface area, the dust radius decreasing rate (2.3.15) is not a function of the radius.

Fig.2.3.2 presents the dust temperature dependencies of the calculated decreasing rates of the dust particle radius for the same plasma parameters as in Fig.2.3.1. In the range of lower dust temperatures than $\sim 1000K$ the dust destruction is caused by chemical processes, at dust temperatures higher than $\sim 3000K$ the fast thermal evaporation of the dust started. There is the slowest destruction rate in the intermediate temperature range caused by RES. Taking the dust equilibrium temperatures from Fig.2.3.1 we find from Fig.2.3.2(b) that the dust particle dwell time strongly depends on the plasma density. The typical dust particle of micrometer size can survive in a plasma ~ 10 s for $n_0 = 10^{13}$ cm^{-3} and $\sim 10^{-2}$ s for $n = 10^{14}$ cm^{-3}. In the last case, there is the reasonable question about the dust heating time, whether the dust particle will survive long enough to get the equilibrium temperature. Simple estimation gives the dust heating time

$$\tau_{heat} = \frac{\rho_d R_d}{3A_C} \int_{T_0}^{T_{d,eq}} \frac{C_{mh}}{W} dT_d, \tag{2.3.16}$$

where C_{mh} is the carbon's molar heat capacity [78]. Calculating the heating time (2.3.16) for the dust particle with $R_d = 1\,\mu$m in the plasma with $n_0 = 10^{14}$ cm^{-3}, we can find $\tau_{heat} \sim 10^{-4}$ s that is much shorter than the dwell time. Above estimations show that in a divertor plasma of present fusion devices dust particles can survive long time > 10 s and with high speed can be transported through the more dense edge plasma.

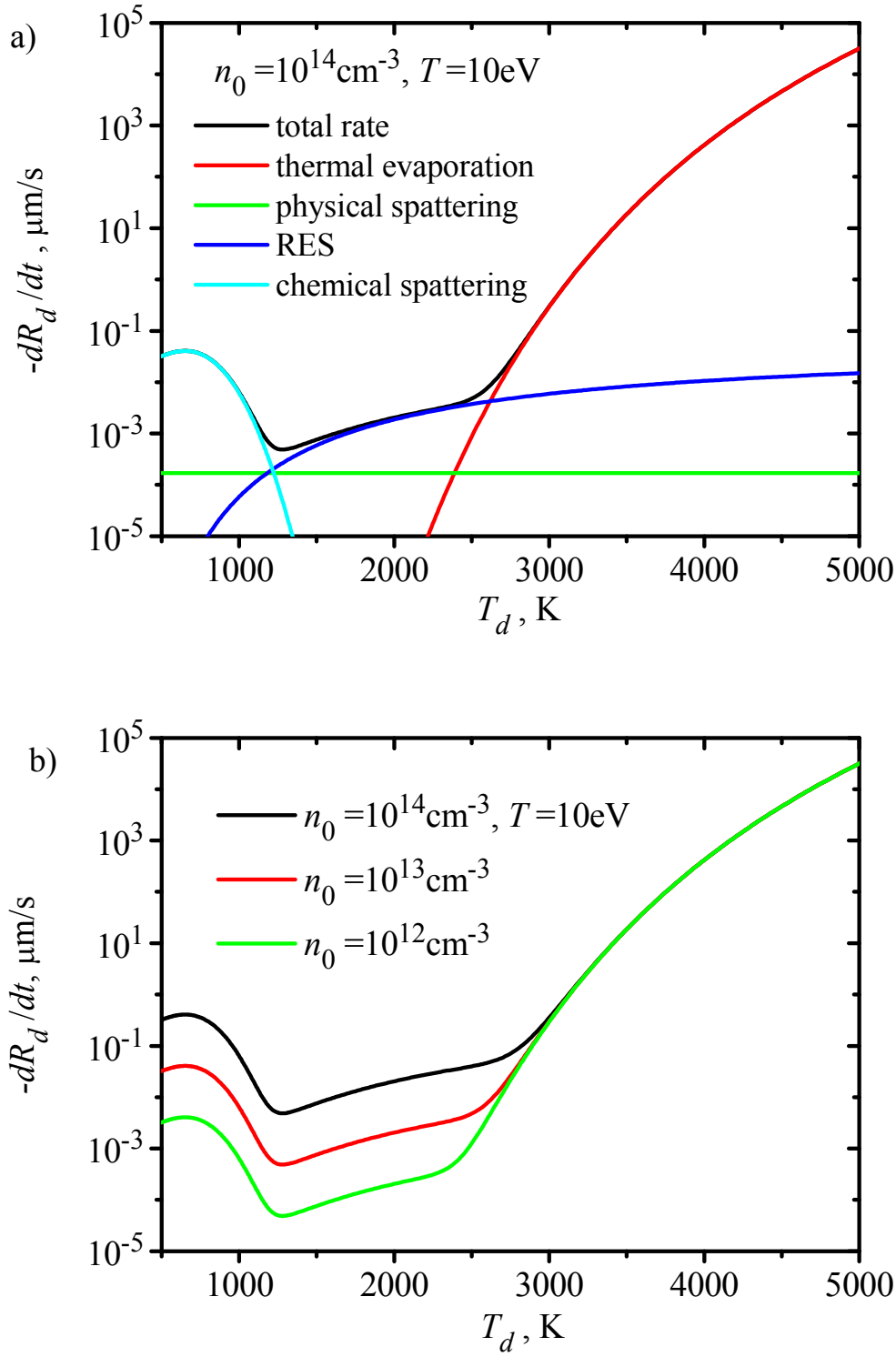

Fig. 2.3.2 *Rates of a spherical carbon dust particle radius decreasing due to various processes (a) in the hydrogen plasma with* $T_e = T_i = 10$ eV *and various densities* n_0 *(b).*

The dynamics of the dust particle in a magnetized sheath were considered in [11] for the magnetic field oblique to the wall with not too small angle α_B, $1 >> \alpha_B > \sqrt{m_e/m_i}$. As well known [26] the magnetized sheath consists of two regions: the quasi-neutral magnetic presheath with the scale length of the order of the ion gyro-radius ρ_{Li}, and the Debye sheath with the scale length of the order of the Debye length λ_D, it is assumed here that $\lambda_D < \rho_{Li}$. At the entrance of the presheath, ions move along the magnetic field toward the wall. The component of ion velocity normal to the wall starts to increase when they are closer to the wall than the ion gyro-radius due to scraping wall ion trajectories during gyro-motion. There are also strong diamagnetic and $E \times B$ ion flows along the direction parallel to the wall and perpendicular to the magnetic field in the magnetized sheath. The motion of a dust particle itself is not magnetized as the Larmor radius for the dust particle is very large due to the huge dust mass, but the direction of the ion drag force depends on the direction of the magnetized ion flow. As the ion drag force provided by the diamagnetic ion flow is not balanced by any other force, the dust particle can be significantly accelerated in parallel to the wall direction. Due to this acceleration the dust particle can obtain as large as a few km/s velocity parallel to the wall. Therefore, if the wall has steps or roughness (like edge of a limiter or a divertor plate or inhomogeneous redeposited layers) the dust particle can be launched into the plasma in poloidal or radial direction (limiter case) and fly on significant distances. The obtained high velocity allows reflection of the dust particles from other walls that makes motion of the dust particles in a complex geometry of fusion devices rather difficult to predict. The combination of the dust particles oscillations in the direction normal to the wall and motion parallel to the wall can produce “jumping” of the dust particle on the wall surface. In the case, when the surface is not smooth the “jumping” may be enhanced by the diamagnetic ion flow, which is parallel to the wall surface locally, but the obtained acceleration may be not parallel to the wall at the next “jump” position. All these types of the dust particles motion may make their way toward the hot and dense core plasma, where the dust particles are destroyed and deliver their components as impurities.

2.4 Conclusion

In this chapter we have analyzed the behavior of a spherical dust particle in a boundary plasma near an electrically biased wall using the one-dimensional (1D) approach. The plasma parameters in the sheath and the presheath are obtained in the 1D model and then the motion of a spherical dust particle is analyzed along the normal direction to the wall. The currents and the forces to the dust particle are calculated as if the spherical (three dimensional) dust particle was immersed into the plasma, which is non-uniform only in normal direction to the wall (one-dimensional). The dynamics of the dust particle is calculated by solving the dust charging and motion equations separately from the plasma simulations. Such separation is caused by the huge difference between timescales of the plasma and dust dynamics. In this model, it is also assumed that the dust particle does not disturb a plasma significantly and we can use the simulated local plasma parameters for the calculation of the currents and forces. Using this approach we have studied the conditions, under which the dust particles can be released from the wall, and the possible trajectories of the dust particles of various radii and masses in the sheath. We showed that there is the first critical dust radius, which defines the biggest dust particles capable to leave the wall due to excess of the electrostatic force over the ion drag forces acting on the particle. The dependence of the first critical radius on the wall potential allows controlling the size of the released dust particles with applying of a bias voltage to the wall. It was shown that there is the critical wall potential relative to the plasma potential, when the releasing of any size dust particles from the wall is suppressed. The gravity effect on the first critical radius is clarified. As was shown, the gravitational force directed to the wall reasonably reduces the value of the first critical radius. On the other hand, when the gravitational force directed from the wall, the releasing of the dust particles from the wall becomes possible below the critical wall potential. However, not all released dust particles can further move deeply into the plasma. Some dust particles can oscillate in the sheath with large amplitude, while others can not go far from the wall and return on it due to the recharging process. The existence of the second critical dust radius, which separates the oscillating and returning dust particles on their radii, was shown in the certain range of the wall potentials. The appearance of the second critical radius is explained by peculiarities of

the equilibrium dust charge and the effective potential profiles. The effect of the delayed dust charging is pointed out, that leads to damping of the dust particles oscillations and disappearance of the second critical radius for the very light particles. The combined diagrams of the critical radii and the wall potentials for different gravity conditions show all possible types of the dust particle behavior in the analyzed system. We suggest that the modern experimental techniques allow verifying these results under laboratory plasma conditions in relatively straightforward way using spherical dust particles of different radii in DC discharge plasma. For that purpose distributions of dust particles on their radii on an electrode can be compared before and after exposure to a plasma or, possibly, direct observation of an individual dust particle motion can be used. However, the small amplitude dust oscillations, when a dust particle just detaches the wall, may be difficult to detect.

Some aspects of a dust particle dynamics in edge plasmas of fusion devices were discussed. We have analyzed the power balance of the dust particles due to various heating and cooling mechanisms for different densities of plasmas. We have shown the dependences of the heating and cooling powers on the dust temperature that gives us the equilibrium dust temperature under various plasma conditions. The rate of dust destruction was obtained as a function of the dust particle temperature. It shows that a dust particle of a micrometer size can survive sufficiently long time (tens of seconds) in edge plasmas. The effect of a magnetic field on dust dynamics is discussed and the possibility of acceleration of the dust particles along the wall surface due to diamagnetic drift of ions was shown. It is suggested that the dust particles can be an important source of the impurities in future fusion reactors like ITER [12], where the heat flux on a divertor plate and its destruction is expected as significant. The more detailed studies of the dust particles motion in a magnetized edge plasma should be done using integrated simulations of the total SOL plasma (fluid or kinetic approaches) and dust dynamics (e.g. by Monte-Carlo method), that requires combination and developing of different codes. To describe the properties (charging, forces) of a dust particle in plasma under various conditions including a magnetic field more detailed theoretical and simulation studies are also needed.

Chapter 3

Dust behavior in boundary plasma – Two-dimensional model

In this chapter we consider the properties of a spherical conductive dust particle on a plasma-facing wall and sheath formation with the dust particle using the self-consistent two-dimensional Particle-In-Cell (2D PIC) simulations. The simulations are conducted to overcome the limitations of the one-dimensional model used in Chapter 2, where the dust particle was assumed not affecting the sheath formation. The PIC method allows kinetic self-consistent simulations of sheaths with the dust particle of various shape and size that can be larger than a Debye length or even a sheath width and can strongly affect the sheath formation. In this chapter we describe the developed simulation method and analyze the simulated charge, currents and forces to the dust particle at the wall position in comparison with the analytical approach. The present state of this study shows at which points the theoretical consideration of the dust statics on the plasma-facing wall agrees or disagrees with the simulation results and what are important effects that should be included in the theoretical description, besides some preliminary modifications are proposed. The further modifications of the analytical approach as well as the self-consistent simulation study of the dust particles with various shapes apart from the wall are the future issues of this study.

3.1 Introduction

In the previous consideration of the dust particles behavior on a plasma-facing wall and in the boundary plasma we neglected the effect of the dust on the plasma as was described above. Such simplification was necessary to solve analytically dust statics equations on the plasma-facing wall and obtain expressions for dependencies

of the critical dust radii on local plasma parameters and the wall potential. However, the kinetic approach is necessary to describe the self-consistent interaction of the dust particle with the plasma as the dust charging and shielding depend on velocity distribution functions of plasma particles as well as affect them due to absorption and scattering processes. The self-consistent simulation of the dust motion together with the plasma dynamics in a kinetic approach is practically unfeasible with available computational resources, because of very large difference in the time scales due to a huge dust mass, which may exceed the ion mass up to $\sim 10^{22}$ times. The using of an artificially reduced dust mass for the simulation is not reliable due to the delayed charging that may strongly affect motion of the light dust particles as we saw in the previous chapter. That was the reason why we split the plasma simulations and the dust motion in our 1D consideration. Again, such splitting is possible only neglecting the influence of a dust particle on a plasma. We can neglect the disturbance of a plasma by a dust particle when its size is small, then the dust charge which is proportional to the dust radius R_d in a plasma [40] and R_d^2 on a wall [77] is also small. It was shown in previous researches [49] that the screening radius of the dust particles is the linearized ion-electron Debye length when the dust radius is smaller than the Debye length and increases to the electron Debye length for larger dust particles. So, disturbance of a plasma by small dust particles is localized and does not affect the sheath formation. Moreover, it was also shown in [49] that the potential distribution around a small dust particle in a plasma is well described by the Debye-Hückel potential, so we could use the classical approximation of the truncated Coulomb potential for the scattering of ions by the dust particle. Nevertheless, if the dust particle size is large in comparison with the Debye length, then the modification of the local potential distribution around a dust particle due to shielding of its charge can significantly disturb the sheath formation near a wall and the dust, so they should be considered simultaneously and at least two-dimensional description of the disturbed sheath is necessary. Another important property of the boundary plasma near a wall is a strong and non-uniform electric field in the sheath, which accelerates the ion flow over the sound speed. The non-uniform electric field polarizes the dust particle, so a spherically non-symmetric own electric field makes the particle shielding more complicated and affects the absorption and Coulomb scattering of plasma particles. The problem for a dust particle in the external electric field near the

wall is even more complex, because the wall charges also are redistributed under the effects of the dust particle field and the potential structure in this multidimensional system involving high order field moments. In addition, the sheath electric field is non-uniform in space and has a gradient on the Debye length scale; therefore, the polarization of the larger dust particle than the Debye length is non-linear. One more mentioned issue is the highly accelerated ion flow in the non-uniform sheath potential. As was shown previously, the ion flow leads to anisotropic screening of the dust charge and creates the wake potential [50] behind the dust, which is thought responsible for the vertical alignment of dust particles in dust crystals [16]. All these issues make very difficult self-consistent theoretical description of properties of a large dust particle in the sheath. Therefore, computer simulations are usually used to analyze self-consistent dust particle charging and shielding. Numbers of simulations are performed to study dust charging and shielding in an ion flow [51,52,56-58]. All the works consider a dust particle immersed in uniform drifting plasma without an external electric field and a wall. Other works [55,79] consider various aspects of dust charging in a uniform external electric field either without a plasma or in a diffuse-drift approach of a highly collisional fluid. So far, there have been no self-consistent kinetic simulations of a dust particle in sheath. As the aim of our work is investigate of dust behavior in the sheath, we need to perform such self-consistent simulations to analyze the behavior of the large dust particles. We still are not able to simulate the dust and plasma dynamics simultaneously due to the different time scales, so we are restricted to self-consistent simulations of an immobile dust particle in the sheath at a given position. Nevertheless, the same difference in the dynamics time scales allows us to assume that the plasma reaches a quasi-steady state at every position of the dust particle during its motion. This means that we can simulate the dust particles at different distances from the wall and calculate the local self-consistent dust charge and acting forces and then use these local self-consistent values to analyze the dust dynamics. In this way, we can obtain the effective potential profiles for the self-consistent dust-plasma-wall interactions in a quasi-steady state. The effective potential can be obtained at spatially discrete positions and can be interpolated in between them. Such method is equivalent to solving dust dynamics equations on a spatially discrete mesh with the simulated distribution of the self-consistent field. It requires a large amount of the computational work, which is not complete yet, because the two-dimensional simulations consume significantly more computational

resources than the one-dimensional ones. The new 2D PIC/MC code for these simulations was originally developed and the simulation method is described in the next section. After confirmation of the correctness of the developed code by several test runs, we started our simulations for the dust particle on the wall as its initial position. We obtained the self-consistent simulated values of the dust charge, currents and forces acting on the dust particle on the wall position, which will be described further, for different radii of the dust particle and values of the wall potential and made the comparison with the 1D model. These results allow us to evaluate our one-dimensional model, clarify the dust shielding effect and propose modifications to the analytical approach. The further results of the developed 2D model will be published in future works.

3.2 Numerical method: self-consistent simulations

The two-dimensional PIC/MC simulation code was developed on the basis of our one-dimensional code created formerly, which was extended with additional radial dimension r and the three-dimensional $\left(\upsilon_x, \upsilon_y, \upsilon_z\right)$ velocity space was converted into the $\left(\upsilon_z, \upsilon_r, \upsilon_\theta\right)$ one, so the 1D3v model was extended to the 2D3v model. The most of procedures were modified including the plasma particles injection and absorption, the motion advancing, the weighting on a spatial mesh and the Monte-Carlo collisions procedures as well as the Poisson's equation solver with additional boundary conditions. The special care was given to the dust particle representation with the surface charge distribution. In addition to the conventional diagnostics of the plasma parameters, several new parameters are calculated, such as dust surface charge distribution and its total charge, absorbed currents by the dust particle and the acting forces on it. Below we describe the simulation method in more details.

The simulated system is schematically shown in Fig.3.2.1. The plane wall at $z = 0$ is facing the plasma injected from the left boundary of the system $z = -L_s$. The system is cylindrically symmetric around the z-axis. The additional dimension of the system is the radial r direction. The system is limited in the r direction by the outer radial boundary $r = L_r$. The system is rotationally uniform around the z-axis, so we can simulate a full-dimensional body of a dust particle with the axial symmetry.

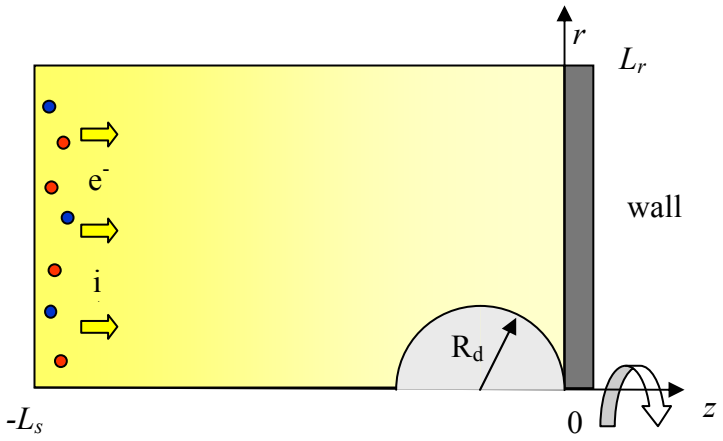

Fig. 3.2.1 *Sketch of the two-dimensional simulated system with a spherical dust particle.*

Representing the dust particle as a half-circle in the (z,r) space, we are able to simulate the spherical dust particle in the system. Other axially symmetric shapes of the dust particle are also possible, e.g. a rectangular shaped particle in the (z,r) space. The particle position on the z-axis can be arbitrary including the case of the dust particle touching the wall. There is no magnetic field in the system. The same elementary processes of the ion and electron collisions with neutral atoms as for the 1D model are included in the 2D system. The Monte-Carlo procedure for the elementary processes simulation uses the same method that was described in the 1D model, which was already three-dimensional in velocity space (1D3v). As the positions of colliding particles do not change during the elementary processes, but only their velocities change, or a particle appears/disappears at the same position, the 1D3v collisional procedures were easily transformed into present 2D3v code.

The wall and the dust particle surfaces are assumed perfectly absorbing for the incident plasma particles, so that no secondary emission is considered. As in the 1D case, the plasma is injected into the system from the left boundary. The electrons are injected with the half-Maxwellian velocity distribution function in the z direction with the fixed temperature T_e and the full-Maxwellian distribution in r direction with the same temperature T_e. Ions have the temperature T_i in the both directions for the full-Maxwellian velocity distribution along the r direction and the shifted Maxwellian distribution with the shift velocity u_0 along the z direction. The densities of ions and electrons on the left boundary are equalized to the given value n_0 to

maintain quasi-neutrality. The ion shift velocity is determined in order to avoid any unphysical potential changes at the left boundary. The left boundary of the system is transparent for outgoing particles, which are excluded from the simulation when they cross the boundary. The algorithm of the plasma particles motion, which we describe below, assures that a plasma particle can not have unphysical negative values of r coordinate during the motion.

On the outer radial boundary we applied the original "inverse-reflection" boundary conditions for the plasma particles. Since the plasma is non-uniform along the z direction and its profiles are not known a priori, we can not inject plasma particles from the outer radial boundary into the system without implying some artificial plasma conditions there. Therefore, we reflected all particles going out of the simulated system through the outer radial boundary back into the system that implies zero total particles flux through this boundary and is a common simulation technique. This flux condition is exact when there is no dust particle in the system. In this case, there is no scattering center, which can create a non-zero radial flux. When the dust particle is present in the system, the radial flux through the outer radial boundary strictly speaking is not zero. Nonetheless, it should be vanishing for sufficiently remote position of the boundary from the dust, because of the strong axial electric field in the sheath, which drives the plasma particles out of the system along the z direction. So, the reflection boundary conditions on this boundary are much better than any artificially imposed constant input flux of the plasma particles. However, the important question is following: where the reflected particle appears inside the simulated region at the next time step and what should be its velocity? The answer to this question distinguishes one reflection method from another. Usually for a periodical system in Cartesian coordinates an outgoing particle reenters the system from the opposite side or "mirror" reflection is used bouncing the particle back into the system. The "mirror" reflection assumes that another particle symmetrically enters the system form outside as the outgoing particle leaves it. This "mirror" method is valid only if there is no any force acting on the particles normally to the boundary, otherwise the symmetry is broken. None of these methods is applicable for the cylindrical geometry on the outer radial boundary, because neither periodicity nor symmetry exists there in the radial direction. Moreover, the radial centrifugal force is always directed out of the system making the "mirror" reflection senseless. To avoid

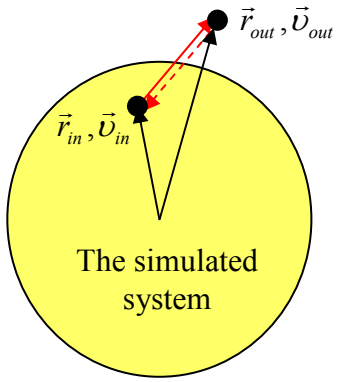

Fig. *3.2.2 Scheme of the "inverse reflection" boundary conditions for a radially outgoing particle in the cylindrical system.*

these difficulties, let's notice that the equation of motion $m\,d^2\vec{r}/dt^2 = \vec{F}$ is time reversible in a constant force field. The PIC method is discrete in time, so during a time step Δt a field solved on a spatial mesh is fixed. It means, if an outgoing particle had a position $\vec{r}_{in}$ and a velocity $\vec{\upsilon}_{in}$ at time t inside the system and moved out to a position $\vec{r}_{out}$ and a velocity $\vec{\upsilon}_{out}$ at a moment $t+\Delta t$, then a particle with the exactly opposite velocity $-\vec{\upsilon}_{out}$ at the position $\vec{r}_{out}$ at the moment t could move for the same time Δt from the position $\vec{r}_{out}$ to the position $\vec{r}_{in}$ and the velocity $-\vec{\upsilon}_{in}$ (see Fig.3.2.2). If we assume that our system is in a steady state and a local velocity distribution function of plasma particles is symmetric (in respect to the zero velocity) near the outer radial boundary, then such an "inversely symmetric" particle with the opposite velocity at the point $\vec{r}_{out}$ will always exists. Therefore, we can apply this consideration to a particle motion through the outer radial boundary of our system in the (r,θ) space to get the "inverse reflection" boundary conditions for the particles crossing the outer radial boundary

$$\begin{cases} r(t+\Delta t) = r(t) \\ \upsilon_r(t+\Delta t) = -\upsilon_r(t) \\ \upsilon_\theta(t+\Delta t) = -\upsilon_\theta(t) \end{cases}. \tag{3.2.1}$$

We assume that the motion along the z direction of the particle going out of the system through the outer radial boundary is the same as the motion of the "inversely reflected" incoming particle. This assumption is correct when the radial variation of any force acting along the z direction is not large on the $\upsilon_r \Delta t$ scale that is easy to

achieve for the sufficiently remote outer radial boundary from the dust particle and a strong electric field along the z-axis in the sheath. The same conditions are required for the in- and out-flux equality through the boundary, as was discussed above, that is automatically provided by the symmetrical velocity distribution function. Therefore, the very simple "inverse reflection" boundary conditions (3.2.1) for outgoing plasma particles through the outer radial boundary were used, which imply symmetric velocity distribution functions in the $(\upsilon_r, \upsilon_\theta)$ velocity space at the boundary. These boundary conditions are also valid for the case when a radial force is acting on particles at the outer radial boundary without any additional calculations of the particles trajectories.

The plasma particles equations of motion in cylindrical coordinates are written as

$$\begin{cases} \dot{z} = \upsilon_z \\ \dot{r} = \upsilon_r \\ \dot{\upsilon}_z = \dfrac{q}{m} E_z(z,r) \\ \dot{\upsilon}_r = \dfrac{q}{m} E_r(z,r) + \dfrac{\upsilon_\theta^2}{r} \\ \dot{\upsilon}_\theta = -\dfrac{\upsilon_r \upsilon_\theta}{r} \end{cases}, \tag{3.2.2}$$

where the dot means total time derivative, q is the charge of a plasma particle, m is its mass, $E_z(z,r)$ and $E_r(z,r)$ are the z and r components of the local electric field. As can be seen, these equations have singularity at the axis $r = 0$ that makes difficult their using for simulations. Moreover, due to a discrete time step the radial coordinate r may accidentally get a negative value during the particle motion. In order to avoid this singularity, we transform the coordinates and velocities of a particle and then solve the motion equations in the local Cartesian coordinates with the x-axis along the local θ direction and the y-axis along the local r direction (Fig.3.2.3). After updating of the particles coordinates and velocities, we transform them back to the cylindrical coordinates for charge weighting on the mesh procedure. As in the one-dimensional code, we find the particle velocities at each half time step for the diagnostic purpose.

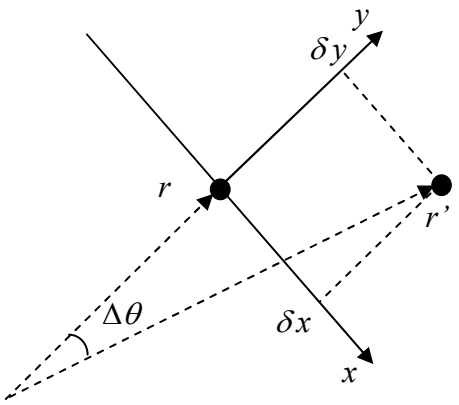

Fig. 3.2.3 *Local Cartesian system of coordinates used for solution of the particle motion equations.*

Therefore, the procedure of the particle motion is following: at the time moment t the particle's coordinates and velocities are

$$\left(z, r, \upsilon_z, \upsilon_r, \upsilon_\theta\right)\Big|_t, \tag{3.2.3}$$

then the velocities and the components of the local electric filed are transformed as

$$\begin{cases} \upsilon_z = \upsilon_z \\ \upsilon_y = \upsilon_r \\ \upsilon_x = \upsilon_\theta \\ E_y = E_r\left(z, r\right) \\ E_z = E_z\left(z, r\right) \end{cases}, \tag{3.2.4}$$

and $E_x = E_\theta = 0$ due to cylindrical symmetry. After a half time step, the new particle's velocities are

$$\begin{cases} \tilde{\upsilon}_x \equiv \upsilon_x\left(t + \Delta t/2\right) = \upsilon_x\left(t\right) \\ \tilde{\upsilon}_y \equiv \upsilon_y\left(t + \Delta t/2\right) = \upsilon_y\left(t\right) + \dfrac{q}{m} E_y \dfrac{\Delta t}{2} \\ \tilde{\upsilon}_z \equiv \upsilon_z\left(t + \Delta t/2\right) = \upsilon_z\left(t\right) + \dfrac{q}{m} E_z \dfrac{\Delta t}{2} \end{cases}. \tag{3.2.5}$$

Using these velocities we can find the displacement of the particle in the local Cartesian system of coordinates during the motion on time Δt

$$\begin{cases} \delta x = \tilde{\upsilon}_x \Delta t \\ \delta y = \tilde{\upsilon}_y \Delta t \\ \delta z = \tilde{\upsilon}_z \Delta t \end{cases}, \tag{3.2.6}$$

and the new cylindrical coordinates of the particle at the moment $t+\Delta t$

$$\begin{cases} z' \equiv z(t+\Delta t) = z + \delta z \\ r' \equiv r(t+\Delta t) = \sqrt{(r+\delta y)^2 + \delta x^2} \end{cases}. \tag{3.2.7}$$

The new velocity components in the cylindrical system of coordinates at the time $t+\Delta t$ are written then

$$\begin{cases} \upsilon_z' \equiv \upsilon_z(t+\Delta t) = \tilde{\upsilon}_z + \dfrac{q}{m} E_z(z',r') \\ \upsilon_r' \equiv \upsilon_r(t+\Delta t) = \tilde{\upsilon}_y \cos\Delta\theta + \tilde{\upsilon}_x \sin\Delta\theta + \dfrac{q}{m} E_r(z',r') \dfrac{\Delta t}{2} \\ \upsilon_\theta' \equiv \upsilon_\theta(t+\Delta t) = \tilde{\upsilon}_x \cos\Delta\theta - \tilde{\upsilon}_y \sin\Delta\theta \end{cases}, \tag{3.2.8}$$

where $\Delta\theta$ is the rotation angle of the particle in the θ direction that satisfies the relations

$$\begin{cases} \cos\Delta\theta = \dfrac{r+\delta y}{r'} \\ \sin\Delta\theta = \dfrac{\delta x}{r'} \end{cases}. \tag{3.2.9}$$

As can be seen from equation (3.2.7), r' can not have negative values and has zero value only when $r+\delta y = 0$ and $\delta x = 0$. The last situation corresponds to the purely radial motion with $\Delta\theta = \pi$, thus, the uncertainty in formulae (3.2.9) should be resolved as $\cos\Delta\theta = -1$ and $\sin\Delta\theta = 0$. Therefore, using this algorithm according to (3.2.3-9), we can avoid the singularity of the plasma particles motion equations at the $r = 0$ axis and assure that the particles can not have negative values of the radial coordinate r numerically.

The PIC simulation method requires that the electric field distribution in the system should be found by solving the Poisson's equation on a spatial mesh. We used a rectangular uniform mesh in (z,r) space with constant cell sizes Δz and Δr in axial and radial directions, respectively (Fig.3.2.4). The mesh covers the entire system including the interior of the dust particle and the first node of the mesh is placed at the origin of the coordinate system $(z=0, r=0)$. We use an index $i = 0..N$, where $N = L_s/\Delta z$, for numbering the nodes in the axial direction, and an index $j = 0..M$, where $M = L_r/\Delta r$, for the nodes in the radial direction. The first node has $i = 0$ and

$j = 0$. To find the field distribution we solve the Poisson's equation in the following form

$$\nabla\kappa(z,r)\nabla\varphi(z,r) = -\rho^{free}(z,r)/\varepsilon_0 \,, \tag{3.2.10}$$

where $\rho^{free}(z,r)$ is the local density of free charges, $\varphi(z,r)$ is the local electric potential, and $\kappa(z,r)$ is the local dielectric constant, which has value $\kappa = \kappa_d$ inside the dust particle and $\kappa = 1$ outside it. The Poisson's equation (3.2.10) can be written in finite differences for a non-boundary (i,j) node of our spatial mesh ($i \neq 0, N$ and $j \neq 0, M$) as following

$$A_{i,j}^{i,j+1}\varphi_{i,j+1} + A_{i,j}^{i+1,j}\varphi_{i+1,j} + A_{i,j}^{i,j}\varphi_{i,j} + A_{i,j}^{i-1,j}\varphi_{i-1,j} + A_{i,j}^{i,j-1}\varphi_{i,j-1} = -\rho_{i,j}^{free}/\varepsilon_0 \,, \tag{3.2.11}$$

where the coefficients $A_{i,j}$ are

$$\begin{cases} A_{i,j}^{i.j+1} = \dfrac{1}{2j\Delta r^2}\left(\kappa_{i,j+1} + \kappa_{i,j}\right)\left(j + \dfrac{1}{2}\right) \\ A_{i,j}^{i+1,j} = \dfrac{1}{2\Delta z^2}\left(\kappa_{i+1,j} + \kappa_{i,j}\right) \\ A_{i,j}^{i,j} = -\dfrac{1}{2j\Delta r^2}\left[\kappa_{i,j+1}\left(j + \dfrac{1}{2}\right) + 2j\kappa_{i,j} + \kappa_{i,j-1}\left(j - \dfrac{1}{2}\right)\right] - \dfrac{1}{2\Delta z^2}\left(\kappa_{i+1,j} + 2\kappa_{i,j} + \kappa_{i-1,j}\right) \\ A_{i,j}^{i-1,j} = \dfrac{1}{2\Delta z^2}\left(\kappa_{i,j} + \kappa_{i-1,j}\right) \\ A_{i,j}^{i,j-1} = \dfrac{1}{2j\Delta r^2}\left(\kappa_{i,j} + \kappa_{i,j-1}\right)\left(j - \dfrac{1}{2}\right) \end{cases} . \tag{3.2.12}$$

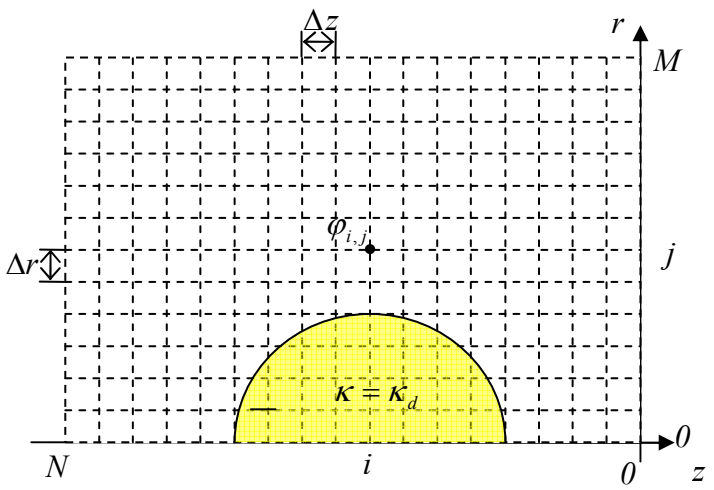

Fig. 3.2.4 *Sketch of the spatial mesh used for the Poisson's equation solving.*

The coefficients $A_{i,j}$ (3.2.12) are written for the general case without applied boundary conditions. Therefore, now for the non-boundary points of the system we have $(N-1)(M-1)$ linear equations and $(N+1)(M+1)-4$ unknowns, thus $2(N+M-2)$ equations of boundary conditions are necessary. The boundary conditions should be written for the boundary points of the system. We assume that the wall has the fixed potential φ_w and the potential of the left axial boundary of the system is zero. At the axis $r=0$ the radial component of the electric field should be zero due to the cylindrical symmetry of the system and at the outer radial boundary $r=L_r$ we also assume the zero radial electric field. The last condition is satisfied only approximately when the dust particle exists in the system, which creates a radial electric field, but if the outer radial boundary is sufficiently far from the dust particle then the radial electric field at the boundary can be neglected. The screening of the dust charge by a plasma also helps to reduce the radial electric field at the outer radial boundary. Later we show how far should be placed the outer radial boundary from the dust particle for physically correct solutions of a potential. The boundary conditions described above can be written as

$$\begin{cases} \varphi_{0,j}=\varphi_w, & j=1..(M-1) \\ \varphi_{N,j}=0, & j=1..(M-1) \\ \varphi_{i,1}-\varphi_{i,0}=0, & i=1..(N-1) \\ \varphi_{i,M}-\varphi_{i,M-1}=0, & i=1..(N-1) \end{cases}. \tag{3.2.13}$$

Here we expressed the radial electric field at the boundaries as a one-side finite difference derivative of the potential. Now the system of linear equations (3.2.11-13) is closed and can be solved. Let's note that the indices of the mesh nodes used in the equation for the point (i,j) differ only on ± 1 from the values i and j. Therefore, the matrix of the system of linear equations (3.2.11-13) can be written as a five-diagonal sparse matrix, which we solved by the Gauss elimination method for bounded matrices. After finding of the electric potential at the mesh nodes, we calculate the components of the eclectic field as a finite difference centered derivative for all non-boundary mesh nodes and as a one-side derivative for the boundary nodes. We used the matrix method for solving of the Poisson's equation (3.2.10), because the (z,r) variables in this equation are inseparable due to the spherical shape of the dust particle

and the corresponding half-circle shape of the local dielectric constant distribution $\kappa(z,r)$. In the case of a cylindrical dust particle and a rectangular shape of the local dielectric constant distribution $\kappa(z,r)$, the Poisson's equation (3.2.10) can be solved by the FFT (Fast Fourier Transform) or the Cycle Reduction methods [70], which are much faster than the matrix method. Nevertheless, the matrix method is more universal, because we can use various boundary conditions (any combination of given potentials and normal components of the electric field) instead of (3.2.13) as well as it is possible to set any point of the system to a given potential that allows placing of arbitrary shaped bodies under different potentials inside the system. Thus, the described solution method of the Poisson's equation provides significant flexibility that can be applicable for different problems.

The free charge density $\rho^{free}(z,r)$ in the RHS of the Poisson's equation (3.2.10) includes charges of plasma particles in the system as well as charges absorbed by the dielectric dust particle from plasma, although they are placed on the dust surface. For a numerical solution of the finite difference Poisson's equation (3.2.11), we need to know values of the free charge density at the nodes of the spatial mesh. The free charges in a plasma are distributed on the spatial mesh according to the standard first order Cloud-In-Cell procedure [69] accounting difference of the cells volumes in the cylindrical geometry. The charge induced by an electric field on the dust particle is the bound charge with $\rho^{bound}(z,r)$. The sum of the free and bound charges is the total charge, which satisfies the conventional Poisson's equation

$$\nabla^2\varphi(z,r) = -\left[\rho^{free}(z,r) + \rho^{bound}(z,r)\right]/\varepsilon_0 . \qquad (3.2.14)$$

We should note here that we needn't to know the bound charge to solve equation (3.2.10), but it can be calculated from (3.2.14) using the solution of (3.2.10). Let's consider two limit cases of the dust conductivity: the ideally conductive or ideally insulating dust particle. In the former case, the dust dielectric constant $\kappa_d \to \infty$, which we simulate by a sufficiently large value $\kappa_d = 10^6$, and in the latter case, the dust dielectric constant can have any value. For the perfectly insulating dust particle we assume that the plasma charges absorbed by a dust particle are stick at the point, where they cross the dust surface. To treat the absorbed charges we introduce an additional uniform grid with the angle ϑ on the dust surface with K cells (Fig.3.2.5). Each cell accumulates the free absorbed charges in it that form the free

charge of the cell, which is assigned to its center. The free charge of the cell, then, is also weighted on the spatial mesh of the system to solve the Poisson's equation (3.2.10).

In the case of a perfectly conductive dust particle detached from the wall, all charges on the dust surface are strictly speaking free. Nevertheless, we keep the separation of the dust surface charge on the free (absorbed from a plasma) charge and the bound charge, which is zero in total, but can be non-uniformly distributed on the dust surface with positive and negative values. This separation allows us to distribute the free dust charge arbitrarily on the conductive dust surface, because the artificial bound charge will be automatically redistributed to keep almost zero electric field inside the dust particle due to the dust dielectric constant with a very high value, according to equation (3.2.10). To minimize the numerical errors we distributed the free charge of the conductive dust particle uniformly on its surface, and then all non-uniformity of the dust surface charge distribution is kept by the bound dust charge.

In the case when the perfectly conductive dust particle is attached to the wall, an external source keeps constant potential of the wall and the attached dust. The equality of the dust potential to the one of the wall is assured by the high value of the dust dielectric constant κ_d, which provides practically zero electric field inside the dust particle, and at least one common point of the dust particle connected with the wall. In this case, the total bound dust charge can have non-zero values due to

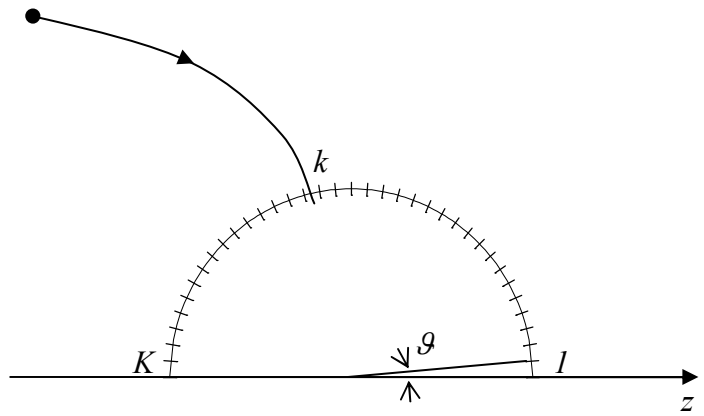

Fig. 3.2.5 *Dust surface mesh for the absorbed charge calculations.*

redistribution of charges between the dust and the wall in order to keep the common constant potential. As the common constant potential is already assured by the boundary conditions (3.2.13) and the sufficiently high κ_d value, this redistribution is obtained automatically solving the Poisson's equation (3.2.10).

After finding of the electric field distribution in the system, we can calculate the normal to the dust surface component of the electric field E_n^k at the centers of the dust surface grid cells using linear interpolation between the spatial mesh nodes inside the system. Then, the total charge density at the *k*-th grid point on the dust surface, σ_k^{total}, can be calculated as

$$\sigma_k^{total} = \frac{\sigma_k^{free}}{\kappa_d} + \varepsilon_0 E_n^k \frac{\kappa_d - 1}{\kappa_d}, \tag{3.2.15}$$

where σ_k^{free} is the free dust surface charge density at the *k*-th grid point on the dust surface. The total dust charge is then

$$Q_d = \sum_{k=1}^{K} \sigma_k^{total} S_k , \tag{3.2.16}$$

and the total electrostatic force acting on the dust particle along the z-axis is

$$F_{el} = \sum_{k=1}^{K} \left(E_z^k - \frac{\sigma_k^{total}}{2\varepsilon_0} \cos\left[\vartheta \left(k - \frac{1}{2} \right) \right] \right) \sigma_k^{total} S_k , \tag{3.2.17}$$

where E_z^k is the axial component of the electric field at the center of the *k*-th cell of the dust surface grid, S_k is the surface area of the *k*-th cell of the dust surface grid. The radial or rotational force on the dust particle is zero due to the cylindrical symmetry of the system. This total electric force acting on the dust particle includes all kinds of electrostatic interaction of the dust particle with the wall and the plasma; therefore, it includes the electrostatic force created by the field of the Debye sheath, the electrostatic image force as well as the drag force due to Coulomb scattering both of ions and electrons. We will discuss this issue later in this chapter. The drag force on the dust particle due to the absorption can be easily obtained by calculation of the momentum transfer rate to the dust particle of the absorbed ions and electrons.

For testing of the developed two-dimensional code using the numerical methods described above, we simulated the collisionless sheath without a dust particle. In this case, the plasma should be uniform in the radial direction and can be described

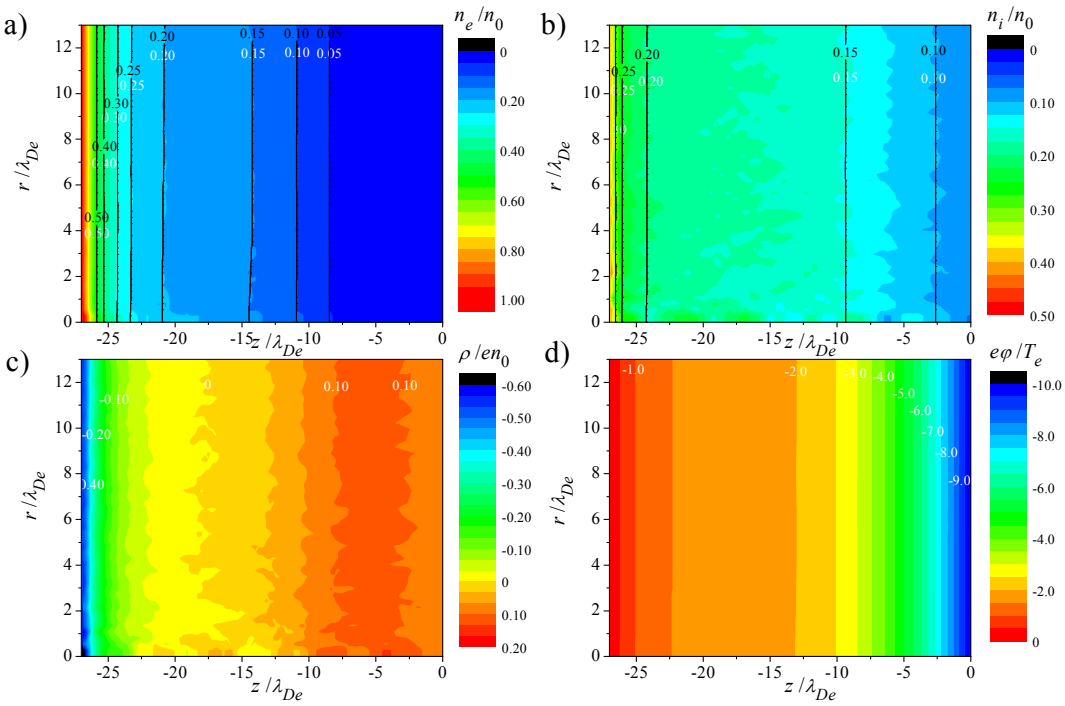

Fig. 3.2.6 *Spatial distributions of the electron (a), ion (b) and charge (c) densities as well as electric potential (d) in the simulated collisionless sheath and comparison with the theoretical analysis (solid black lines).*

with the theoretical one-dimensional model (Section 2.1.1). In Fig.3.2.6, the simulated spatial distributions of the electron, ion and charge densities as well as the potential distribution in the collisionless sheath are shown as color map diagrams, the solid black lines inside the diagrams show the theoretical values of the electron and ion densities calculated according to formulae (2.1.8-9). The simulations have done for the wall potential fixed at $e\varphi_w/T_e = -10$, the ratio of the ion temperature to the electron one $T_i/T_e = 1$ and the equal injected electron and ion densities $n_{e0}^{(+)} = n_{i0}^{(+)} = n_0/2$. The number of used super-particles of each sort was 262144 and the spatial mesh has 100×50 cells in the axial and radial directions, respectively. As can be seen, there is a very good agreement between the simulation and the theoretical results. The ion density is more fluctuating in comparison with the electron density, because the averaging time for the diagnostics was order of the ion plasma oscillation period. Also the level of the fluctuations is relatively high near the axis of symmetry due to smallness of volumes of the spatial mesh cells and, correspondingly, smaller number of super-particles per cell. Nevertheless, the fluctuation level is not very large and does not affect potential formation as can be seen in Fig.3.2.6(d). Moreover, we

can not see any significant radial non-uniformity of the plasma even near the outer radial boundary, thus the developed "inverse reflection" boundary conditions are proved to be correct.

For the next test we put a spherical conductive dust particle attached to the wall in a uniform external electric field without a plasma. In this case, the theoretical consideration [77] gives us the potential distribution in the system and the charge of the dust particle. In Fig.3.2.7, the simulated and the theoretical charges of the dust particle of various radii are shown for the external electric field 10^5 V/m and the radius of the system $L_r = 50\,\mu$m. As can be seen, the theoretical and the simulated dust charges are in a good agreement for the values of the R_d/L_r ratio up to approximately 0.4. For the larger values of the ratio, the dust charge is disturbed by too close position of the radial outer boundary of the system and imposed there zero component of the radial electric field. Therefore, we can say that our field boundary conditions are valid when the system's radius at least 2.5 times larger than the radius of the dust particle. In the presence of a plasma, the field created by the dust particle decays quicker, so we can safely use the obtained validity criterion for the field boundary conditions $L_r/R_d > 2.5$.

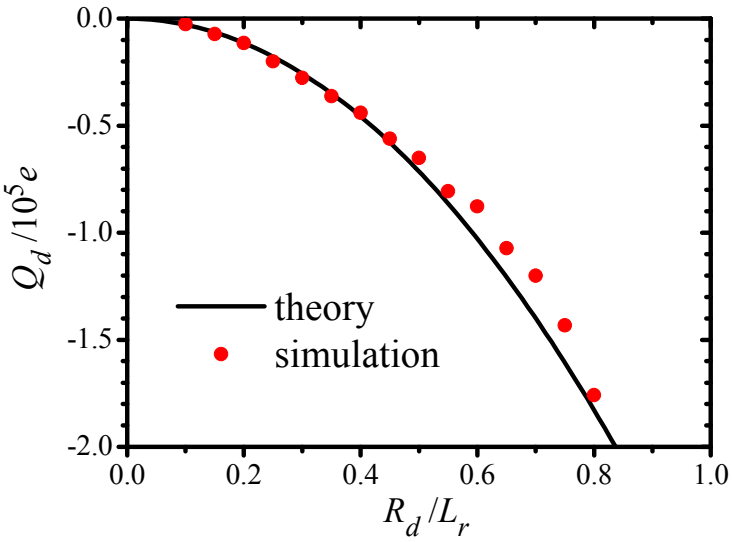

Fig. 3.2.7 *Dependence of the simulated charge of the dust particle attached to the wall in uniform external electric field* 10^5 V/m *on the ratio of the dust radius to the radius of the system.*

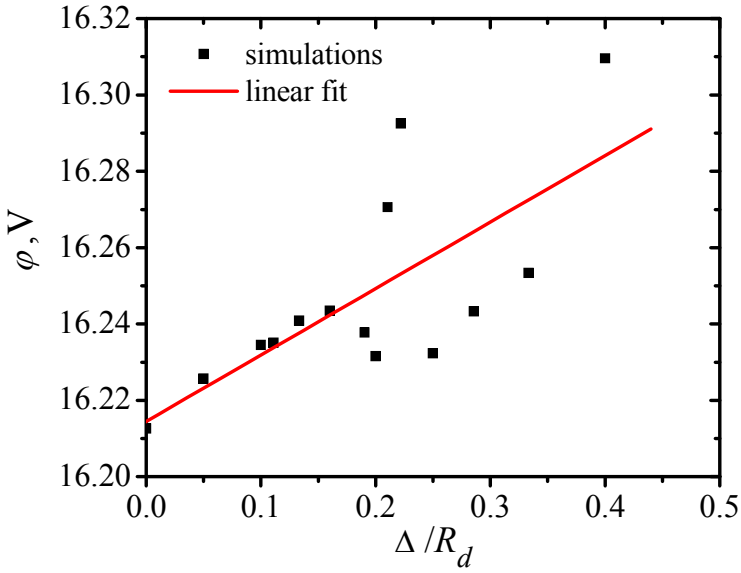

Fig. 3.2.8 *Simulated (dots) and fitted (red line) potential dependence on the cell sizes* $\Delta = \Delta z = \Delta r$ *at the point, which is distant on the dust radius length from the dust surface, for the dielectric spherical dust particle with the radius* $R_d = 1\,\mu$m *and dielectric constant* $\kappa_d = 10$, *with its center placed at the distance* $2\,\mu$m *from the wall in the uniform external electric field* 10^6 V/m *without plasma.*

Further, we check the effect of the spatial mesh size on the potential solution around a dust particle. If the mesh is too coarse then the spherical shape of the dust particle may not be reproduced well and the electric field distribution around the dust particle is disturbed. For this purpose we simulated the dielectric spherical dust particle with the radius $R_d = 1\,\mu$m and the dielectric constant $\kappa_d = 10$, with its center placed at the distance $2\,\mu$m from the wall in the uniform external electric field 10^6 V/m without a plasma. In Fig.3.2.8, the simulated potential at the point on the axis of symmetry, which is $4\,\mu$m far from the wall and $1\,\mu$m from the dust surface, is shown for the different sizes of the spatial mesh cells $\Delta = \Delta z = \Delta r$. The red line in Fig.3.2.8 is the linear fit of the simulated potentials at the selected point. As can be seen, the simulated potential converges to the value $\varphi \approx 16.215$ V as the cell size approaches to zero $\Delta \to 0$. This value can be considered as close to the true solution of the potential at the selected point. The value of the undisturbed by the dust particle potential at this point is $\varphi_0 = 16$ V, therefore the potential disturbance introduced by the uncharged polarized dust particle is about $\varphi_p \approx 0.215$ V. The convergence is good

for the cell sizes smaller than approximately $0.15R_d$ and the relative error of the φ_p is less then 10%, while the relative error of total potential is about 0.1%. Therefore, we can expect a good approximation of the dust particles shape, when there are at least six cells per a dust radius $R_d/\Delta \geq 6$.

In this section we described the numerical method, the boundary conditions and their applicability for the two-dimensional self-consistent simulations of a conductive or dielectric spherical dust particle in the boundary plasma including the case of the dust particle attached to the wall. The originally developed PIC code based on the described method is applicable to analyze the dust particles properties at the wall position self-consistently with the sheath formation and verify our one-dimensional consideration results.

3.3. Results of self-consistent simulations

In this section we describe present results of the two-dimensional self-consistent simulations of the conductive spherical dust particle placed on the electrically biased wall in contact with a plasma. The plasma is injected from the left boundary of the system, where electrons have the Maxwellian and hydrogen ions have the shifted Maxwellian velocity distribution functions with the same densities equal $n_0 = 10^{12}$ cm^{-3} and the temperatures $T_e = T_i = 3$ eV, which are typical for the plasma in the divertor region of fusion devices. The injected ion velocity distribution function has the shift on velocity $u_0 = 3.284 \times 10^4$ m/s in order to satisfy the Bohm criterion [21,24] of the sheath formation. The wall potential and the dust particle radius are the parameters in order to analyze corresponding dependencies. The elementary processes were not included in the simulations and the presheath was not produced, because the dust particle was placed on the wall in the Debye sheath region and the computationally consuming presheath formation is not particularly an important factor of the dust particle properties on the wall. For the selected plasma parameters the electron Debye length in the bulk plasma is $\lambda_D = 12.9$ μm, the electron plasma frequency equals $\omega_{pe} = 5.6 \times 10^{10}$ s^{-1} and the ion plasma frequency is $\omega_{pi} = 1.3 \times 10^9$ s^{-1}. The steady state of the plasma without a dust particle was calculated once, after that the dust particle of variable radius was put in the system and the simulations restarted.

This allowed us to save the computational time, because the new steady state after the dust particle insertion usually was achieved for $10\omega_{pi}^{-1}$. The system size varied to satisfy the model validity conditions described in the previous section and typically is $200\times100\,\mu$m in the axial and radial directions, respectively. The size of the spatial mesh cell typically was $1\,\mu$m in the both directions. The simulation of one regime usually takes from 10 to 40 hours using four Itanium 2GHz processors.

The typical simulation results of the dust particle on the plasma-facing wall are shown in Fig.3.3.1, where the spatial distributions of the electric potential, the charge density, the electron and ion densities, the ion flow velocity in the axial direction and the effective electron temperature are plotted for the dust radius $R_d = 20\,\mu$m and the wall potential $\varphi_w = -15$ V. The surface of the dust particle is indicated by the white line. As can be seen from the potential distribution (Fig.3.3.1(a)), the equipotential lines smoothly bend around the dust particle, so that the sheath edge is not strongly affected by the dust particle presence, instead the sheath width is compressed in front of the dust particle. Distribution of the potential in the radial direction shows that the screening length of the dust particle is about the Debye length λ_D. The interesting fact is that there is the positive charge accumulation in front of the dust particle (Fig.3.3.1(b)). In the studies of a dust particle in an ion flow without the wall [52], we saw that a positive charge accumulates behind the dust particle, where the wake potential is formed due to the scattering of ions by the charged particle. In our case with the wall presence, the ion scattering significantly differs from the infinite plasma case, because the scattered ions are absorbed by the wall and have practically no decelerated part of their trajectories. The formation of the positive charge in front of the dust particle becomes clearer if we compare the distributions of the ion (Fig.3.3.1(c)) and electron (Fig.3.3.1(d)) densities. The ion density profiles are almost undisturbed by the dust particle, while the electron density decreases significantly around it. Therefore, the positively charged region in front of the dust is formed due to lack of electrons, as near the wall, but with the higher ion density, as in the middle of the sheath. Also, we can conclude from this observation that the dust is screened by electrons and not by ions, so the screening length is comparable with the electron Debye length. There is a shadow region in the space between the wall and the dust particle, where the densities of electrons and ions are both relatively low, the potential is close to the wall potential and the electric field is

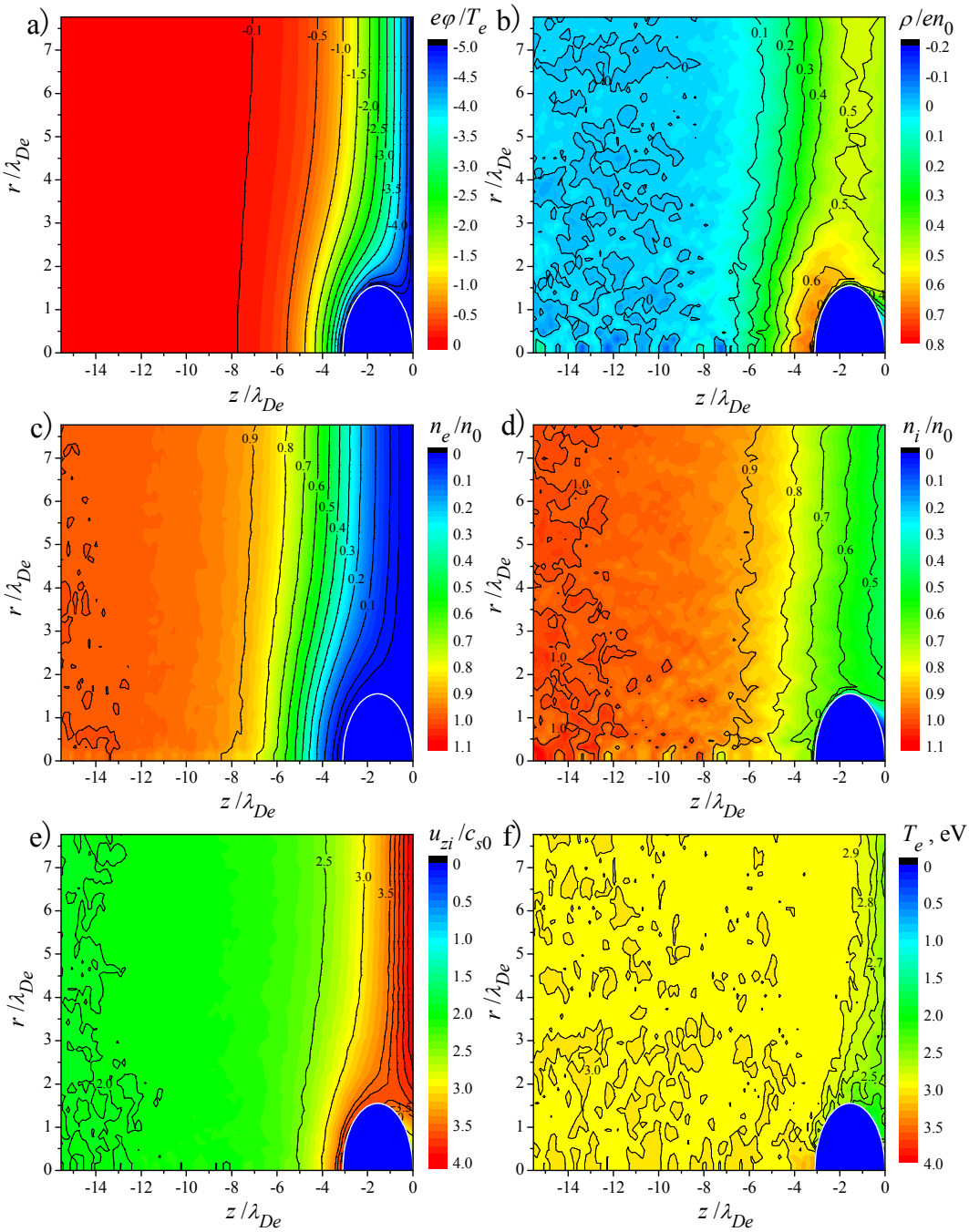

Fig. 3.3.1 *Simulated spatial distributions of the electrostatic potential (a), the charge density (b), the electron (c) and the ion (d) densities, the ion flow velocity in the axial direction (e) and the effective electron temperature (f) in the sheath with the conductive spherical dust particle on the wall.*

small in comparison with the electric field at the wall far from the dust particle. As can be seen from Fig.3.1.1(e) the ions are accelerated along the z-axis near the front side of the dust particle to almost the same speed as at the wall. At the same time, the ion density is higher there than that near the wall far from the dust, therefore the axial flux of the ions is increased in front of the dust particle that testifies about attraction of ions along the radial direction. There are also scattered ions going into the shadow region behind the dust particle. In Fig.3.1.1(f), the effective electron temperature distribution in the simulated system is shown. We can see that the effective temperature decreases near the wall and in the shadow region, where the potential is close to the wall potential. This can be explained by the effect of truncation of the electron velocity distribution function due to absorption of the high-energy electrons by the wall and the dust. We currently can not explain the small spot of hot electrons near the front dust side that is, probably, a numerical effect due to small number of representative super-electrons there and requires additional investigations. This qualitative description of the self-consistent sheath formation with the conductive spherical dust particle on the wall, which size exceeds the Debye length, shows the one-side shielding of the dust particle that weakens the effect of the dust on the sheath edge and creates the specific scattering field for the ions.

In Fig.3.3.2, the simulated total force acting on the dust particle on the plasma-facing wall (black dots) without the gravitational force and its prediction by the one-dimensional model, both of which are normalized by the geometrical cross section of the particle, are shown as functions of the dust particle radius for the two values of the wall potential: the floating wall potential without a dust particle $e\varphi_w/T_e = -2.17$ and the deeper than floating potential value $e\varphi_w/T_e = -5.0$. As we can see, for the deeper wall potential the total force changes its sign from negative (from the wall direction) for small dust particle radii to positive (to the wall direction) for the bigger dust particles and there is the critical value of the dust radius around $R_d = 1.8\lambda_D$. Therefore, the simulations confirm the existence of the first critical dust radius, so that the dust particles with larger radii than the first critical one can not leave the wall. In the case of the shallower wall potential, the values of the total force are more positive for the same dust size in comparison with the deeper wall potential case. That qualitatively agrees with the one-dimensional model prediction and implicitly support the threshold potential existence.

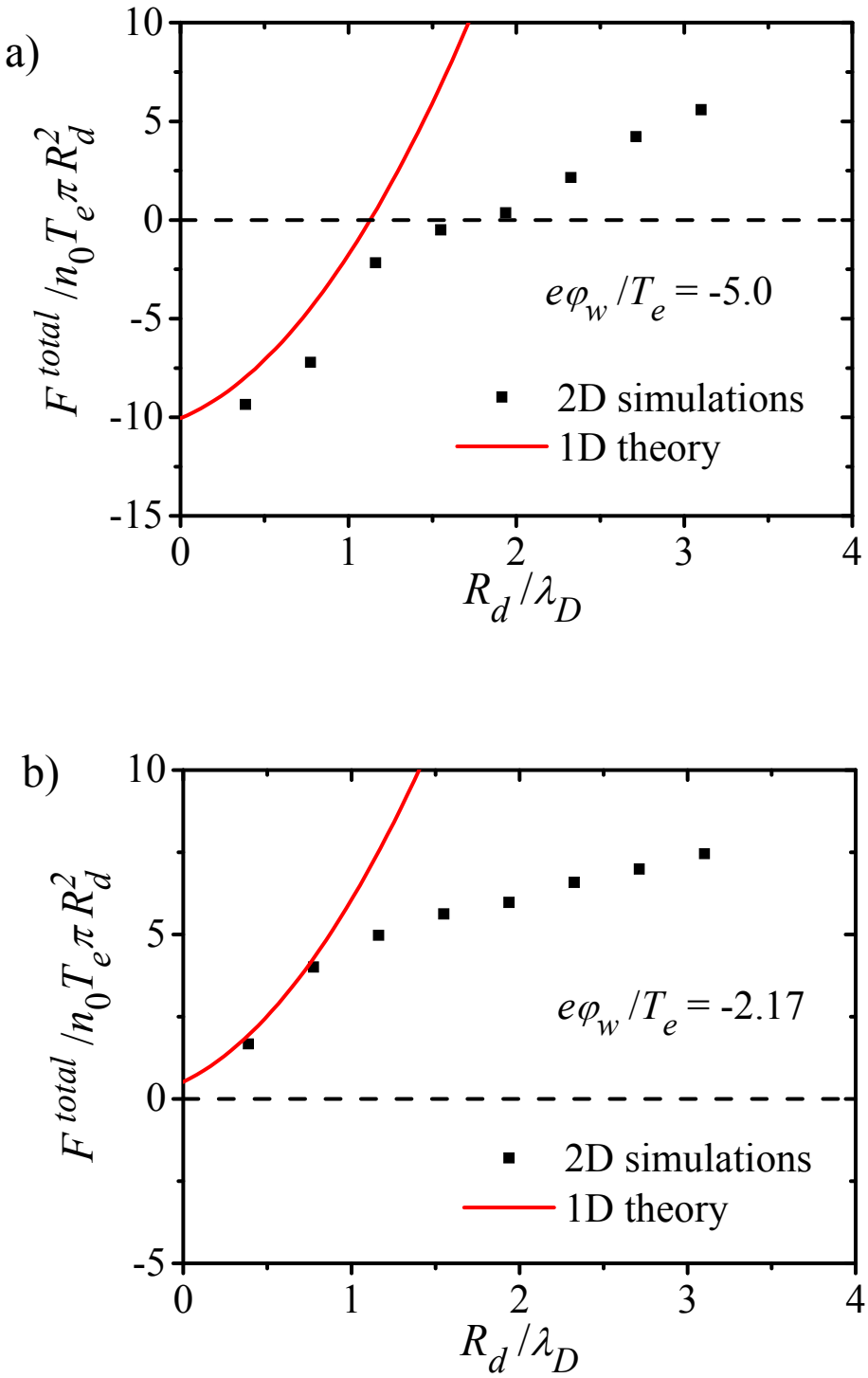

Fig. 3.3.2 *Simulated (dots) and theoretical (red lines) dependences on the dust radius of the total force acting on the spherical conductive dust particle placed on the plasma-facing wall for the two values of wall potential* $e\varphi_w/T_e = -5.0$ *(a) and* $e\varphi_w/T_e = -2.17$ *(b).*

Unfortunately, the simulation of very small dust particles is difficult, because we need a tiny mesh in this case, and as the first critical dust radius is zero for the threshold potential, it is hard to simulate. However, the simulated total force is close to the theoretically predicted parabolic dependence for the dust particles smaller than the Debye length λ_D. At the same time, there is the difference between the simulated and the theoretical total forces for the larger dust radius than the Debye length, as we suggested. For the both values of wall potentials, the simulated dependences of the total force on the dust radius are much weaker than the theoretical parabolic one for the large dust particles. That leads to the bigger values of the simulated first critical dust radius than that predicted theoretically.

To clarify the reason leading to the difference between the one-dimensional theoretical and the simulation results, we analyze properties of the dust particle on the plasma-facing wall. In Fig.3.3.3, the dependences of the charge of the dust particle placed on the plasma-facing wall on the particle radius are shown according to the self-consistent simulations (circles) and the one-dimensional theoretical formula (2.2.15) (red line). The theoretical values of the dust charge are proportional to the square of the dust radius and are linearly proportional to the electric field at the wall,

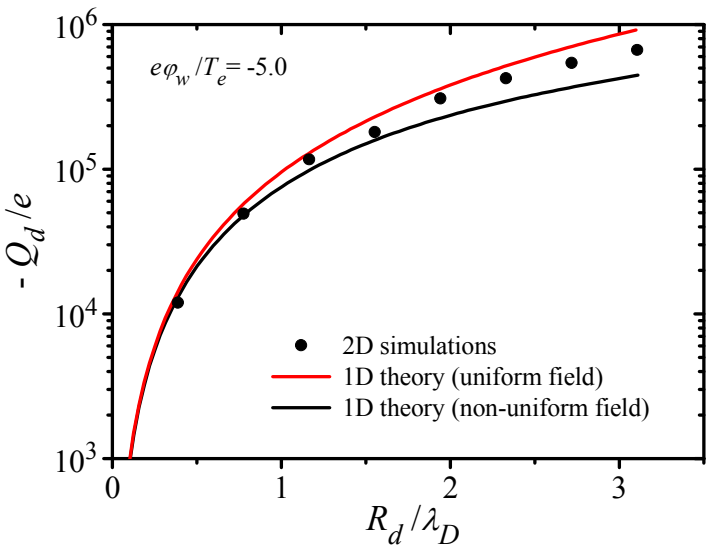

Fig. 3.3.3 *Dependence of the charge of the spherical conducting dust particle placed on the wall on the particle radius for the wall potential value* $e\varphi_w/T_e = -5.0$. *The black dots show the results of the 2D simulations, the red line represents one-dimensional analytical approach for uniform external electric field and the black line shows the analytical dependence taking into account the non-uniform external electric field.*

which was taken from the simulation of the sheath without a dust particle and equals $E_w = 2.15 T_e / e\lambda_D$. As we can see in Fig.3.3.3, the absolute values of the simulated dust charge are smaller than the theoretically obtained ones, in particular for the bigger dust than the Debye length. This leads to reduction of the repulsive electrostatic force acting on the bigger dust particles than the Debye length in comparison with the 1D theoretical prediction and can not explain the weakening of the total force acting on the big dust particles (Fig.3.3.2). Here we should note that the theoretical formula (2.2.15) is obtained under the assumption of the uniform electric field near the wall on the scale of the dust particle radius. However, the electric field in the sheath is not uniform as we saw from the sheath simulations in the section (2.1.3). As was described earlier, in the 1D theoretical approach we can not take into account the self-consistent shielding of the dust particle in a plasma, but we can consider the spatial variation of the unperturbed electric field by the dust particle in the sheath near the wall. The charge of a spherical conductive dust particle placed on a conductive wall in a non-uniform external electric field can be solved analytically using the expansion of the field potential on the z coordinate

$$\varphi(z) = \sum_{k=0}^{k_{\max}} h_k z^k \ , \tag{3.3.1}$$

where h_k are dimensional coefficients of the expansion, i.e. h_0 is the wall potential and $-h_1$ is the electric field at the wall. The solution (see Appendix C) gives the dust charge in the form of series of powers of the dust particle radius R_d

$$\begin{aligned} Q_d = -2\pi R_d^2 \varepsilon_0 \{ & h_1 I_{qc2} + h_2 \frac{1}{3}\left(\frac{I_{q1}}{\beta_0^2} + \frac{I_{qc2}}{\beta_0} + I_{qc3} \right) R_d + \\ & + h_3 \frac{1}{15}\left(\frac{6 I_{q1}}{\beta_0^3} + \frac{3\left(I_{qc2} + I_{q2}\right)}{\beta_0^2} + \frac{3 I_{qc3}}{\beta_0} + I_{qc4} \right) R_d^2 + \ldots \} \end{aligned} , \tag{3.3.2}$$

where $\beta_0 = \frac{1}{2}$, and the coefficients I_{qn} and I_{qcn} are

$$I_{qn} = \int_0^\infty \lambda^{n-1} e^{-2\beta_0 \lambda} d\lambda = \frac{\Gamma(n)}{(2\beta_0)^n} , \tag{3.3.3}$$

$$I_{qcn} = \int_0^\infty \frac{\lambda^{n-1} e^{-\beta_0 \lambda}}{\sinh(\beta_0 \lambda)} d\lambda = \frac{2}{(2\beta_0)^n} \Gamma(n) \zeta(n) . \tag{3.3.4}$$

Here, $\Gamma(n)$ is the Gamma function and $\zeta(n)$ is the Riemann's Zeta function. The first term in formula (3.3.2) corresponds to the dust charge on the wall in the uniform electric field with the value $-h_1$ and coincides with formula (2.2.15). Hence, we can show that the value of the form factor for a spherical dust particle is $\xi_q = 2I_{qc2} = 2\pi^2/3$. In Fig.3.3.3, the analytical dependence of the dust particle charge on its radius, which takes into account non-uniformity of the electric field in the sheath, is shown by the black line. The potential distribution in the sheath was simulated without the dust particle for the same plasma parameters as the simulations with the dust particle, and then the potential was expanded on the z coordinate according to (3.3.1). The expansion up to the third order of z was good on the range $-6.2\lambda_D \le z \le 0$. Correspondingly, the dust charge was calculated according to (3.3.2) up to the term proportional to R_d^3 that is valid for $-3.1\lambda_D \le R_d \le 0$. The higher orders in the expansion were checked to make no significant improvement in the accuracy for the indicated range. As we can see in Fig.3.3.3, accounting of the electric field non-uniformity the reduction of the theoretical estimation of the dust particle charge is significant for the bigger dust particles than the Debye length, while for the smaller particles we have very good agreement with the simulation results. The absolute value of the theoretical dust charge in the non-uniform electric field is lower than the simulated one for the big particles. As the only effect, which was not taken into account in the dust charge calculation in the non-uniform external electric field, is the dust shielding by a plasma, then this effect is responsible for the difference between the simulated dust charge and the one-dimensional theoretical consideration in the non-uniform external field. Therefore, the plasma shielding of the dust particle placed on the plasma-facing wall leads to the increase of the negative dust charge. Physically this effect is reasonable, because the plasma shielding causes sharper variation of the potential near the dust particle, thus it enhances the electric field at the dust particle surface and, consequently, its surface charge density. Thus, the effect of the dust shielding by a plasma is opposite to the effect of the non-uniform electric field, so they partially compensate each other. Due to this the simulated dust charge is comparatively close to the theoretical one in the uniform electric field as shown in Fig.3.3.3.

Let's further consider the electron and ion fluxes on the dust particle placed on the wall. In Fig.3.3.4, the dependence of the electron current density to the dust particle is shown as a function of the dust radius for the two cases of the wall potential $e\varphi_w/T_e = -2.17$ and -5.0. As we can see, the electron current density is practically independent of the dust particle radius. It shows that we should be careful of using the OML expression for the electron current to the dust (2.2.2).

In the particular case, when the conductive dust particle is attached to the wall, its potential is fixed to the wall potential value and does not depend on the dust charge and size, as for the dust particle floating in a plasma. Therefore, the electron density near the dust surface $n_e(z)\exp\left(Q_d e/4\pi\varepsilon_0 R_d T_e(z)\right)$ in expression (2.2.2) should be substituted with $n_0 \exp\left(e\varphi_w/T_e\right)$, as the wall potential is counted from the bulk plasma with the density n_0. Here we neglected the variation of the electron temperature near the dust surface. Therefore, the electron current to the dust particle is rewritten as

$$I_e = -\pi R_d^2 e n_o \sqrt{\frac{8T_e}{\pi m_e}} \exp\left(\frac{e\varphi_w}{T_e}\right). \tag{3.3.5}$$

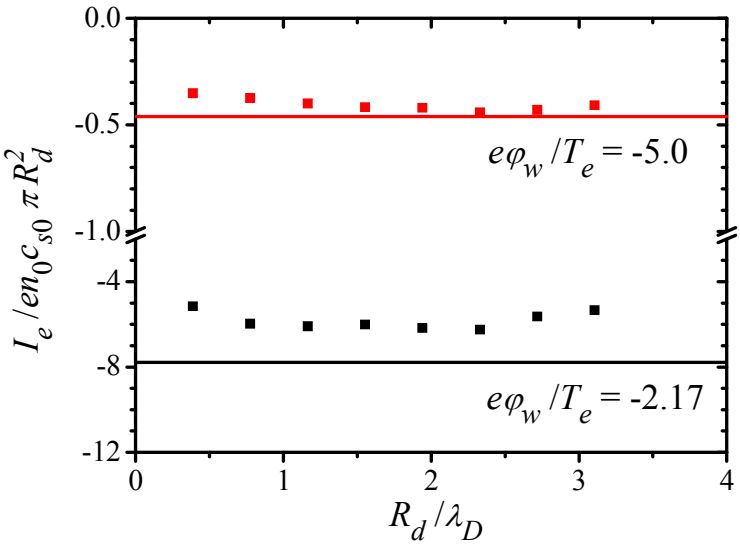

Fig. 3.3.4 *Dependence of the simulated (dots) and theoretical (lines) electron current density on the attached to the wall spherical dust particle for the two values of the wall potential* $e\varphi_w/T_e = -2.17$ *(black) and* $e\varphi_w/T_e = -5.0$ *(red).*

The electron current density corresponding to (3.3.5) is shown in Fig.3.3.4 by solid lines for the two values of the wall potential. As we can see, the modified electron current density is independent of the dust particle size and is in better agreement with the simulated electron current density for the deeper wall potential case. For the both cases of the wall potential, the simulated value of the electron current density is smaller than the theoretical one, which can be explained by the effect of the truncation of the electron velocity distribution function in the complex dust-wall geometry. The high-energy electrons absorbed by the wall are absent in the distribution function of the electron velocity normal to the dust particle surface. Thus, this component of the electron velocity, which is normally directed toward the dust surface, can not form the half-Maxwellian distribution and the electron flux to the dust reduces especially in the shadow region between the dust particle and the wall. The shallower the wall potential is, the stronger this effect is, because more electrons with lower energy will be absorbed by the wall.

If we consider the dust particle with the fixed wall potential as we did for the electron current (3.3.5), we obtain the following modified OML expression for the ion current to the dust particle on the wall

$$I_i = \pi R_d^2 \Gamma_{iz0} q_i \left(1 - \frac{2 q_i \varphi_w}{m_i u_{iz0}^2} \right), \tag{3.3.6}$$

where Γ_{iz0} and u_{iz0} are the ion particle flux and the ion flow velocity to the z direction at the point with the zero potential (left boundary), respectively. As we can see, the modified ion current density according to (3.3.6) does not depend on the dust radius in spite to the conventional OML expression (2.2.2) and the simulation results, which are shown in Fig.3.3.5 by the red line and the black dots, respectively. Surprisingly, that the unmodified OML dependence (2.2.2) is not so far from the simulated ion current density values. However, it linearly increases with the dust radius, while the simulated current density dependence on the dust radius is nonlinear and tends to saturate for large particle radii (Fig.3.3.5). To clarify this dependence let's note that the OML theory describes the motion of ions only in a field of the dust particle, while the strong electric field created by the wall is also present in the sheath. Strictly speaking, the new theory of the absorption of the plasma particles by a dust particle in an external electric field needs to be developed.

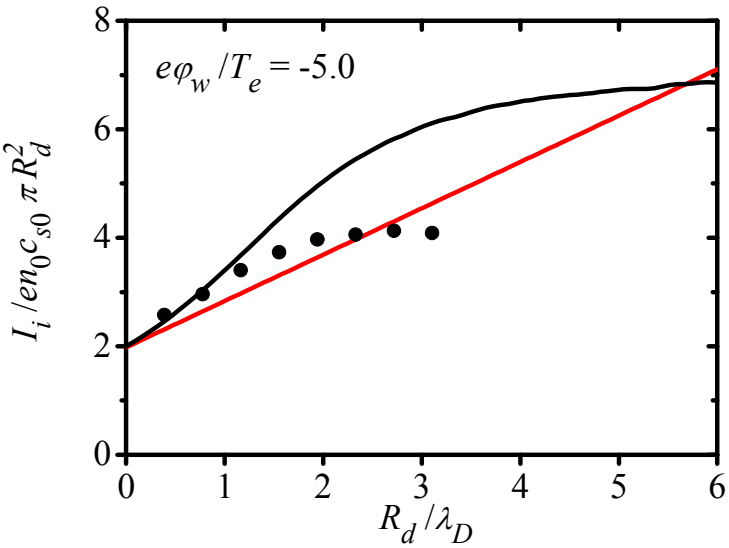

Fig. 3.3.5 *Dependencies of the ion current density to the spherical conducting dust particle placed on the plasma facing wall. Black dots represent simulation results, red line shows the dependence according to the OML theory and the black line according to the modified OML expression.*

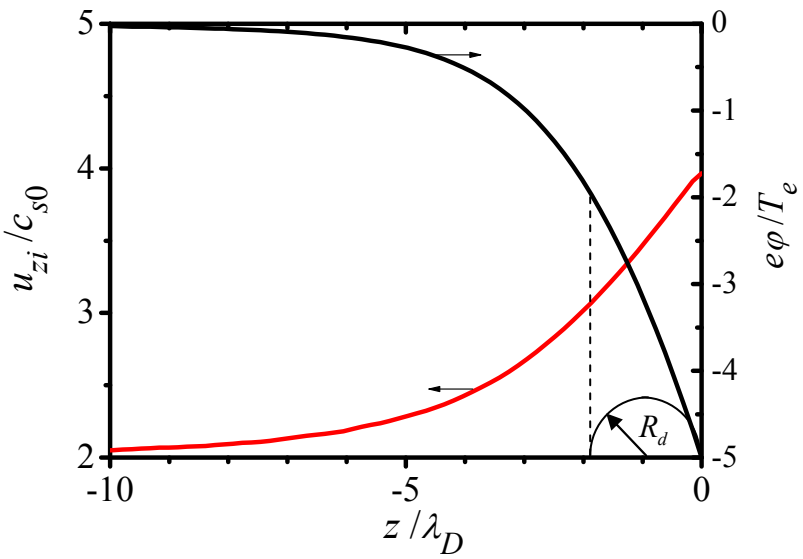

Fig. 3.3.6 *Simulated spatial profiles of the ion flow velocity and the electric potential in the undisturbed by the dust particle sheath. The dashed line shows the position, where we can roughly assume the ions start to feel the electric field created by the dust particle shown as a half-circle.*

Such theory should calculate ion trajectories in the self-consistent fields of the dust particles and the sheath, but because of the complexity of the situation we left this as one of future issues. At present, we can try to separate the both fields in the one-dimensional model and reduce the sheath field effect by excluding part of ions trajectories far from the dust particle in axial direction. As a first estimation we can assume that the ion trajectories start to feel the dust particle field at the position $-z = 2R_d$. Then, we can apply to formula (3.3.6) the local values of the ion flow velocity at the point $-z = 2R_d$ and the potential difference between this point in the undisturbed sheath and the wall as following

$$I_i = \pi R_d^2 \Gamma_{iz0} q_i \left(1 - \frac{2q_i \left[\varphi\left(z = -2R_d\right) - \varphi_w \right]}{m_i u_{iz}^2 \left(z = -2R_d\right)} \right). \tag{3.3.7}$$

The ion flux here was not changed as it conserves in the collisionless undisturbed sheath. In Fig.3.3.6, the simulated spatial profiles of the ion flow velocity and the electric potential in the sheath undisturbed by the dust particle are shown, where the selected point $-z = 2R_d$ is indicated by the dashed line. Applying the simulated values of the ion flow velocity and the potential from Fig.3.3.6 into the modified OML expression (3.3.7) we can get the dependence of the ion current density on the dust radius shown in Fig.3.3.5 by the black line. The modified OML dependence of the ion current density has good agreement with the simulation results for the smaller dust than the Debye length and shows the saturation for the big dust particles, which is not present in the conventional OML dependence (2.2.2). Nevertheless, the simulated ion current density is much smaller than that obtained from the modified OML expression (3.3.7), when the dust particle radius is bigger than the Debye length. It is reasonable to suggest that this difference comes from the self-consistent screening of the dust particle by a plasma, which is not present in the theoretical 1D approach. The dependences similar to the ion current density on the dust radius (Fig.3.3.5) can be obtained for the ion absorption drag force, because of their common nature due to the ion absorption and the similarity in the OML expressions for the current (2.2.2) and the force (2.2.9).

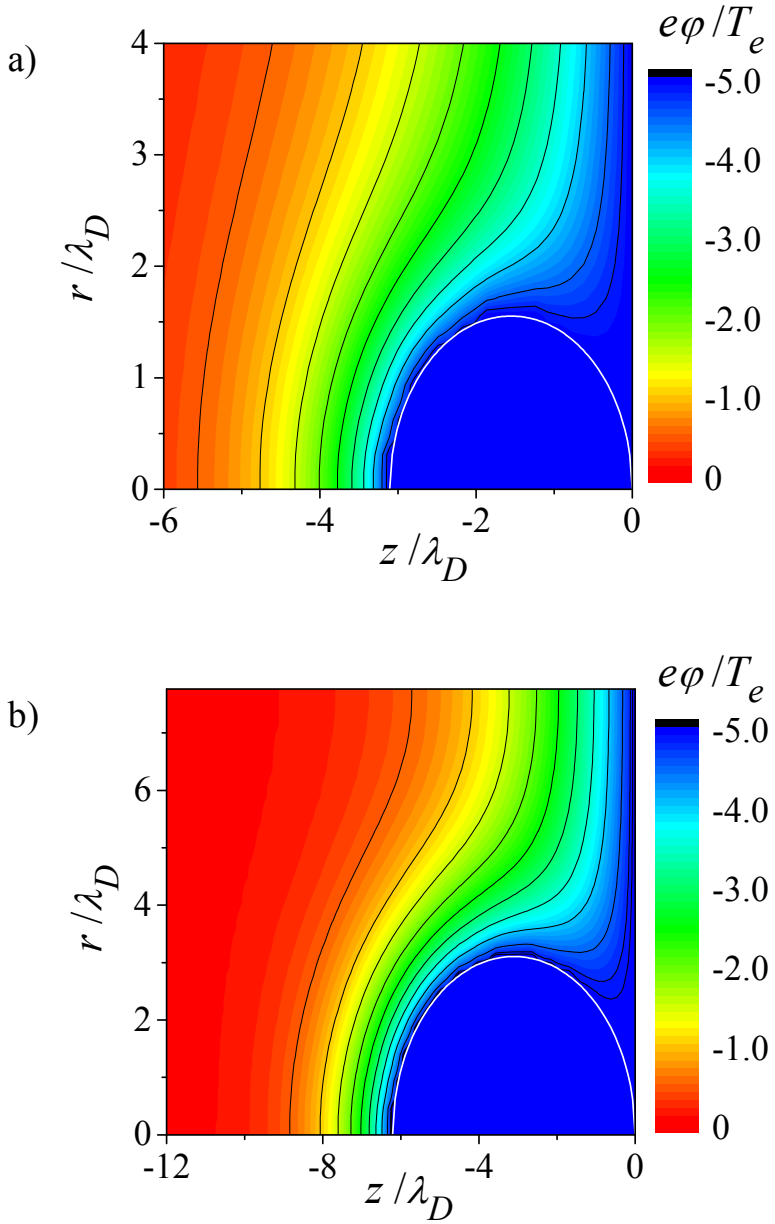

Fig. 3.3.7 *Simulated potential distributions around the dust particles of two different radii* $R_d/\lambda_D = 1.55$ *(a) and* $R_d/\lambda_D = 3.10$ *(b) on the plasma facing wall with the wall potential* $e\varphi_w/T_e = -5.0$.

Let's consider more closely the screening of the dust particle by a plasma on the plasma-facing wall. In Fig.3.3.7, the simulated spatial potential distributions around the dust particles of two different radii on the plasma-facing wall with the potential $e\varphi_w/T_e = -5.0$ are shown. The potential distribution for the particle with radius $R_d/\lambda_D = 1.55$ is shown in Fig.3.3.7(a) and for the larger dust particle with $R_d/\lambda_D = 3.10$ in Fig.3.3.7(b). In the case when the dust particle radius is $R_d/\lambda_D = 1.55$, which is larger than the Debye length, we can see the dust particle placed in the disturbed sheath potential near the wall, so we can expect that the electric field of the wall sheath affects the current to the dust particle. When the dust particle is larger with $R_d/\lambda_D = 3.10$, an individual sheath around the particle is developing and the effect of the wall sheath reduces. In this case, the ion current density to the dust particle tends to be defined by the plasma conditions at the edge of the individual dust sheath. When the dust sheath width is small in comparison with the dust radius, the ion current to the dust is limited by the dust sheath and not by the ion orbital momentum. Therefore, for the very large dust particles with $R_d \gg \lambda_D$ the ion current density is almost independent of the dust radius and saturates at the level, which can be estimated as $I_i \approx 4\pi R_d^2 e n_0 c_{s0}$ that can be seen from the simulation results in Fig.3.3.5. This level is lower than that obtained by the modified OML expression (3.3.7), because the increase of the ion absorption cross section (2.2.1) due to the orbital term in the parenthesis does not work in the sheath limited regime. The saturation of the ion current density also means the saturation of the ion flow pressure on the dust particle due to absorption. Therefore, the ion drag force acting on the very large dust particle with $R_d \gg \lambda_D$ placed on the wall can grow proportionally to $\sim R_d^2$ that is weaker than the cubic dependence obtained in the 1D theoretical model. This can contribute in the weaker dependence of the total force acting on the very large dust particle on the dust particle radius (Fig.3.3.2). We can suggest that the same mechanism can diminish the strong fourth order dependence on the dust radius of the ion drag scattering force, which was obtained in the 1D model, for the very large dust particles.

3.4 Discussion

In this chapter we described the model and the present results of the two-dimensional self-consistent simulations of the spherical conductive dust particle placed on the plasma-facing wall. The originally developed two-dimensional PIC/MC code allows us to simulate the interaction between a plasma and conductive or insulating dust particles of various shapes with different values of the dielectric constant placed at arbitrary distance from the wall including the case of the particle attached to the wall. The self-consistent simulations of the dust particle shielding and the sheath formation near the wall allow us to verify the results obtained in the one-dimensional approach, which were described in Chapter 2. In particular, we have confirmed the existence of the first critical dust radius, which is the radius of the biggest dust particle capable to leave the wall. It was shown that our 1D approach correctly describes the statics of the dust particles, which radii are smaller than the Debye length, on the plasma-facing wall. However, we found that the total force pushing the dust particles toward the wall does not increase so fast with increasing of the particles radii as the force predicted by the one-dimensional model does. It leads to larger values of the first critical dust radius than the prediction for the deeper wall potentials. The analysis of the obtained simulation results shows that the charge of the dust particles on the wall, which are bigger than the Debye length, calculated according to the 1D model is larger than the simulated one. However, the electric field non-uniformity in the sheath significantly reduces the dust charge to the smaller values than the simulated ones. The simulated dust charge is, therefore, the combination of the effect of the non-uniform electric field in the sheath and the effect of the dust shielding by a plasma. The last one causes increasing of the normal electric field at the dust surface and enhancing of the dust surface charge density. Thus, we can expect that for a smaller Debye length the charge of the dust particle with a fixed radius at the wall with a fixed potential is larger than that for a longer Debye length and, correspondingly, the electric force is stronger. Nevertheless, to explain the reduction of the total force acting on the dust particle toward the wall for the large dust radii we need to consider the ion drag force dependence on the dust size. We have shown that the ion current density and, correspondingly, the ion absorption drag pressure acting on the much bigger dust particle than the Debye length tends to saturate due to developing of the sheath limited current regime. For the dust particles,

which radii are not so large but still larger than the Debye length, we proposed the modified OML expressions for the electron and ion currents to the dust particle attached to the wall accounting the fixed dust potential and the acceleration of ions in the sheath. The more precise absorption theory for the dust particle in the sheath can be developed basing on the calculation of ion trajectories in the sheath potential disturbed by the dust particle. The non-self-consistent consideration without the plasma screening effect, which takes into account the induced field calculation around the conductive dust particle at the wall (Appendix C) can be useful and is our future issue. The reduction of the ion absorption drag pressure can contribute to the explanation of the first critical dust radius increasing. Nevertheless, the contribution of the ion drag scattering force is also important and can be studied further. One of the possible issues affecting dependence of the ion scattering drag force on the dust radius is the corresponding dependence of the dust Coulomb logarithm. Another issue is defining itself of the ion scattering drag force on the dust particle in the sheath. In spite of the classical consideration, ions are absorbed by the wall and have no decelerating part of their trajectories around the dust particle. We can consider this effect from the electrostatic point of view. In an unlimited uniform plasma flow, the wake potential is created behind the dust particle along the flow. The electrostatic interaction of the charged dust particle with the wake field can be considered as the scattering force acting on the dust particle. Thus, the scattering force is the interaction of the dust particle with a plasma. However, in the sheath even without a dust particle the plasma is positively charged and can attract the negatively charged dust particle to the direction from the wall. Thus, not all electrostatic interactions of the dust particle with a plasma can be considered causing the scattering force. Only the interaction with the plasma disturbance introduced by the dust particle presence can be attributed to the scattering, other part of the electrostatic dust-plasma interaction should be attributed to the usual electric force due to the sheath electric field. As we saw from the 2D simulations, the large positive charge is created near the upstream point of the dust surface, which is opposite to the conventional wake field. Therefore, the direction and the value of the scattering force acting on the dust particle at the wall needs additional studies. As well as the ion absorption by the dust particle in the disturbed sheath, the scattering process can be also considered for the theory development. As a next issue we also consider the self-consistent simulations of the dust particles with different shapes apart from the wall. That can clarify the self-consistent dust dynamics in the sheath.

Chapter 4

Summary

In the present work we investigated the statics and dynamics of the spherical dust particle on the electrically biased plasma-facing wall and in the boundary plasma near it using the one-dimensional theoretical approach with simulated plasma parameters distributions as well as the two-dimensional self-consistent simulations. The used theoretical one-dimensional model describes the behavior of the dust particle in the boundary plasma assuming that the particle does not disturb the plasma parameters distributions significantly that can be correct for the smaller dust radii than the Debye length. The spatial profiles of the plasma parameters in the sheath and the presheath were simulated using our own developed 1D PIC/MC code. The charging of the dust particle in a plasma is described according to the Orbital Motion Limited theory [41,42], which gives the absorption cross sections of electrons and ions by the dust particle. The ion absorption cross section is also used for calculations of the ion absorption drag force. Other forces acting on the dust particle taken into account are the electric force due to the sheath electric field, the electrostatic image force due to the interaction of the dust with the induced charges on the wall, the ion scattering drag force due to the deflection of ion trajectories by the dust and the gravitational force. Except the electrostatic and arbitrary directed gravitational forces all others are pushing the dust particle toward the wall. The balance of the pushing and repulsive forces, which defines the conditions when the dust particle can leave the wall and start the motion toward the plasma, was analyzed. The charging of conductive dust particle on the wall physically differs from the charging in the plasma, because in this case not the currents but the component of the electric field normal to the surface defines the dust charge. Taking into account the dependencies of the charge and the forces on the dust particle radius, we have predicted the existence of the first critical dust radius, which defines the largest particle able to release from the wall. The dependencies of the first critical dust radius on the wall potential, the form factor of the dust particle, the plasma parameters and the gravity conditions were analytically obtained for the

simple Bohm sheath model [24]. For the case without the gravitational force, it was shown that there is the threshold sheath potential drop, so that in the shallower than this sheath potential dust particles of any size can not leave the wall. For the deeper than the threshold sheath potential the first critical dust radius is the increasing function of the potential drop. Accounting the possibility to control the sheath potential drop with the externally applied voltage, one can also control the size of the dust particles released from the wall or even suppress releasing of particles with any size. It was shown that the gravitational force directed toward the wall does not affect the threshold potential and reduces the values of the first critical dust radius. In the case of the gravitational force acting from the wall direction, the threshold potential remains unchanged, but releasing of the dust particles for the shallower potentials becomes possible with the gravity assistance. Depending on the value of the gravitational parameter, which describes the relative strength of the gravitational force in respect to the ion flow pressure, there could be a range of the sheath potentials, where releasing of the dust from the wall is still suppressed. Practically it can be used for collection of dust particles on some electrodes and prevention of their spreading in a plasma, especially for dense plasma conditions when the role of the gravitational force is not important. Such collectors could be installed in the divertor region of fusion devices, where the dust probably produced and where the biased electrode minimally affects the confinement conditions.

Furthermore we analyzed possible trajectories of the released dust particles with various radii and masses in the normal to the wall direction using our one-dimensional model. The trajectories were calculated using simultaneous solutions of the dust charging and motion equations with the simulated profiles of the plasma parameters in the boundary plasma. It was shown that there is the second critical radius for the heavy dust particles, which discriminates their large and small amplitude trajectories. The large amplitude dust oscillatory trajectories are possible in the well like effective potential profiles with the minimum corresponding to the equilibrium position. The smaller the dust particle is, the larger the oscillation amplitude becomes. The short trajectories are performed by dust particles in the force field pushing it toward the wall, which corresponds to the effective potential profile decreasing near the wall. Such dust particles return to the wall immediately after releasing due to the fast recharging process switching the direction of the total force acting on the released particle in a plasma. The existence of the second critical radius

was explained by appearance of the effective potential barrier separating the wall from the dust equilibrium position, which the particle with the zero initial velocity can not reach. For the dust particle with the radius equal to the second critical one the barrier just appears at the wall position. It was shown that without the gravitational force the maximum of the effective potential corresponding to the barrier appears in the sheaths with the deeper sheath potential drop than $4.23T_e/e$ and does not appear in the shallower sheaths than $2.84T_e/e$ for the Bohm sheath model. For the intermediate sheath potentials the second critical radius exists and has the maximum value corresponding to the critical dust levitation radius found by Vladimirov [60]. The sharp discrimination of the motion amplitudes on the dust particle radii disappears for the dust particles lighter than the critical mass due to the delayed charging effect, when the charge of the dust particle initially attached to the wall slowly relaxes in a plasma to the local equilibrium charge in comparison with the oscillation period. The delayed charging effect also leads to the collisionless damping of the large amplitude oscillations due to the mechanism described in [63]. The effect of gravity on the effective potential barrier and the equilibrium positions was examined. It was shown that the levitation of dust particles may be possible near a wall in an upper horizontal position with the shallow sheath potential. The combined diagrams of the equilibrium and the critical dust radii plotted in the sheath potential space show the scenario of the dust particle behavior initially placed on the wall for any selected wall potential, dust radius and the given gravitational conditions. Such diagrams allow us to analyze which dust particles can leave the wall and go far into the plasma that can be helpful for understanding of the plasma contamination.

The power balance of the carbon dust particle in a plasma was analyzed allowing to estimate the internal particle temperature and the corresponding dwell time for different plasma conditions. It was shown that for the present and future divertor plasma parameters a micrometer size dust particle can have a temperature of a few thousands kelvins and survive long enough time, from hours to tens of milliseconds, to move on significant distances with the typical speed of a m/s order. It was shown that the main mechanisms leading to the carbon dust destruction in divertor plasma are likely the thermal evaporation and the radiation enhanced sublimation, while the chemical sputtering plays role only for relatively low dust temperatures. Some of these results were published in [11] and support the idea that

the dust particles can penetrate into the edge plasma of fusion devices and contribute to the impurity contamination. The role of the ion diamagnetic drift in the magnetized sheath and the roughness of the wall surface for the dust particle acceleration was recognized in [11].

In order to evaluate the results obtained from the one-dimensional consideration and analyze the behavior of the bigger dust particle than the Debye length in sheaths, we developed the new two-dimensional PIC/MC code for the cylindrically symmetric system. The code allows simulating of the self-consistent sheath formation with the conductive or insulating immobile dust particle of various axially symmetric shapes, sizes and values of the dielectric constant, which can be placed at arbitrary position in front of the electrically biased wall including the case of a dust particle attached to the wall. Some non-standard features of the code concerning boundary conditions, the field solver and the motion advancing scheme are described in Section 3.2. The results of the simulations of the total force acting on the conductive spherical dust particles on the plasma-facing wall confirm the existence of the first critical dust radius. The simulated total force reasonably agrees with the theoretical prediction calculated according to the one-dimensional model for the dust particles which radii are smaller than the Debye length that validates the first critical radius estimations for the shallow wall potentials. For the bigger dust particles than the Debye length the simulated total force is much weaker than that predicted by the one-dimensional model. It leads to the bigger values of the first critical dust radius for deep sheath potential drops than ones expected from the theoretical consideration. The analysis of the self-consistent charging and screening of the big dust particle suggests that, the most likely, this effect is attributed to the theoretical overestimation of the ion drag force, especially its scattering component, rather than the underestimation of the repulsive electric force. The comparison of the simulated dust charge with the induced charge on the dust particle in the non-uniform sheath electric field shows that the latter one is smaller than the former one for big dust radii due to the self-consistent screening of the dust particle by a plasma, which enhances the field on the dust surface and the corresponding induced surface charge density. The analysis of the ion current density on the dust particle shows its nonlinear dependence on the particle radius in spite to the OML prediction, which takes into account a fixed potential of the dust particle attached to the wall. We suggest that there are two reasons responsible for the observed dependence. The first one is the superposition of

the sheath electric field with the one created by the dust particle, which leads, in the rough approximation, to the dependence of the impact ion kinetic and potential energy on the dust particle size. The second effect is transition of the ion current regime from the orbital to the sheath limited for the dust particles, which size is much larger than the Debye length. In the sheath limited regime the ion current density on the dust particle tends to saturate. Together with the ion current density also the ion flow pressure on the dust particle saturates that contributes to the weakening of the total force pushing the particle toward the wall. The ion scattering by the dust at the wall position substantially differs from the usual scattering of ions by the dust particle in the ion flow. The simulations of the dust particle screening near the wall showed that the excess of positive charge is formed near the upstream point of the dust surface, because of absence of the decelerating part of the ion trajectories due to the absorption by the wall. This can cause the significant effect on the ion scattering drag force including the change of its direction. Regarding this, additional theoretical and simulation studies of the ion scattering by a dust near the wall are needed. The obtained results of the self-consistent screening of dust particles that are bigger than the Debye length in the sheath show the main effects, which should be taken into account in future theoretical descriptions. As the next step of our researches we also consider obtaining of the self-consistent effective potential profiles for the big dust particles in the boundary plasma that should clarify the self-consistent dust dynamics. This study can be useful for developing of the more rigorous theoretical estimations of the self-consistent currents and forces acting on the big dust particle that can be applied for integrated simulations of dust dynamics in a SOL (Scrape-Off-Layer) plasma in fusion devices. The theory also should take into account effects of a magnetic field and a possible electron emission from the dust in future. Further refining of the consideration of the dust particle releasing from the wall can include the contact potential difference between the wall and the dust particle of different material. This also can be considered as the electrostatic approach for accounting of the molecular bounding forces between the wall and the dust particle. In the conclusion we would like to say that the present work includes the first theoretical consideration of the dust releasing from the plasma-facing wall and the first self-consistent simulations of the dust particles screening in the sheath.

Appendix A

Local macroscopic quantities in collisionless boundary plasma

Let's consider the one-dimensional model, in which the plasma particles with the half-Maxwellian distribution functions are injected from the bulk plasma boundary ($z = -L_s$) toward the perfectly absorbing wall ($z = 0$), which has the given potential φ_w (Fig.2.1.1). In this analysis we consider the formation of the collisionless sheath potential, which monotonically decreases toward the wall. The potential at the injection boundary of plasma particles is set to zero. Because there are no particle sources and sinks in the system, the local energy distribution functions of the plasma particles, $f_j\left(z, \varepsilon_{jz}\right)$ (here j = e, i), are the same at any point as at the injection boundary $f_j\left(z = 0, \varepsilon_{jz}\right)$. Here $\varepsilon_{jz} = m_j \upsilon_z^2 / 2 + q_j \varphi\left(z\right)$ is the total particle energy in the electrostatic potential $\varphi\left(z\right)$. The local macroscopic quantities inside the system can be easily calculated using the local energy distribution function. Electrons have positive and negative velocities due to reflection by the monotonically decreasing potential. The local electron density with positive velocities can be calculated as

$$n_e^{(+)}\left(z\right) = \frac{1}{\sqrt{2m_e}} \int_{-e\varphi(z)}^{\infty} d\varepsilon_{ez} \frac{f_{e0}^{(+)}\left(\varepsilon_{ez}\right)}{\sqrt{\varepsilon_{ez} + e\varphi\left(z\right)}} = n_{e0}^{(+)} \exp\left[e\varphi\left(z\right)/T_e\right], \tag{A.1}$$

and with negative velocities as

$$n_e^{(-)}\left(z\right) = \frac{1}{\sqrt{2m_e}} \int_{-e\varphi(z)}^{-e\varphi_w} d\varepsilon_{ez} \frac{f_{e0}^{(+)}\left(\varepsilon_{ez}\right)}{\sqrt{\varepsilon_{ez} + e\varphi\left(z\right)}} = n_{e0}^{(+)} \exp\left[\frac{e\varphi\left(z\right)}{T_e}\right] \operatorname{erf}\left(\sqrt{\frac{e\left[\varphi(z) - \varphi_w\right]}{T_e}}\right). \tag{A.2}$$

Here $f_{e0}^{(+)}\left(\varepsilon_{ez}\right)$ is the electron energy distribution function (2.1.5) and $n_{e0}^{(+)}$ is the density of electrons with positive velocities at the injection boundary and

$\operatorname{erf} x = \frac{2}{\sqrt{\pi}} \int_0^x e^{-t^2} dt$ is the error function.

The total local density of electrons with positive and negative velocities is then expressed as

$$n_e(z) = n_e^{(+)}(z) + n_e^{(-)}(z) = n_{e0}^{(+)} \exp\left[e\varphi(z)/T_e\right] \left\{1 + \operatorname{erf}\left(\sqrt{e\left[\varphi(z) - \varphi_w\right]/T_e}\right)\right\}. \quad \text{(A.3)}$$

The second term of the electron density in (A.3) comes from the fact that the electron distribution function is truncated at negative velocities. One can easily obtain the total electron density at the sheath entrance $z = 0$, where $\varphi = 0$

$$n_e(0) = n_{e0}^{(+)} \left[1 + \operatorname{erf}\left(\sqrt{-e\varphi_w/T_e}\right)\right] \quad \text{(A.4)}$$

As ions have only positive velocities in the monotonically decreasing potential, the local ion density is obtained as following

$$n_i(z) = n_i^{(+)}(z) = \frac{1}{\sqrt{2m_i}} \int_0^\infty d\varepsilon_{iz} \frac{f_{i0}^{(+)}(\varepsilon_{iz})}{\sqrt{\varepsilon_{iz} - q_i\varphi(z)}} = n_{i0}^{(+)} \exp\left[-q_i\varphi(z)/T_i\right] \operatorname{erfc}\left(\sqrt{\frac{-q_i\varphi(z)}{T_i}}\right), \quad \text{(A.5)}$$

where $f_{i0}^{(+)}(\varepsilon_{iz})$ is the ion energy distribution function and $n_{e0}^{(+)}$ is the ion density at the injection boundary and $\operatorname{erfc} x = 1 - \operatorname{erf} x$ is the complementary error function. The flux of electrons with positive velocities is

$$\Gamma_{ez}^{(+)}(z) = \frac{1}{m_e} \int_{-e\varphi(z)}^{\infty} d\varepsilon_{ez} f_{e0}^{(+)}(\varepsilon_{ez}) = n_{e0}^{(+)} \sqrt{\frac{2T_e}{\pi m_e}} \exp\left[e\varphi(z)/T_e\right], \quad \text{(A.6)}$$

and with negative velocities is

$$\Gamma_e^{(-)}(z) = -\frac{1}{m_e} \int_{-e\varphi(z)}^{-e\varphi_w} d\varepsilon_{ez} f_{e0}^{(+)}(\varepsilon_{ez})$$

$$= -n_{e0}^{(+)} \sqrt{\frac{2T_e}{\pi m_e}} \exp\left[e\varphi(z)/T\right] \left[1 - \exp\left\{-e\left[\varphi(z) - \varphi_w\right]/T_e\right\}\right]. \quad \text{(A.7)}$$

The sum of these fluxes gives us the uniform total electron flux

$$\Gamma_e = \Gamma_e^{(+)}(z) + \Gamma_e^{(-)}(z) = n_{e0}^{(+)} \sqrt{\frac{2T_e}{\pi m_e}} \exp\left(e\varphi_w/T_e\right). \quad \text{(A.8)}$$

The flux of ions, all of which have positive velocities, is obtained as

$$\Gamma_i(z) = \Gamma_i^{(+)}(z) = \frac{1}{m_i} \int_0^\infty d\varepsilon_{iz} f_{i0}^{(+)}(\varepsilon_{iz}) = n_{i0}^{(+)} \sqrt{\frac{2T_i}{\pi m_i}}. \quad \text{(A.9)}$$

These macroscopic quantities give us the local flow velocities of electrons and ions

$$u_{ez}(z) = \frac{\Gamma_e^{(+)}(z) + \Gamma_e^{(-)}(z)}{n_e^{(+)}(z) + n_e^{(-)}(z)} = \sqrt{\frac{2T_e}{\pi m_e}} \frac{\exp[-e(\varphi(z) - \varphi_w)/T_e]}{1 + \mathrm{erf}\,[\sqrt{e(\varphi(z) - \varphi_w)/T_e}\,]}, \tag{A.10}$$

and

$$u_{iz}(z) = \frac{\Gamma_i^{(+)}(z)}{n_i^{(+)}(z)} = \frac{\sqrt{2T_i / \pi m_i}}{\exp(-q_i \varphi(z)/T_i)\,\mathrm{erfc}(\sqrt{-q_i \varphi(z)/T_i})}. \tag{A.11}$$

The potential φ_w of the floating wall is determined by equality of the electron and ion fluxes to the wall and can be found as following

$$\varphi_w = -\frac{T_e}{2e} \ln\left[\left(\frac{n_{e0}^{(+)}}{n_{i0}^{(+)}}\right)^2 \frac{m_i}{m_e} \frac{T_e}{T_i}\right]. \tag{A.12}$$

Appendix B

Sheath potential drop and externally applied voltage

In order to obtain the relation between the externally applied voltage φ_{ext} and the sheath potential drop φ_{sh}, the simple one-dimensional model is used (Fig.B.1). We consider the plasma between the wall $w1$ and the wall $w2$ with the externally applied voltage φ_{ext} to the walls. The areas of the wall $w1$ and the wall $w2$ are S^{w1} and S^{w2}, respectively.

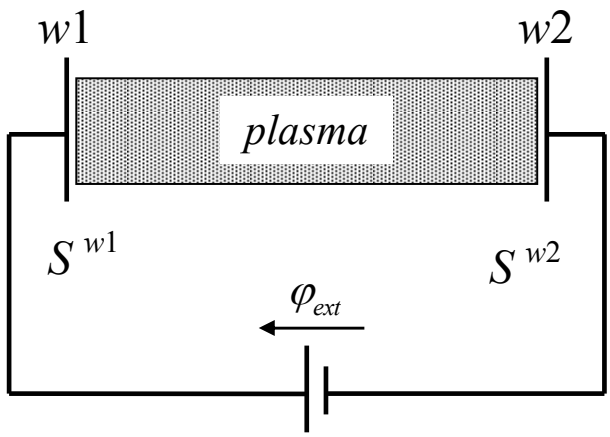

Fig. B.1 *One-dimensional model for calculation of the relation between the externally applied voltage* φ_{ext} *and the sheath potential drop* φ_{sh}.

The Debye sheaths are formed in front of each wall, where a plasma is assumed collisionless, so that the particle fluxes conserve. In this model we do not take into account the presheath potential drop and assume the same quasi-neutral plasma conditions at the edges of both sheaths. Also, we consider only the positively charged sheaths. The ions at a sheath edge are assumed monoenergetic with the velocity u_{ise} directed toward a wall satisfying the Bohm criterion. The ion flux to the wall is then

$$\Gamma_i = n_i(z)u_{iz}(z) = n_{ise}u_{ise}. \tag{B.1}$$

Here n_{ise} and u_{ise} are the ion density and the ion flow velocity at the sheath entrance, respectively. The electron velocity distribution function at the sheath edge is truncated due to absorption of high-energy electrons by the wall (see Appendix A), so the electron flux in the sheath is expressed via the electron density at the sheath edge n_{ese} as following

$$\Gamma_e = n_{ese}\sqrt{\frac{2T_e}{\pi m_e}}\frac{\exp\left(-e\varphi_{sh}/T_e\right)}{1+\mathrm{erf}\left(\sqrt{e\varphi_{sh}/T_e}\right)}. \tag{B.2}$$

The current conservation in this circuit (Fig.B.1) gives us the following relation

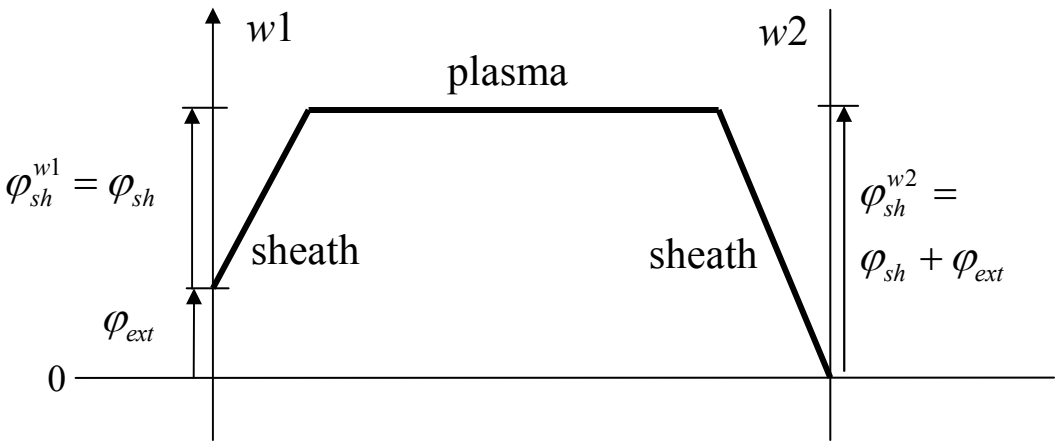

Fig. B.2 *Sketch of potential profile between two walls w1 and w2. Here the external voltage is applied to the wall w1 with the positive polarity and the potential is referred from the wall w2.*

$$S^{w1}\Gamma_e^{w1} + S^{w2}\Gamma_e^{w2} = Z_i\left(S^{w1}\Gamma_i^{w1} + S^{w2}\Gamma_i^{w2}\right). \tag{B.3}$$

Here $Z_i = q_i/e$ is the ion charge number, Γ_e^{w1} and Γ_e^{w2} are the electron fluxes to the walls $w1$ and $w2$, respectively. According to (B.2) we have

$$\Gamma_e^{w1} = n_{ese}\sqrt{\frac{2T_e}{\pi m_e}}\frac{\exp\left(-e\varphi_{sh}/T_e\right)}{1+\mathrm{erf}\left(\sqrt{e\varphi_{sh}/T_e}\right)}, \tag{B.4}$$

$$\Gamma_e^{w2} = n_{ese}\sqrt{\frac{2T_e}{\pi m_e}}\frac{\exp\left[\left(-e\varphi_{sh}+\varphi_{ext}\right)/T_e\right]}{1+\mathrm{erf}\left[\sqrt{\left(e\varphi_{sh}+\varphi_{ext}\right)/T_e}\right]}. \tag{B.5}$$

The ion fluxes to the walls $w1$ and $w2$, Γ_i^{w1} and Γ_i^{w2}, respectively, are equal each other due to the same sheath edge conditions

$$\Gamma_i^{w1} = \Gamma_i^{w2} = n_{ise}u_{ise}. \tag{B.6}$$

Substituting these expressions into the current conservation equation (B.3), we find the relation between the externally applied voltage φ_{ext} and the sheath potential drop φ_{sh}

$$\frac{\exp\left(-e\varphi_{sh}/T_e\right)}{1+\operatorname{erf}\left(\sqrt{e\varphi_{sh}/T_e}\right)}\frac{S^{w1}}{S^{w2}}+\frac{\exp\left[-(e\varphi_{sh}+\varphi_{ext})/T_e\right]}{1+\operatorname{erf}\left[\sqrt{(e\varphi_{sh}+\varphi_{ext})/T_e}\right]}=\frac{u_{ise}}{\sqrt{2T_e/\pi m_e}}\left(1+\frac{S^{w1}}{S^{w2}}\right). \tag{B.7}$$

Here the charge neutrality condition at the sheath edges $n_{ese}=Z_i n_{ise}$ is used. According to the Bohm criterion, the ion flow velocity at the sheath entrance equals to the ion sound speed $u_{ise}=\sqrt{T_e/m_i}$, thus the relation (B.7) can be rewritten as

$$\frac{\exp\left(-e\varphi_{sh}/T_e\right)}{1+\operatorname{erf}\left(\sqrt{e\varphi_{sh}/T_e}\right)}\frac{S^{w1}}{S^{w2}}+\frac{\exp\left[-(e\varphi_{sh}+\varphi_{ext})/T_e\right]}{1+\operatorname{erf}\left[\sqrt{e\varphi_{sh}+\varphi_{ext})/T_e}\right]}=\sqrt{\frac{\pi}{2}\frac{m_e}{m_i}}\left(1+\frac{S^{w1}}{S^{w2}}\right). \tag{B.8}$$

Without the externally applied voltage, $\varphi_{ext}=0$, the sheath potential drop corresponds to the floating walls case

$$\frac{\exp\left(-e\varphi_{sf}/T_e\right)}{1+\operatorname{erf}\left(\sqrt{e\varphi_{sf}/T_e}\right)}=\sqrt{\frac{\pi}{2}\frac{m_e}{m_i}}. \tag{B.9}$$

Here φ_{sf} is the potential drop in the sheath near the floating wall. As this potential drop is determined by the equality of the electron and ion fluxes, it does not depend on the areas of the walls. In the case of a deep sheath potential, the effect of the truncation of electron velocity distribution function is negligible, $\operatorname{erf}\left(\sqrt{e\varphi_{sf}/T_e}\right)\to 1$. So, the well known floating sheath potential drop is obtained

$$\frac{e\varphi_{sf}}{T_e}=-\frac{1}{2}\ln\left(2\pi\frac{m_e}{m_i}\right). \tag{B.10}$$

On the other hand, in the case of large applied voltage, $e\varphi_{ext}/T_e\gg 1$, the second term in LHS of equation (B.8), which corresponds to the electron current to the wall $w2$, can be neglected

$$\frac{\exp\left(-e\varphi_{sh}/T_e\right)}{1+\operatorname{erf}\left(\sqrt{e\varphi_{sh}/T_e}\right)}=\sqrt{\frac{\pi}{2}\frac{m_e}{m_i}}\frac{S^{w1}+S^{w2}}{S^{w1}}. \tag{B.11}$$

In this case, for $S^{w2}\ll S^{w1}$ the sheath potential drop near the wall $w1$, φ_{sh}, approaches the floating potential φ_{sf} (B.9). The dependences of the sheath potential

drops near the walls $w1$ and $w2$ are shown in Fig.B.3 for the hydrogen plasma and the two values of the ratio S^{w1}/S^{w2}=0.1 and 10.0. For this case the floating sheath potential drop is $\varphi_{sf} = 2.847\,T_e/e$. Due to symmetry of the model, the value φ_{sh}^{w2} can be considered as the sheath potential drop φ_{sh} for the negative polarity of the externally applied voltage to the wall $w1$.

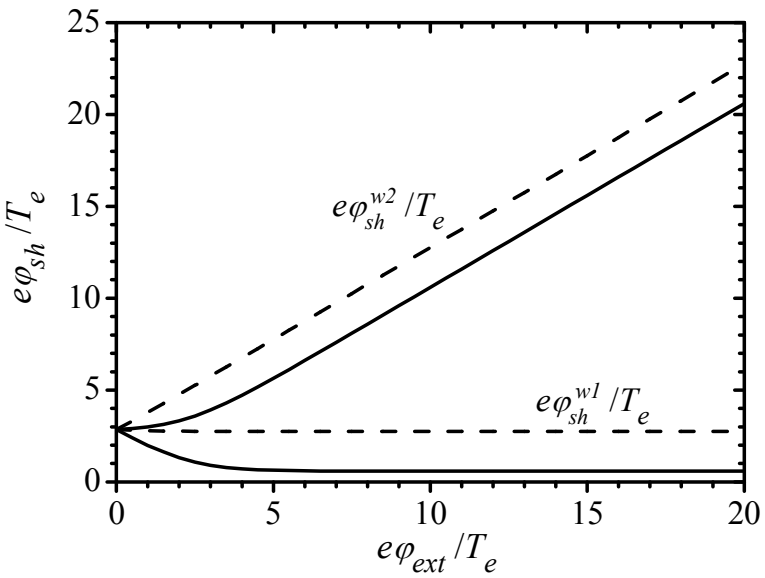

Fig. B.3 *Sheath potential drops near the walls* $w1$ *and* $w2$ *as functions of the externally applied voltage. The solid lines correspond to the area ratio* $S^{w1}/S^{w2} = 0.1$ *and the dashed lines to* $S^{w1}/S^{w2} = 10$.

As we can see, for the large value of the ratio S^{w1}/S^{w2}, the sheath potential drop near the wall $w1$ is almost independent of the external voltage. In this case, we can not get shallow sheath potential drops. On the other hand, in case of the small value of the area ratio, the sheath potential drop is widely controlled by the externally applied voltage.

Appendix C

Electrostatic potential due to induced charge of spherical dust in non-uniform electric field

The induced charge on the spherical dust particle immersed in non-uniform electric field is described here theoretically. The spherical conductive dust particle with the radius R_d is attached to the infinitely extended conductive wall with externally applied non-uniform electric field (Fig.C.1).

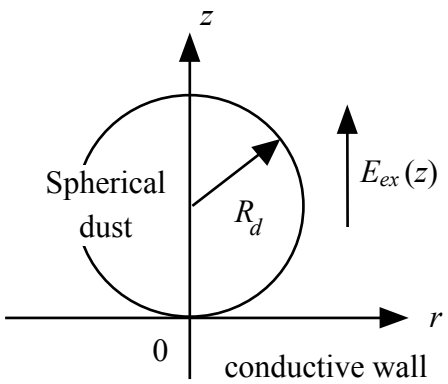

Fig. C.1 *Sketch of a conductive spherical dust particle with the radius* R_d *on a conductive wall in cylindrical coordinates* (r,z). *Non-uniform electric field is applied externally.*

The local electrostatic potential is a superposition of the external non-uniform potential $\varphi_{ex}(z)$ and the potential created by the induced charge of the dust particle $\varphi_{in}(r,z)$

$$\varphi(r,z) = \varphi_{ex}(z) + \varphi_{in}(r,z). \tag{C.1}$$

The external potential can be approximated by the polynomial of the axial coordinate z

$$\varphi_{ex}(z) = \sum_{k=0}^{k_{\max}} h_k z^k \,, \tag{C.2}$$

where the coefficient h_0 corresponds to the wall potential at $z = 0$

$$h_0 = \varphi_w \,. \tag{C.3}$$

This means that the induced potential at the wall is vanishing

$$\varphi_{in}(r, z = 0) = 0 \,. \tag{C.4}$$

The induced potential should satisfy the Laplace equation

$$\frac{1}{r}\frac{\partial}{\partial r}\left(r \frac{\partial \varphi_{in}}{\partial r} \right) + \frac{\partial^2 \varphi_{in}}{\partial z^2} = 0 \,. \tag{C.5}$$

In order to obtain the potential in the cylindrically symmetric configuration, the bipolar coordinates (α, β) are introduced

$$z + i\,r = \frac{i\,R_d}{\alpha + i\,\beta} \,, \tag{C.6}$$

where i is the imaginary unit.

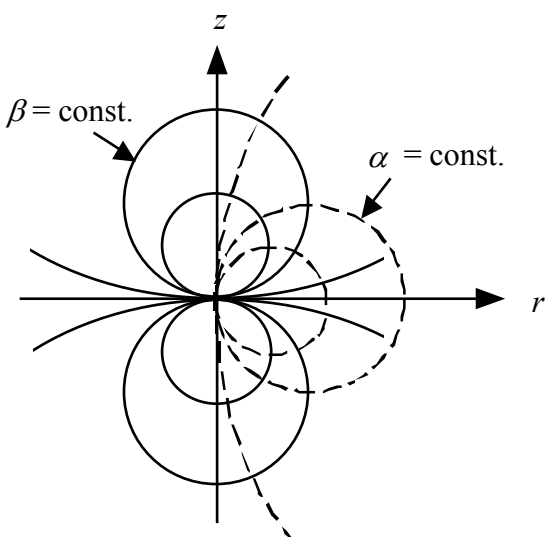

Fig. C.2 *Constant lines of the bipolar coordinates α and β in (r, z) space. The spherical dust particle surface and the wall surface correspond to $\beta = \beta_0 = 1/2$ and $\beta = 0$, respectively.*

The relations between the coordinates (r,z) and (α,β) are following

$$\begin{cases} r = R_d\,\alpha/\left(\alpha^2+\beta^2\right) \\ z = R_d\,\beta/\left(\alpha^2+\beta^2\right) \end{cases} \quad \text{and} \quad \begin{cases} \alpha = R_d\,r/\left(r^2+z^2\right) \\ \beta = R_d\,z/\left(r^2+z^2\right) \end{cases}, \tag{C.7}$$

where $0 \le \alpha \le \infty$ and $-\infty \le \beta \le \infty$. The introduced coordinates α and β are orthogonal with the lines of constant α and β in (r,z) space shown in Fig.C.2. The dust surface and the wall surface $(z=0)$ correspond to $\beta = 1/2 = \beta_0$ and $\beta = 0$, respectively.

The Laplace equation (C.5) in the (α,β) coordinates has the form

$$\left(\frac{\partial}{\partial\alpha}\frac{\alpha}{\alpha^2+\beta^2}\frac{\partial}{\partial\alpha}+\frac{\partial}{\partial\beta}\frac{\alpha}{\alpha^2+\beta^2}\frac{\partial}{\partial\beta}\right)\varphi_{in} = 0. \tag{C.8}$$

The general solution of this equation is given by

$$\varphi_{in}(\alpha,\beta) = \sqrt{\alpha^2+\beta^2}\int_0^\infty d\lambda\, C(\lambda)\frac{\sinh(\beta\lambda)}{\sinh(\beta_0\lambda)}J_0(\alpha\lambda). \tag{C.9}$$

Note that the induced potential satisfies the condition (C.3) on the wall surface, where $z=\beta=0$. The unknown coefficient $C(\lambda)$ is determined by the boundary condition on the dust surface. Here, this coefficient is expanded by the series of the parameter λ

$$C(\lambda) = e^{-\beta_0\lambda}\sum_{n=1}^{\infty} c_n\lambda^n\ . \tag{C.10}$$

This gives us the series expression of the induced potential

$$\varphi_{in}(\alpha,\beta) = \sqrt{\alpha^2+\beta^2}\sum_{n=1}^{\infty} c_n I_{\lambda n}(\alpha,\beta), \tag{C.11}$$

where the function $I_{\lambda n}(\alpha,\beta)$ is defined as

$$I_{\lambda n}(\alpha,\beta) \equiv \int_0^\infty d\lambda\,\lambda^n e^{-\beta_0\lambda}\frac{\sinh(\beta\lambda)}{\sinh(\beta_0\lambda)}J_0(\alpha\lambda). \tag{C.12}$$

The external potential (C.2) in the (α,β) space is expressed as following

$$\varphi_{ex}(\alpha,\beta) = \sum_{k=0}^{k_{\max}} h_k\left(\frac{R_d\beta}{\alpha^2+\beta^2}\right)^k\ . \tag{C.13}$$

Further, we express the term $\left[\beta/\left(\alpha^2+\beta^2\right)\right]^k$ in the expansion (C.13) using the function $I_n\left(\alpha,\beta\right)$, which is defined as

$$I_n\left(\alpha,\beta\right)\equiv\int_0^\infty d\lambda\,\lambda^n e^{-\beta\lambda}J_0\left(\alpha\lambda\right)=\left(-1\right)^n\frac{d^n}{d\beta^n}\frac{1}{\sqrt{\alpha^2+\beta^2}}. \tag{C.14}$$

This relation leads to

$$\frac{\beta}{\alpha^2+\beta^2}=\sqrt{\alpha^2+\beta^2}\,I_1\left(\alpha,\beta\right), \tag{C.15.1}$$

$$\left(\frac{\beta}{\alpha^2+\beta^2}\right)^2=\frac{\sqrt{\alpha^2+\beta^2}}{3\beta}I_1\left(\alpha,\beta\right)+\frac{\sqrt{\alpha^2+\beta^2}}{3}I_2\left(\alpha,\beta\right), \tag{C.15.2}$$

$$\left(\frac{\beta}{\alpha^2+\beta^2}\right)^3=\frac{\sqrt{\alpha^2+\beta^2}}{5\beta^2}I_1\left(\alpha,\beta\right)+\frac{\sqrt{\alpha^2+\beta^2}}{5\beta}I_2\left(\alpha,\beta\right)+\frac{\sqrt{\alpha^2+\beta^2}}{15}I_3\left(\alpha,\beta\right), \tag{C.15.3}$$

and so on to the desired order. Finally, the external potential can be expressed by the function $I_n\left(\alpha,\beta\right)$ as following

$$\begin{aligned}\varphi_{ex}\left(\alpha,\beta\right)=\varphi_w+\sqrt{\alpha^2+\beta^2}\Bigg[&\left(h_1R_d+\frac{h_2R_d^2}{3\beta}+\frac{h_3R_d^3}{5\beta^2}+\frac{h_4R_d^4}{7\beta^3}\right)I_1\left(\alpha,\beta\right)\\&+\left(\frac{h_2R_d^2}{3}+\frac{h_3R_d^3}{5\beta}+\frac{h_4R_d^4}{7\beta^2}\right)I_2\left(\alpha,\beta\right)+\left(\frac{h_3R_d^3}{15}+\frac{2h_4R_d^4}{35\beta}\right)I_3\left(\alpha,\beta\right)\\&+\frac{h_4R_d^4}{105}I_4\left(\alpha,\beta\right)\Bigg].\end{aligned} \tag{C.16}$$

Here, the highest order of expansion $k_{\max}$ in (C.2) is limited by 4. This expression can be combined with that of the induced potential to give the summary local potential

$$\begin{aligned}\varphi\left(\alpha,\beta\right)&=\varphi_{ex}\left(\alpha,\beta\right)+\varphi_{in}\left(\alpha,\beta\right)\\&=\varphi_w+\sqrt{\alpha^2+\beta^2}\Bigg[\left(h_1R_d+\frac{h_2R_d^2}{3\beta}+\frac{h_3R_d^3}{5\beta^2}+\frac{h_4R_d^4}{7\beta^3}\right)I_1\left(\alpha,\beta\right)\\&\quad+\left(\frac{h_2R_d^2}{3}+\frac{h_3R_d^3}{5\beta}+\frac{h_4R_d^4}{7\beta^2}\right)I_2\left(\alpha,\beta\right)+\left(\frac{h_3R_d^3}{15}+\frac{2h_4R_d^4}{35\beta}\right)I_3\left(\alpha,\beta\right)\\&\quad+\frac{h_4R_d^4}{105}I_4\left(\alpha,\beta\right)\Bigg]+\sqrt{\alpha^2+\beta^2}\sum_{k=1}^{\infty}c_kI_{\lambda k}\left(\alpha,\beta\right).\end{aligned} \tag{C.17}$$

The potential on the surface of the dust particle, where $\beta = \beta_0 = 1/2$, is the same as the wall potential φ_w

$$\varphi_{ex}\left(\alpha, \beta_0\right) + \varphi_{in}\left(\alpha, \beta_0\right) = \varphi_w, \tag{C.18}$$

for any value of α. Taking into account the relation

$$I_k\left(\alpha, \beta_0\right) = I_{\lambda k}\left(\alpha, \beta_0\right), \tag{C.19}$$

one can obtain the unknown coefficients c_k in equation (C.10) expressed by the coefficients of the external potential h_k.

$$\begin{cases} c_1 = -\left(h_1 R_d + \dfrac{h_2 R_d^2}{3\beta_0} + \dfrac{h_3 R_d^3}{5\beta_0^2} + \dfrac{h_4 R_d^4}{7\beta_0^3}\right) \\ c_2 = -\left(\dfrac{h_2 R_d^2}{3} + \dfrac{h_3 R_d^3}{5\beta_0} + \dfrac{h_4 R_d^4}{7\beta_0^2}\right) \\ c_3 = -\left(\dfrac{h_3 R^3}{15} + \dfrac{2h_4 R_d^4}{35\beta_0}\right) \\ c_4 = -\dfrac{h_4 R_d^4}{105} \\ c_k = 0 \quad ; \quad k > 4 \end{cases} \tag{C.20}$$

The surface charge density of the spherical dust particle can be obtained from the normal component of the electric field on the dust surface

$$\begin{aligned} \sigma_s\left(\alpha\right) &= \varepsilon_0 \frac{\alpha^2 + \beta_0^2}{R_d} \frac{\partial \varphi}{\partial \beta}\bigg|_{\beta=\beta_0} \\ &= -\varepsilon_0 \frac{\left(\alpha^2 + \beta_0^2\right)^{3/2}}{R_d} \Bigg\{ h_1 R_d I_{c20}\left(\alpha\right) + \frac{h_2 R_d^2}{3}\left[\frac{I_{10}\left(\alpha\right)}{\beta_0^2} + \frac{I_{c20}\left(\alpha\right)}{\beta_0}\right] \\ &\quad + \frac{h_3 R_d^3}{5}\left[\frac{2I_{10}\left(\alpha\right)}{\beta_0^3} + \frac{I_{c20}\left(\alpha\right)}{\beta_0^2}\right] + \frac{h_4 R_d^4}{7}\left[\frac{3I_{10}\left(\alpha\right)}{\beta_0^4} + \frac{I_{c20}\left(\alpha\right)}{\beta_0^3}\right] \\ &\quad + \frac{h_2 R_d^2}{3} I_{c30}\left(\alpha\right) + \frac{h_3 R_d^3}{5}\left[\frac{I_{20}\left(\alpha\right)}{\beta_0^2} + \frac{I_{c30}\left(\alpha\right)}{\beta_0}\right] \\ &\quad + \frac{h_4 R_d^4}{7}\left[\frac{2I_{20}\left(\alpha\right)}{\beta_0^3} + \frac{I_{c30}\left(\alpha\right)}{\beta_0^2}\right] + \frac{h_3 R_d^3}{15} I_{c40}\left(\alpha\right) \\ &\quad + \frac{2h_4 R_d^4}{35}\left[\frac{I_{30}\left(\alpha\right)}{\beta_0^2} + \frac{I_{c40}\left(\alpha\right)}{\beta_0}\right] + \frac{h_4 R_d^4}{105} I_{c50}\left(\alpha\right) \Bigg\}, \end{aligned} \tag{C.21}$$

where the functions $I_{n0}(\alpha)$ and $I_{cn0}(\alpha)$ are defined as

$$I_{n0}(\alpha) \equiv \int_0^\infty d\lambda\, \lambda^n e^{-\beta_0 \lambda} J_0(\alpha\lambda) \quad \text{and} \tag{C.22}$$

$$I_{cn0}(\alpha) \equiv \int_0^\infty d\lambda\, \lambda^n \frac{J_0(\alpha\lambda)}{\sinh(\beta_0 \lambda)}. \tag{C.23}$$

Finally, the induced charge of the spherical dust particle is

$$\begin{aligned} Q_d &= \int_{\beta=\beta_0} \sigma_s\, dS = 2\pi R_d^2 \int_0^\infty d\alpha \frac{\alpha}{\left(\alpha^2+\beta_0^2\right)^2} \sigma_s(\alpha) \\ &= -2\pi R_d^2 \varepsilon_0 \left\{ h_1 I_{qc2} + \frac{h_2}{3}\left[\frac{I_{q1}}{\beta_0^2} + \frac{I_{qc2}}{\beta_0} + I_{qc3}\right] R_d \right. \\ &\quad + \frac{h_3}{15}\left[\frac{6I_{q1}}{\beta_0^3} + \frac{6\left(I_{q2}+I_{qc2}\right)}{\beta_0^2} + \frac{3I_{qc3}}{\beta_0} + I_{qc4}\right] R_d^2 \\ &\quad \left. + \frac{h_4}{105}\left[\frac{45I_{q1}}{\beta_0^4} + \frac{15\left(I_{qc2}+2I_{q2}\right)}{\beta_0^3} + \frac{3\left(5I_{qc3}+2I_{q3}\right)}{\beta_0^2} + \frac{6I_{qc4}}{\beta_0} + I_{qc5}\right] R_d^3 \right\}. \end{aligned} \tag{C.24}$$

Here, the coefficients I_{qn} and I_{qcn} are defined as

$$\begin{aligned} I_{qn} &\equiv \int_0^\infty d\alpha \frac{\alpha I_{n0}(\alpha)}{\sqrt{\alpha^2+\beta_0^2}} = \int_0^\infty d\alpha \frac{\alpha}{\sqrt{\alpha^2+\beta_0^2}} \int_0^\infty d\lambda\, \lambda^n e^{-\beta_0\lambda} J_0(\alpha\lambda) \\ &= \int_0^\infty d\lambda\, \lambda^n e^{-\beta_0\lambda} \int_0^\infty d\alpha \frac{\alpha}{\sqrt{\alpha^2+\beta_0^2}} J_0(\alpha\lambda) = \int_0^\infty d\lambda\, \lambda^{n-1} e^{-2\beta_0\lambda} = \frac{\Gamma(n)}{(2\beta_0)^n} \end{aligned} \tag{C.25}$$

and

$$\begin{aligned} I_{qcn} &\equiv \int_0^\infty d\alpha \frac{\alpha I_{cn0}(\alpha)}{\sqrt{\alpha^2+\beta_0^2}} = \int_0^\infty d\alpha \frac{\alpha}{\sqrt{\alpha^2+\beta_0^2}} \int_0^\infty d\lambda\, \lambda^n \frac{J_0(\alpha\lambda)}{\sinh(\beta_0\lambda)} \\ &= \int_0^\infty d\lambda \frac{\lambda^n}{\sinh(\beta_0\lambda)} \int_0^\infty d\alpha \frac{\alpha}{\sqrt{\alpha^2+\beta_0^2}} J_0(\alpha\lambda) \\ &= \int_0^\infty d\lambda \frac{\lambda^{n-1} e^{-\beta_0\lambda}}{\sinh(\beta_0\lambda)} = \frac{2}{(2\beta_0)^n} \Gamma(n) \varsigma(n), \end{aligned} \tag{C.26}$$

where $\Gamma(n)$ and $\varsigma(n)$ are the Gamma and the Riemann's Zeta functions, respectively.

In the case of the uniform external electric field,

$$E_{0z} = -\frac{d\varphi}{dz} = -h_1, \tag{C.27}$$

the averaged surface charge density is obtained as

$$Q_d / 4\pi R_d^2 = \varepsilon_0 E_{0z} I_{qc2} / 2 = \varepsilon_0 E_{0z} \Gamma(2)\, \varsigma(2) = \frac{\pi^2}{3} \varepsilon_0 E_{0z}. \tag{C.28}$$

Bibliography

[1] L. Boufendi and A. Bouchoule, Plasma Sources Sci. Technol. **11**, A211 (2002).

[2] L. Boufendi and A. Bouchoule, Plasma Sources Sci. Technol. **3**, 262 (1994).

[3] A. Garscadden, Pure & Appl. Chem. **66** (6), 1319 (1994).

[4] V.N. Tsytovich and J. Winter, Physics-Uspekhi **41**, 815 (1998).

[5] J.P. Sharpe, V. Rohde, The ASDEX-Upgrade Experimental Team, A. Sagara, H. Suzuki, A. Komori, O. Motojima, and The LHD Experimental Group, J. Nucl. Materials **313-316**, 455 (2003).

[6] J. Winter, Plasma Phys. Control. Fusion **40**, 1201 (1998).

[7] K. Narihara, K. Toi, Y. Hamada, K. Yamauchi, K. Adachi, I. Yamada, K.N. Sato, K. Kawahata, A. Nishizawa, S. Ohdachi, K. Sato, T. Seki, T. Watari, J. Xu, A. Ejiri, S. Hirokura, K. Ida, Y. Kawasumi, M. Kojima, H. Sakakita, T. Ido, K. Kitachi, J. Koog, and H. Kuramoto, Nucl. Fusion **37** (8), 1177 (1997).

[8] A. Bouchoule, in *Dusty Plasmas: Physics, Chemistry and Technical Impact in Plasma Processing*, edited by A. Bouchoule (Wiley, New York, 1999).

[9] M. Rubel, M. Cecconello, J.A. Malmberg, G. Sergienco, W. Biel, J.R. Drake, A. Hedqvist, A. Huber, and V. Philipps, Nuclear Fusion **41** (8), 1087 (2001).

[10] T. Ohkawa, Kaku Yugo Kenkyu **37**, 117 (1977).

[11] S.I. Krasheninnikov, Y. Tomita, R.D. Smirnov, and R.K. Janev, Phys. Plasmas **11** (6), 3141 (2004).

[12] G. Federici, C.H. Skinner, J.N. Brooks, J.P. Coad, C. Grisolia, A.A. Haasz, A. Hassanein, V. Philipps, C.S. Pitcher, J. Roth, W.R. Wampler, and D.G. Whyte, Nucl. Fusion **41** (12R), 1967 (2001).

[13] P.K. Shukla and A.A. Mamun, *Introduction to Dusty Plasma Physics* (IoPP, Bristol and Philadelphia, 2002).

[14] P.K. Shukla, Phys. Plasmas **8** (5), 1791 (2001).

[15] U. de Angelis, Physica Scripta **45**, 465 (1992).

[16] V.N. Tsytovich, Physics-Uspekhi **40** (1), 53 (1997).

[17] G.E. Morfill, H.M. Thomas, and M. Zuzic, in *Advances in Dusty Plasmas*, edited by P.K. Shukla, D.A. Mendis, and T. Desai (World Sci., Singapore, 1997).

[18] Y. Tomita, R. Smirnov, and S. Zhu, Plasma Sci. Technol. **7** (1), 2657 (2005).

[19] Y. Tomita, R. Smirnov, Yu. Chutov, A. Takayama, and T. Takizuka, Contrib. Plasma Phys. **44** (1-3), 162 (2004).

[20] L. Tonks and I. Langmuir, Phys. Rev. **34**, 876 (1929).

[21] K.-U. Riemann, J. Phys. D: Appl. Phys. **24**, 493 (1991).

[22] K.-U. Riemann, Phys. Plasmas **4** (11), 4158 (1997).

[23] P.C. Stangeby and J.E. Allen, J. Phys. A: Math. Gen. **3**, 304 (1970).

[24] D. Bohm, in *The Characteristics of Electrical Discharges in Magnetic Fields*, edited by A. Guthrie and R.K. Wakerling (McGrawHill, New York, 1949), Ch. 3.

[25] R.N. Franklin, J. Phys. D: Appl. Phys. **36**, 2821 (2003).

[26] R. Chodura, Phys. Fluids **25** (9), 1628 (1982).

[27] K. Sato, H. Katayama, and F. Miyawaki, Contrib. Plasma Phys. **34** (2-3), 133 (1994).

[28] K.-U. Riemann, J. Phys. D: Appl. Phys. **36**, 2811 (2003).

[29] E.R. Harrison and W.B. Thompson, Proc. Phys. Soc. **74**, 145 (1959).

[30] R.N. Franklin, J. Phys. D: Appl. Phys. **36**, R309 (2003).

[31] V. Godyak and N. Sternberg, Phys. Plasmas **9** (11), 4427 (2002).

[32] M.S. Benilov, Phys. Plasmas **10** (11), 4584 (2003).

[33] V. Godyak and N. Sternberg, Phys. Plasmas **10** (11), 4587 (2003).

[34] R.N. Franklin, Phys. Plasmas **10** (11), 4589 (2003).

[35] V. Godyak and N. Sternberg, Phys. Plasmas **10** (11), 4590 (2003).

[36] V.N. Tsytovich, S.V. Vladimirov, and S. Benkadda, Phys. Plasmas **6** (8), 2972 (1999).

[37] Y.N. Nejoh, Phys. Plasmas **8** (8), 3545 (2001).

[38] J.-X. Ma and M.Y. Yu, Phys. Plasmas **2** (4), 1343 (1995).

[39] E.C. Whipple, Rep. Prog. Phys. **44**, 1197 (1981).

[40] J. Goree, Plasma Sources and Technology **3**, 400 (1994).

[41] H. Mott-Smith and I. Langmuir, Phys. Rev. **28**, 727 (1926).

[42] J.E. Allen, Physica Scripta **45**, 497 (1992).

[43] J.E. Allen, B.M. Annaratone, and U. de Angelis, J. Plasma Physics **63** (4), 299 (2000).

[44] J.E. Allen, J. Tech. Phys. **43** (2), 95 (2002).

[45] M. Lampe, J. Plasma Physics **65** (3), 171 (2001).

[46] D. Bohm, E.H.S. Burhop, and H.S.W. Massey, in *The Characteristics of Electrical Discharges in Magnetic Fields*, edited by A. Guthrie and R.K. Wakerling (McGrawHill, New York, 1949), Ch. 2.

[47] J.E. Allen, R.L. Boyd, and P. Reynolds, Proc. Phys. Soc. **B70**, 297 (1957).

[48] R.V. Kennedy and J.E. Allen, J. Plasma Physics **67** (4), 243 (2002).

[49] J.E. Daugherty, R.K. Porteous, M.D. Kilgore, and D.B. Graves, J. Appl. Phys. **72** (9), 3934 (1992).

[50] S.V. Vladimirov and M. Nambu, Phys. Rev. E **52**, 2172 (1995).

[51] G. Lapenta, Phys. Plasmas **6** (5), 1442 (1999).

[52] S.A. Maiorov, S.V. Vladimirov, and N.F. Cramer, Phys. Rev. E **63**, 017401 (2000).

[53] M.D. Kilgore, J.E. Daugherty, R.K. Porteous, and D.B. Graves, J. Appl. Phys. **73** (11), 7195 (1993).

[54] S.A. Khrapak, A.V. Ivlev, G.E. Morfill, and H.M. Thomas, Phys. Rev. E **66**, 046414 (2002).

[55] S.A. Khrapak and G.E. Morfill, Phys. Rev. E **69**, 066411 (2004).

[56] I.H. Hutchinson, Plasma Phys. Control. Fusion **44**, 1953 (2002).

[57] I.H. Hutchinson, Plasma Phys. Control. Fusion **45**, 1477 (2003).

[58] I.H. Hutchinson, Plasma Phys. Control. Fusion **47**, 71 (2005).

[59] S. Robertson, A.A.S. Gulbis, J. Colwell, and M. Horánui, Phys. Plasmas **10** (10), 3874 (2003).

[60] S.V. Vladimirov and N.F. Cramer, Phys. Rev. E **62** (2), 2754 (2000).

[61] S. Takamura, T. Misawa, N. Ohno, S. Nunomura, M. Sawai, K. Asano, and P.K. Kaw, Phys. Plasmas **8** (5), 1886 (2001).

[62] E.B. Tomme, B.M. Annaratone, and J.E. Allen, Plasma Sources Sci. Technol. **9**, 87 (2000).

[63] S. Nunomura, T. Misawa, N. Ohno, and S. Takamura, Phys. Rev. Lett. **83** (10), 1970 (1999).

[64] N. Ohno, M. Sawai, T. Misawa, K. Asano, and S. Takamura, Physica Scripta **T98**, 81 (2002).

[65] T. Nitter, Plasma Sourc. Sci. Technol. **5**, 93 (1996).

[66] Z. Sternovsky, M. Horányi, and S. Robertson, J. Vac. Sci. Technol. A **19** (5), 2533 (2001).

[67] R. Smirnov, Y. Tomita, T. Takizuka, A. Takayama, and Yu. Chutov, Contrib. Plasma Phys. **44** (1-3), 150 (2004).

[68] R. Smirnov, Y. Tomita, T. Takizuka, A. Takayama, and Yu. Chutov, JPFR SERIES **6**, 752 (2003).

[69] C.K. Birdsall and A.B. Langdon, *Plasma Physics via Computer Simulation* (IoPP, Bristol and Philadelphia, 1991).

[70] R.W. Hockney and J.W. Eastwood, *Computer Simulation Using Particles* (McGraw-Hill, New York, 1981).

[71] C.K. Birdsall, IEEE Trans. Plasma Sci. **19** (2), 65 (1991).

[72] W. Lotz, IPP 1/62 Institute für Plasmaphysik Garching bei München (1967).

[73] *Atomic and Plasma-Material Interaction Data for Fusion Vol.7A*, edited by R.K. Janev, (IAEA, Vienna, 1998).

[74] *Atomic and Plasma-Material Interaction Data for Fusion Vol.7B*, edited by R.K. Janev, (IAEA, Vienna, 1998).

[75] W.H. Cramer, J. Chem. Phys. **30** (3), 641 (1959).

[76] M.A. Lieberman, A.J. Lichtenberg, *Principles of Plasma Discharges and Materials Processing* (Wiley, New York, 1994).

[77] N.N. Lebedev and I.P. Skalskaya, Z. Tech. Phys. **32**, 375 (1962). (in russian)

[78] *American Institute of Physics Handbook*, edited by D.E. Gray et al., (McGraw-Hill, New York, 1972), pp. 4-108, 4-315, 4-225.

[79] C.A.P. Zevenhoven, J. Electrostatics **46**, 1 (1999).